Summer 2010

Spectroscopic Study of Ultracold Rubidium Atoms in an Optical Dipole Force Trap

Eman Mohammed Ahmed
Old Dominion University

SPECTROSCOPIC STUDY OF ULTRACOLD RUBIDIUM ATOMS IN AN OPTICAL DIPOLE FORCE TRAP

by

Eman Mohammed Ahmed
B.S. 2000, Cairo University
M.S. 2005, Old Dominion University

A Dissertation Submitted to the Faculty of
Old Dominion University in Partial Fulfillment of the
Requirement for the Degree of

DOCTOR OF PHILOSOPHY

PHYSICS

OLD DOMINION UNIVERSITY
August 2010

Approved by:

Charles I. Sukenik (Director)

Mark D. Havey (Member)

J. Wallace Van Orden (Member)

Stephen Bueltmann (Member)

John A. Adam (Member)

ABSTRACT

SPECTROSCOPIC STUDY OF ULTRACOLD RUBIDIUM ATOMS IN AN OPTICAL DIPOLE FORCE TRAP

Eman Mohammed Ahmed
Old Dominion University, 2010
Director: Dr. Charles I. Sukenik

The interaction of light with atoms and molecules is of fundamental interest in many branches of science. In atomic physics, this interaction can be used to cool and spatially confine (trap) atoms. These traps can be used as the starting point for other experiments, but the dynamics of the cooling and trapping processes is itself of interest. In order to better understand the physics of trapping atoms in an optical dipole force trap, we have conducted a series of spectroscopic measurements of ultracold rubidium atoms in such a trap. The trap was created at the focus of a Nd:YAG laser beam with wavelength 1064nm and nearly Gaussian spatial mode. For rubidium, the trap light is red-detuned and the atoms are confined to the highest intensity in the beam. In order to probe the atoms confined in the trap, we have performed spectroscopy on the $5S_{1/2} \rightarrow 5P_{3/2}$ transition. Because the polarizability of the ground and excited states is not the same at the trap wavelength, the spectra exhibit both a shift and inhomogeneous broadening. We have investigated the spectra for both linear and circular polarized traps. We also studied the application of a second laser to couple the excited state ($5P_{3/2}$) to another higher excited state ($5D_{5/2}$) to reduce the inhomogeneous broadening of the $5S_{1/2} \rightarrow 5P_{3/2}$ transition. Finally, two-photon spectroscopy was performed on atoms in the dipole force trap and compared to spectra taken in a magneto optical trap (MOT). Autler-Townes splitting was clearly observed in the MOT and appears to have been observed in the dipole force trap also.

To my family...

ACKNOWLEDGMENTS

I would like to thank my adviser, Dr. Charles Sukenik for giving me the opportunity to join his research group. I really learned so much and I gained a lot of experience working in his lab. I thank him deeply for his patience, understanding, and support. His continuous guidance and help made it possible to be where I am now. I would also like to thank Dr. Mark Havey, Dr. J. Wallace Van Orden, Dr. Stephen Bueltmann, and Dr. John Adam for agreeing to be part of my dissertation committee. Many additional thanks to Dr. Havey for his assistance in the experiment.

I would like to express my gratitude to the former graduate student who worked on the same experiment setup, Dr. Minarni Shiddiq, for explaining all the aspects of the experiment and for all the helpful discussions even after she left Old Dominion University. My appreciation goes to Dr. Michael Shaffer for letting me work on his experimental setup and for answering my questions during the first summer of my graduate studies. My thanks to Gambhir Ranjit for being a great lab partner and for sharing equipment and ideas. My appreciation goes to him and his wife for their help and support and for being really good friends. I also thank Maha Omar for her help during the finishing of my data taking and for her kind support.

A special thanks to our department chair Dr. Gail Dodge who is always ready to help everyone professionally and personally. I would also like to thank Dr. Lepsha Vuskovic for her understanding and support. I thank the operational manager of the physics department, Mr. Walt Hooks, and the wonderful department staff, Annette Vialet and Delicia Malin for their help and support over the years.

My heartfelt appreciation to my dear friends Saori Pastore and Jan Drake for their generosity, kindness, and joyful friendship.

I would like to thank Dr. Geoff Krafft for his sincere assistance during the Free-Electron Laser (FEL) run-time at Jefferson Lab. I also thank the professional FEL staff for helping us in the FEL experimental setup.

Finally, I cannot forget to thank all my previous teachers in Egypt and the United States who have shaped my mind and my heart, and made me the person I am today.

TABLE OF CONTENTS

LIST OF TABLES

LIST OF FIGURES

CHAPTER I

INTRODUCTION

The development of laser cooling and trapping techniques for ions and neutral atoms in the last few decades has greatly enhanced the ability to control and manipulate atoms, impacting a range of fields from precision atomic measurements and atomic clocks to quantum degenerate gases and quantum information processing. Laser cooling generally refers to a number of techniques in which atomic and molecular samples are cooled through the interaction with one or more laser light fields.

Over the decades since it was first proposed, trapping and cooling of ions and neutral atoms has become routine for more than 150 research labs around the world [1, 2]. Early laser cooling and trapping experiments used exclusively alkali metal atoms due to their simple atomic structure and convenient laser wavelength, but later alkaline-earth metals, noble gases and even radioactive isotopes were also used as samples. The simplest laser cooling mechanism is called Doppler cooling. Other cooling mechanisms are the sub-Doppler (Sisyphus) cooling, subrecoil cooling such as velocity selective coherent population trapping and Raman cooling, and most notably evaporative cooling.

The most widely used atom trap is the Magneto-Optical Trap (MOT) which uses radiation pressure to cool and trap atoms. Besides the MOT, there are a number of other trapping techniques that have been used to confine ions or neutral atoms. These traps use different types of forces. For example, magnetic traps confine atoms by exerting a force on the atomic magnetic dipole moments while ion traps use a static homogeneous magnetic field and static inhomogeneous electric field (Penning Trap) or an oscillating electric field (Paul Trap) to trap ions. There is also the gravitational trap which uses the force of gravity in combination with other forces to confine atoms. The optical dipole force trap uses the optical dipole force to trap neutral atoms. The dipole force arises from the interaction of a spatially inhomogeneous laser field with the induced atomic electric dipole moment.

Recently, a growing number of experiments in laser cooling and trapping have used an optical dipole force trap rather than a MOT or a magnetic trap because it provides a high density sample of atoms, low scattering rate, and does not require a

This dissertation follows the style of the Physical Review A.

complicated magnetic system. The first optical dipole force traps used a trap laser with frequency detuned slightly below atomic resonance (red detuning) and a power on the order of a few mW. Now, because of the advances in laser production such as the high power CO_2 lasers and the family of Nd:YAG lasers, one can build an optical dipole force trap detuned far from resonance (far off resonance trap–FORT) and much further from resonance (quasi electrostatic trap–QUEST) as well as detuned above atomic resonance (blue detuning) with laser power on the order of many tens of Watts. Optical dipole force traps also have been used to create Bose-Einstein condensates and quantum degenerate Fermi gases.

Applications of trapped and cooled atoms include potential areas such as precision spectroscopy and gravitational measurements, atomic optics, atomic interferometers, atomic clocks, atomic lasers, atomic lithography, and quantum computing. Currently the NIST-F1 clock, which is a laser cooled cesium fountain atomic clock, located at the National Institute of Standards and Technology (NIST) in Boulder, Colorado, serves as the United States' primary time and frequency standard [3]. The uncertainty of NIST-F1 is about 5×10^{-16}, which means it would neither gain nor lose a second in more than 60 million years! This level of time accuracy will greatly improve the performance of the US Global Positioning System (GPS) and the synchronization of the modern telecommunication networks.

Historical Milestones for the Cooling and Trapping of Atoms

The history of laser cooling and trapping is very rich with excitement, scientific cooperation and also Nobel prizes. All this started about half a century ago when the first idea of using radiation to control atoms was introduced as listed below:

- 1962: Askar'yan considered the dipole force confinement of plasmas and neutral atoms [4].
- 1968: Letokhov suggested that atoms might be one-dimensionally confined at the nodes or anti-nodes of a standing wave tuned far below or above the atomic transition frequency [5].
- 1970: Ashkin (1970) demonstrated the trapping of micron-sized particles in laser light based on the combined action of radiation pressure and the dipole force [6]. Later he suggested three-dimensional traps for neutral atoms [7].

- 1975: Hänsch and Schawlow and simultaneously Wineland and Dehmelt proposed laser Doppler cooling using a pair of counter propagating laser beams with frequency tuned slightly below the atomic frequency resonance (optical molasses) [8, 9].

- 1978: Bjorkholm *et al.* demonstrated the focusing, defocusing and steering of a beam of neutral atoms by the dipole forces [10]. In the same year Neuhauser *et al.* and Wineland *et al.* demonstrated the laser cooling of trapped ions [11, 12].

- 1982: Philips and Metcalf were able to stop a thermal beam of sodium atoms using a laser beam and a varying magnetic field to provide a changing Zeeman shift in order to cancel the Doppler shift as the atoms decelerated [13].

- 1985: Chu *et al.* realized the first three-dimensional optical molasses by trapping and cooling neutral atoms to 240 μK [14].

- 1987: Dalibard suggested the Magneto-Optical Trap (MOT) which was soon realized experimentally by Raab *et al.* [15]. Thorsheim *et al.* proposed the laser-induced photoassociation (PA) of ultracold atoms to create translationally cold molecules [16].

- 1988: Lett *et al.* observed the first laser cooling of sodium atoms below the Doppler Limit (Sub-Doppler cooling) at 40 μK [17]. The theoretical explanation of this contradiction was soon presented by Dalibard and Cohen-Tannoudji [18] and Ungar *et al.* [19].

- 1989: Dehmelt and Paul were awarded the Nobel prize for the development of the ion trap technique [20, 21].

- 1993: Lett *et al.* and Miller *et al.* observed for the first time cold sodium molecules (Na_2) and cold rubidium molecules (Rb_2), respectively, by the photoassociation of laser-cooled atoms [22, 23]. Davidson *et al.* cooled Sodium atoms to a subrecoil temperature with stimulated Raman transitions (Raman cooling) in two and three dimensions [24].

- 1994: J. Lawall *et al.* observed the first subrecoil laser cooling in two dimensions by velocity selective coherent population trapping [25]. Davis *et al.* achieved a subrecoil forced evaporative cooling of magnetically trapped sodium atoms [26].

- 1995: Anderson *et al.* produced the first Bose-Einstein condensate (BEC) in a vapor of ^{87}Rb atoms that was confined by magnetic fields and evaporatively cooled to 20 nK [27].

- 1997: Chu, Cohen-Tannoudji and Philips were awarded the Nobel prize for development of methods to cool and trap atoms with laser light [28, 29, 30].

- 1998: Bloch *et al.* demonstrated the first continuous-wave coherent beam of cold atoms from a BEC (atom laser) [31].

- 2001: Cornell, Ketterle and Wieman were awarded the Nobel prize for the achievement of Bose-Einstein condensation in dilute gases of alkali atoms [32, 33].

- 2003: Jochim *et al.* and Greiner *et al.* made the first independent observations of BEC of molecules [34, 35].

- 2005: Hall and Hänsch were awarded the Nobel prize for their contributions to the development of laser-based precision spectroscopy, including the optical frequency comb technique facilitated by laser cooling and trapping of atoms [36, 37].

To better understand the physics of trapping atoms in an optical dipole force trap, we have conducted a series of spectroscopic measurements of ultracold rubidium atoms in such a trap. The trap was created at the focus of a Nd:YAG laser beam with wavelength 1064 nm and nearly Gaussian spatial mode. The trap laser beam can be either continuous-wave (used to form the cw FORT) or mode-locked (used to form the pulsed FORT). There is no cooling in a FORT since it uses a conservative force, so first we cool and confine the atoms using a magneto-optical trap and then we load them into the FORT. The dynamics of the loading process from a MOT to a cw FORT was fully investigated by Kuppen et al. and Corwin [38, 39]. A comparison between the performance of the pulsed FORT and that of the cw FORT was performed on our experiment by the former graduate student Dr. Minarni Shiddiq [40, 41]. In most respects both the cw and pulsed FORTs show comparable behavior. There was a notable difference in the FORT loading efficiency dependence on the detuning of the MOT trap laser frequency during the loading phase. That was a motivation for a further investigation of both traps.

To study the shift the atoms experience in the optical dipole trap, we used a laser beam that is scanned across the possible transitions between the ground and excited states to kick the atoms from the trap. By detecting the number of atoms remaining we can obtain the perturbed spectra and hence measure the shift. Due to the opposite and spatially dependent shift of the ground and excited states, the transition obtained is inhomogeneously broadened. We studied the application of a second laser to couple the first excited state to another higher excited state to reduce the inhomogeneous broadening. We also explored the use of Autler-Townes spectroscopy as a probe of the atoms in the trap.

Specific interest here in optical dipole force traps results from our desire to use the free electron laser at nearby Jefferson Laboratory (in Newport News, Virginia) to construct an optical dipole force trap. Because of the laser's ability to produce infrared light with kiloWatts of average power, it is an excellent candidate for realizing both spatially large and energetically deep traps that would otherwise be difficult to produce using table top lasers. The line of research presented in this dissertation is part of a program to better understand dipole force traps in both the continuous-wave and pulsed regimes. The free electron laser at Jefferson Lab is, in fact, a pulsed laser with sub ps pulse width. As a result, understanding the different dynamics of pulsed vs. cw optical dipole force traps is important. Spectroscopy of atoms in the trap is a powerful tool to gain a better understanding of trapping dynamics.

This dissertation is divided into 5 chapters. In Chapter II, the theoretical background of the experimental aspects such as the principles of atom cooling using laser light, and trapping using dipole forces will be derived. The experimental apparatus, laser setup, electronics used and controlling of the experiment using the computer system will be presented in Chapter III. The results and discussion of the spectroscopic experiments performed on both ^{85}Rb and ^{87}Rb atoms in the MOT and in the FORT will be presented in Chapter IV. Finally, in Chapter V, the conclusions and the outlook will be presented.

CHAPTER II

THEORETICAL BACKGROUND

In this chapter, the basic theory and techniques of laser cooling and trapping of neutral atoms will be presented. The physical and spectral properties of the used rubidium atoms will be briefly given in Sec. II.2. The theories of Doppler cooling and Sub-Doppler cooling are derived in Sec. II.3. The basic principles of the Magneto-Optical Trap (MOT) and Optical Dipole Force Trap are explained in Sec. II.4 and Sec. II.5, respectively. Finally, the inhomogeneous broadening and Autler-Townes spectral line effects are discussed in Sec. II.7 and Sec. II.8, respectively.

II.1 OVERVIEW

The interaction between light and atoms is one of the most important subjects in quantum optics and the building block of laser spectroscopy. Theoretically speaking, any neutral atom can be cooled and trapped through the interaction between a laser light field and the atom. In practice, there are many criteria that have to be fulfilled to make a laser cooling and trapping experiment successful [42]. First, the atom needs to have a cooling transition which is accessible by an available laser beam with enough power and suitable frequency. Second, one needs to be able to scatter photons on the chosen transition so that the spontaneous emission out of the excited state should go entirely to the ground state or metastable state from which it was excited (cycling transition). The feasibility of producing an atomic beam or vapor which can be sent to the observation chamber and cooled by a laser beam is also one of the requirements for a successful laser cooling experiment.

So far, there are mainly three types of atoms that have been successfully cooled and trapped; alkali metal atoms, metastable noble gas atoms, and alkaline earth atoms. However, some other elements in the periodic table have also been used in laser cooling and trapping experiments such as silver, erbium, and ytterbium. Alkali metals were the first elements used in laser cooling and trapping experiments for several reasons. The first reason is because most of their cooling transition frequencies are in the visible region or near-IR and easily accessible by commercial lasers such as diode lasers, dye lasers, and Ti:Sapphire lasers. Second, they can be vaporized easily without a complicated oven. Alkali metal atoms also have a single electron outside of

a closed shell, hence, they have a relatively simple hydrogen-like structure of energy levels and only the valence electron contributes to the orbital angular momentum of the atom. This is very important for having a cycling transition and also can simplify theoretical calculations required for comparison with experimental results.

The most common neutral alkali metal atoms used in laser cooling and trapping experiments are rubidium and cesium since the cooling transitions are accessible by commercial diode lasers, followed by sodium whose cooling transition is accessible by a dye laser. Lithium is of interest in quantum degeneracy experiments since it can provide a bosonic as well as fermionic stable isotope [43], while potassium is harder to cool since it has an unusual hyperfine structure. Hydrogen atoms are very difficult to cool because their transition has to be excited by far-ultraviolet frequency light, a laser in this frequency range is not easily available at present, however, Bose-Einstein Condensates have been made using atomic hydrogen [44]. Finally, since francium is a radioactive element, a francium beam is harder to produce, though francium has also been confined in a Magneto-Optical Trap.

II.2 RUBIDIUM

Rubidium (Latin: rubidus, deepest red) was discovered in 1861 by the German chemists Robert Bunsen and Gustav Kirchhoff in the mineral lepidolite through the use of a spectroscope. The sample produced a set of deep red spectral lines they had never seen before. Bunsen was eventually able to isolate samples of rubidium metal [45]. Rubidium is one of the most commonly used atomic species employed for laser cooling and Bose-Einstein condensation because of its convenient spectral absorption range accessible by readily available and inexpensive diode laser light and the moderate temperatures required to obtain substantial vapor pressures. In 1995, rubidium was used to make a Bose-Einstein condensate [27], for which the discoverers won the 2001 Nobel Prize in Physics [32].

II.2.1 Physical Properties

Rubidium (chemical symbol, Rb) is a soft, silvery-white metallic element of the alkali metal group (group 1 in the periodic table of elements). It has atomic number 37, atomic mass 85.4678 g/mol and density 1.53 g/cm^3 at 20°C. Rubidium melts at a temperature of 39.3 °C (102.7 °F) and is easily vaporized at 688 °C (1270 °F). It is

considered to be the 16th most abundant element in the earth's crust. There are 26 isotopes of rubidium known, with naturally occurring rubidium being composed of just two isotopes, the only stable isotope ^{85}Rb (72.2%) and the very weakly radioactive isotope ^{87}Rb (27.8%) with a half-life of 4.88×10^{10} years (more than three times longer than the estimated age of the universe and is thus effectively stable). Rubidium is highly reactive with properties similar to the other alkali metals, such as very rapid oxidation in air and violent reaction with water, vigorous enough to ignite the liberated hydrogen. Rubidium has also been reported to ignite spontaneously in air. In practice, rubidium is usually sealed in glass ampoules in an inert atmosphere to ensure safety and purity.

II.2.2 Spectral Properties

The electron configuration of rubidium in the ground state has the sequence $1s^2$ $2s^2p^6$ $3s^2p^6d^{10}$ $4s^2p^6$ $5s^1$. From this configuration, it is clear that the ground state of the rubidium atom has closed core shells with only one electron in its valence shell. Since the core shells are closed, these electrons do not contribute to the orbital angular momentum, leaving the total orbital momentum to be determined by the state of the valence electron [46, 47]. Using Russell-Saunders notation

$$n^{2S+1}L_J, \tag{1}$$

where n is the principle quantum number of the valence electron, L is the total orbital angular momentum quantum number (S and P refer to L with values 0 and 1, respectively), S is the total electronic spin quantum number ($2S+1$ is the spin multiplicity) and J is the total angular momentum quantum number of the electron, $\vec{J} = \vec{L} + \vec{S}$, which can take the values

$$|L - S| \leq J \leq L + S, \tag{2}$$

the ground state of the atom can be written as $5^2S_{1/2}$ with total orbital angular momentum $L = 0$ and total angular momentum $J = 1/2$. Due to the spin-orbit interaction (LS-Coupling), the excited state 5P is split into two fine-structure components with $J = 1 \pm 1/2$. The 5S – 5P transitions which are known as the D-doublet of alkali metals are very important in laser cooling experiments. The transition $5^2S_{1/2}$ – $5^2P_{1/2}$ is known as the D_1 line with a transition wavelength of 795.0 nm and the transition $5^2S_{1/2}$ – $5^2P_{3/2}$ is known as the D2 line with a wavelength of 780.1 nm.

Besides the spin-orbit interaction, there is also an interaction of the nuclear magnetic moment with the total angular momentum of the electron. This is described in terms of the total angular momentum of the atom $\vec{F} = \vec{J} + \vec{I}$ where $\vec{I}$ is the nuclear spin of the atom which has a magnitude $I = 5/2$ for ^{85}Rb and $I = 3/2$ for ^{87}Rb and $\vec{J}$ is the total angular momentum of the electron. The magnitude of F can take the values

$$|J - I| \leq F \leq J + I. \tag{3}$$

This interaction splits the ground state and the excited states into what is called hyperfine structure. Here, the ground state splits into two $5^2S_{1/2}$ states with quantum number $F = 2$, $F = 3$ for ^{85}Rb, and $F = 1$, $F = 2$ for ^{87}Rb. The excited states split into two and four lines for $5^2P_{1/2}$ and for $5^2P_{3/2}$, respectively. Due to the different nuclear masses of the two isotopes ^{85}Rb and ^{87}Rb, the transition frequencies of ^{87}Rb are shifted slightly up compared to those of ^{85}Rb. The complete fine structure and hyperfine structure of ^{85}Rb and ^{87}Rb atoms can be seen in Fig. 1. For ^{85}Rb, the transition from $F = 3$ to $F' = 4$ is used for the cooling/trapping because it is a closed transition and has the highest transition strength. This transition can be excited by a laser with wavelength 780.1 nm. For ^{85}Rb, the lifetime of the excited states is 26.63 ns and the linewidth is $\sim$ 6 MHz. Some atoms can make an off-resonant transition from $F = 3$ to $F' = 3$ for ^{85}Rb and then decay into $F = 3$ or $F = 2$. If the atoms decay into $F = 2$, they will no longer scatter photons by the the trapping laser light (no more cooling), hence a second laser (repump laser) is needed to pump the atoms back to the excited states (from which they will subsequently decay) to keep the population of atoms in the upper hyperfine level of the ground state.

In a weak magnetic field (Zeeman effect), each hyperfine state F splits into the states $m_F = -F, ..., F$. The energy splitting is $\Delta E_{m_F} = m_F g_F \mu_B \times B$, where μ_B is Bohr's magneton, B is the magnetic field flux density and g_F is the Landé g-factor for each state in F:

$$\begin{aligned} g_F &= g_J \frac{F(F+1) - I(I+1) + J(J+1)}{2F(F+1)} \\ &\quad + g_I \frac{F(F+1) + I(I+1) - J(J+1)}{2F(F+1)} \end{aligned} \tag{4}$$

$$g_F \simeq g_J \frac{F(F+1) - I(I+1) + J(J+1)}{2F(F+1)}, \quad (5)$$

because the Landé g-factor g_I for the nucleus is much smaller than the Landé g-factor g_J for the electrons[1] by the ratio of the electron mass to the proton mass.

II.3 LASER COOLING

Laser cooling and trapping of an atom depends on the interaction between laser light and an atom to exert a controllable force on the atom [42]. This light force is either dissipative (absorptive) or dispersive (reactive). The dissipative forces are velocity dependent and can be used for cooling as radiation pressure or scattering force. On the other hand, purely dispersive forces are conservative and spatially dependent, hence can be used for trapping as the dipole force. Cooling is then associated with the reduction of the atomic velocity spread around a given value and trapping is related to the control of the position of the atoms in space [48]. Cooling has two important milestones: the Doppler limit and the recoil limit. At each limit, a new approach to cooling must be adopted.

To understand the cooling process, let us consider the process of absorption and emission of photons by an atom. As seen in Fig. 2, when an atom of mass M absorbs a photon from the laser light with wave vector $\vec{k}$, the atom becomes excited. The atom's net momentum decreases by $\hbar\vec{k}$ which is related to a recoil velocity $v_{rec} = \hbar k/M$ and the atom slows down. After a time $\tau = 1/\Gamma$, the excited atom emits a photon spontaneously in a random direction and returns to the ground state. In this emission process, the momentum of the atom changes in the amount of $-\hbar\vec{k}'$. The emission process can be portrayed as a random walk of the atom in momentum space with step size of $\hbar\vec{k}'$. This process is observed as a momentum diffusion or heating of the atom. So, the net change in the momentum of the atom due to a single absorption-emission event is $\Delta\vec{p} = \hbar(\vec{k} - \vec{k}') = \hbar(\Delta\vec{k})$. The mean contribution of $\hbar\vec{k}'$ is zero because spontaneous emission occurs with the same probability in two opposite directions, making $\Delta\vec{p} = \hbar\vec{k}$. The atoms are being slowed down in one direction which is the direction of the laser beam, but at the same time experience a diffusive heating due to the random walk in momentum space.

[1] For the electrons, the Landé g-factor is given by
$g_J = g_L \frac{J(J+1)-S(S+1)+L(L+1)}{2J(J+1)} + g_S \frac{J(J+1)+S(S+1)-L(L+1)}{2J(J+1)} \simeq 1 + \frac{J(J+1)-S(S+1)+L(L+1)}{2J(J+1)}$

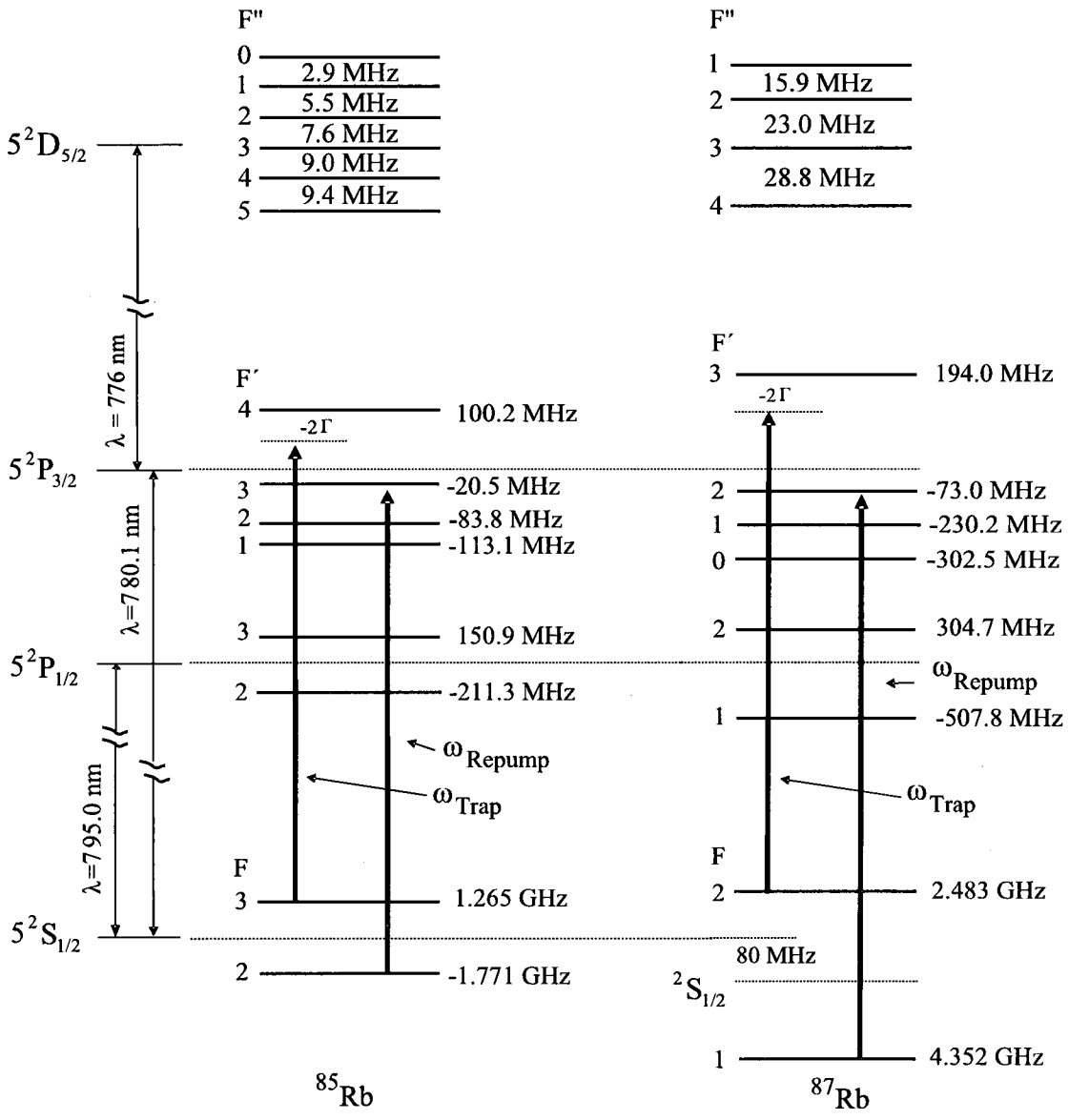

FIG. 1: Energy level diagrams of $5S - 5P - 5D$ transition for ^{85}Rb and ^{87}Rb. Not shown is the $5D_{3/2}$ manifold.

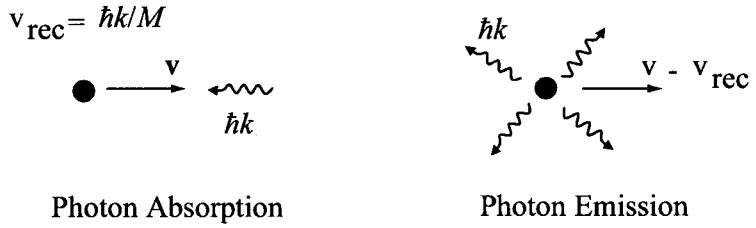

FIG. 2: The photon absorption and photon emission by an atom involves transferring photon momentum $\hbar\vec{k}$ and changing the atom's velocity in the amount of the recoil velocity v_{rec}.

The net force $\vec{F}$ on the atom as a result of its interaction with laser light or the force from absorption followed by spontaneous emission is

$$\vec{F} = \hbar\vec{k}\,\gamma_p, \tag{6}$$

where $\hbar\vec{k}$ is the amount of momentum being transferred for each photon and γ_p is the scattering rate which is given by a Lorentzian-shaped emission line

$$\gamma_p = \frac{\Gamma}{2}\frac{s}{1+s+(\frac{2(\Delta+\omega_D)}{\Gamma})^2}, \tag{7}$$

where:

- $s = I/I_{\text{sat}}$, the normalized intensity,
- $I_{\text{sat}} \equiv \pi hc\Gamma/3\lambda^3$, saturation intensity,
- Δ is the detuning from the atom's resonance frequency,
- $\omega_D = -\vec{k}\cdot\vec{v}$, the Doppler shift.
- Γ is the natural linewidth of the excited state which is equal to the inverse of the natural lifetime of the excited state τ.

For the resonance transition of ^{85}Rb, with $\Gamma/2\pi = 6$ MHz, the maximum acceleration due to the light force is 0.1×10^6 m/s^2 or equals 10^4g for a single photon recoil. By substituting Eq. (7) into Eq. (6), the net scattering force can be rewritten as

$$\vec{F}(\vec{v}) = \hbar\vec{k}\frac{\Gamma}{2}\frac{s}{1+s+(\frac{2(\Delta-\vec{k}\cdot\vec{v})}{\Gamma})^2}. \tag{8}$$

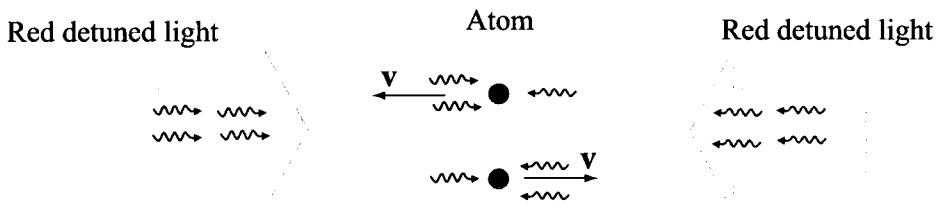

FIG. 3: A one-dimensional optical molasses. An atom moving to the left scatters more light coming from the left, an atom moving to the right scatters more light coming from the right.

II.3.1 Doppler Cooling

The cooling of neutral atoms using a pair of counter propagating laser beams, with frequency tuned slightly below the atomic resonance frequency, was first proposed in 1975 by Hänsch and Schawlow [8]. Since the Doppler effect plays a central role in this method, the cooling process is often called "Doppler cooling".

A schematic Doppler cooling process is shown in Fig. 3. Consider an atom with a cooling transition between a ground state and an excited state. The resonance frequency of the transition is ω_0 and the excited state can emit photons with a decay rate Γ (lifetime τ). The atom which is moving with velocity $\vec{v}$ is illuminated by two counter-propagating laser beams with frequency ω. Because of the Doppler effect, the atom moving toward the incoming laser beam sees the laser frequency shifted higher (blue shifted) by an amount $\omega_{\rm D} = \vec{k} \cdot \vec{v} = \omega_0(v/c)$. So, by detuning the laser frequency lower (red detuned), the atom is more likely to scatter photons from this laser beam. The atom which is moving to the left sees the frequency of the laser beam moving to the right closer to resonance resulting in increased photon scattering, while it sees the frequency of the laser beam moving to the left shifted out of resonance and hence it is less likely to scatter photons from this beam. The opposite happens to an atom moving to the right. This scheme is called "one-dimensional optical molasses."

The average force for the one-dimensional molasses, as shown in Fig. 3, is the sum of the forces due to the two counter-propagating laser beams $\vec{F}_{\rm av} = \vec{F}_+ + \vec{F}_-$ [42],

$$\vec{F}_\pm = \pm \frac{\hbar \vec{k} \Gamma}{2} \frac{s}{1 + s + (\frac{2(\Delta \mp |\vec{k} \cdot \vec{v}|)}{\Gamma})^2}, \tag{9}$$

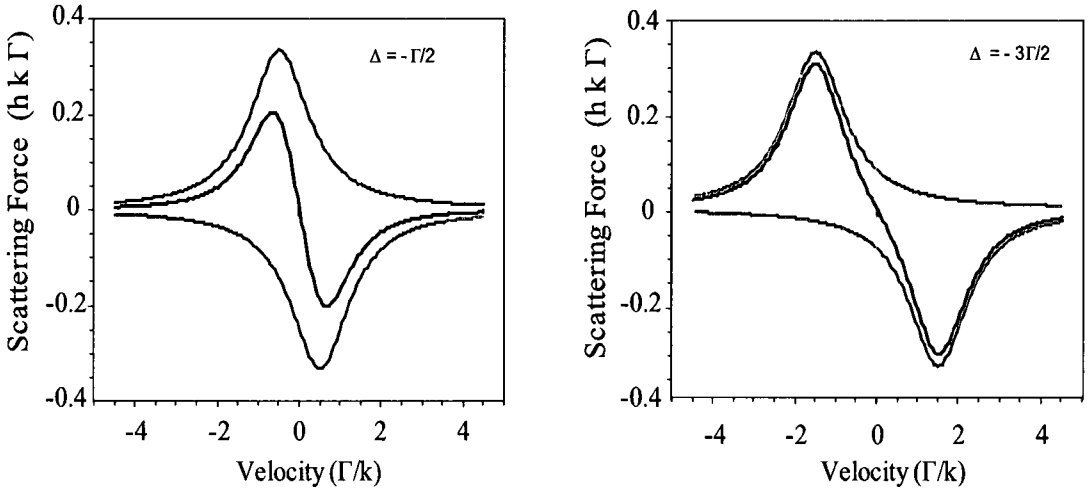

(a) $\Delta = -\Gamma/2$ (b) $\Delta = -3\Gamma/2$

FIG. 4: Each of the counter-propagating beams exerts a scattering force with a Lorentzian velocity dependence (gray line). The average force exerted on the atoms is the sum of these forces (black line). The detunings are (a) $-\Gamma/2$ and (b) $-3\Gamma/2$.

$$\vec{F}_{\rm av} \cong \frac{4\hbar k^2 s}{[1+s+(\frac{2\Delta}{\Gamma})^2]^2}\frac{2\Delta}{\Gamma}\vec{v} = -\kappa_1 \vec{v}. \tag{10}$$

For $\Delta < 0$, the one-dimensional molasses with two counter-propagating beams actually reduces the velocity of the atoms with a damping coefficient κ_1. As shown in Figs. 4(a) and 4(b) for detunings $\Delta = -\Gamma/2$ and $\Delta = -3\Gamma/2$, respectively, both at $s = 2$, the net force from the two beams displays the viscous damping around $v = 0$.

For the low intensity approximation ($s \ll 1$) and low velocity ($kv \ll \Gamma$), Eq. (10) becomes

$$\vec{F}_{\rm av} \cong \frac{4\hbar k^2 s}{[1+(\frac{2\Delta}{\Gamma})^2]^2}\frac{2\Delta}{\Gamma}\vec{v} = -\kappa_1 \vec{v}. \tag{11}$$

The nature of the absorption and emission processes sets a limit on the temperature that can be achieved by this cooling process. The fluctuations of the scattering force due to random kicks from spontaneous emission and the random nature of the absorption events results in diffusion in momentum or heating [42, 49, 50]. There are a number of ways to derive the cooling limit given by the Doppler cooling process. One of the ways is by setting the sum of the heating and cooling rates to zero (steady-state condition). As mentioned earlier, in a given absorption/emission cycle

or a scattering process, the atom receives two random kicks of magnitude $\hbar\vec{k}$. The scattering rate at which the atoms get the kicks from both plane waves is derived from Eq. (7) and for $s \ll 1$ (low saturation) and $kv \ll \Gamma$ (small velocity) is given by

$$\gamma_p = \Gamma \frac{s}{1 + (\frac{2\Delta}{\Gamma})^2}. \tag{12}$$

A momentum diffusion coefficient D_p is defined as

$$D_p \equiv \langle \dot{p}^2 \rangle / 2 = \gamma_p \, \hbar^2 \, k^2. \tag{13}$$

such that D_p/M is the heating rate $\dot{E}$ due to the randomness, which can be written as

$$\left.\frac{\partial E}{\partial t}\right|_{heat} = D_p/M = \gamma_p \, (\hbar k)^2/M, \tag{14}$$

where p is the average momentum imparted to the atoms and M is the atomic mass.

The cooling rate due to the cooling force as derived in Eq. (11) is

$$\left.\frac{\partial E}{\partial t}\right|_{cool} = \vec{F} \cdot \vec{v} = -\kappa_1 v^2 \tag{15}$$

where κ_1 equals to

$$\kappa_1 = \frac{4\hbar \, k^2 \, s}{[1 + (2\Delta/\Gamma)^2]^2} \frac{2\Delta}{\Gamma}. \tag{16}$$

In steady state,

$$\left.\frac{\partial E}{\partial t}\right|_{heat} + \left.\frac{\partial E}{\partial t}\right|_{cool} = 0 \tag{17}$$

then using Eq. (14) and Eq. (15),

$$D_p/\kappa_1 = M \, v^2 = M \, \langle v^2 \rangle = k_B T, \tag{18}$$

where k_B is the Boltzmann constant and v^2 becomes $\langle v^2 \rangle$ if $\hbar k^2/M \ll \Gamma$ which is well satisfied for the strong dipole transition of rubidium and most other atoms used in laser cooling [50]. The last term of Eq. (18) comes from the equipartition theorem in one degree of freedom. Using Eq. (13) and Eq. (16),

$$k_B T = \frac{\hbar\Gamma}{4} \frac{1 + (2\Delta/\Gamma)^2}{2\Delta/\Gamma}. \tag{19}$$

The Doppler limit or the minimum temperature is obtained for detuning $\Delta = -\Gamma/2$. From Eq. (19), the Doppler temperature or Doppler limit at low saturation and small velocity is obtained as

$$T_{\mathrm{D}} = \frac{\hbar\Gamma}{2k_B}. \tag{20}$$

II.3.2 Sub-Doppler (Sisyphus) Cooling

We assumed in the theory of Doppler cooling that the atom has a simple two-level state structure, however many real atoms have hyperfine structure and Zeeman sublevels which gives rise to a new cooling mechanism. The new surprising temperature of the optical molasses was actually below the Doppler limit T_{D} and was discovered after an accurate measurement method of the temperature had been developed. The cooling mechanisms rely on multilevel atoms, light shifts, polarization gradients, and optical pumping [17, 30]. For this reason, this cooling mechanism is known as "polarization gradient cooling". It is also called sub-Doppler cooling since lower temperatures than those in the theory of Doppler cooling can be achieved using this mechanism.

The interaction between nearly resonant light and atoms can drive transitions between atomic energy levels due to the scattering process which is a velocity-dependent mechanism. The interaction also can shift the atomic energy levels (Zeeman sublevels) due to the Stark shift, this mechanism depends on the spatial varying light field. The spatial varying light field can be obtained using two counter-propagating light beams with the same intensity and wavelength but orthogonal polarization, the superposition of these beams produces a standing wave whose polarization varies in space. The total electric field of two counter-propagating beams, which propagate in the z-direction with frequency ω can be written as

$$\vec{E}(z,t) = \vec{\mathcal{E}}(z)e^{-i\omega t} + \vec{\mathcal{E}}^{*}(z)e^{+i\omega t}, \tag{21}$$

where the field vector is given by

$$\vec{\mathcal{E}}(z) = \mathcal{E}_0(\hat{e_x}e^{ikz} + \hat{e_y}e^{-ikz}) = \sqrt{2}\mathcal{E}_0 e^{ikz}\hat{\epsilon}(z), \tag{22}$$

where $\hat{\epsilon}(z) = \frac{1}{\sqrt{2}}(\hat{e_x} + \hat{e_y}e^{-2ikz})$. It is clear that the polarization $\hat{\epsilon}(z)$ of the light field varies in space.

In the low intensity limit (the optical coherences and any mechanisms in the excited states can be ignored), the light shifts ΔE_{g} of the ground magnetic sublevels due to the light field are given by [42]

$$\Delta E_{\mathrm{g}} = \frac{\hbar\,\Delta\, s\, C_{\mathrm{ge}}^2}{1 + (2\Delta/\Gamma)^2}, \tag{23}$$

where s is the normalized intensity, Δ is the detuning from the atom's resonance frequency, and C_{ge} is the Clebsch-Gordon coefficient that describes the coupling

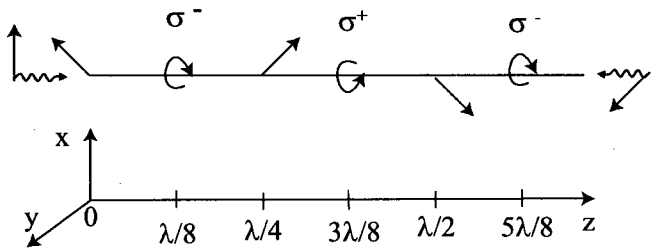

FIG. 5: Superposition of two orthogonal, linearly polarized, counter-propagating laser beams. The polarization of the light field changes four times in a period of $\lambda/2$.

between the atom and the light field. The values of $C_{\rm ge}$ depend on the polarization of the light field and the magnetic quantum number which are different for each transition and can be found in [42].

There are two different configurations used to realize sub-Doppler cooling, which are related to the two distinct configurations of polarization gradients. The first is illustrated by two orthogonal, linearly polarized counter-propagating laser beams which have the same intensity and wavelength (lin $\perp$ lin configuration). The second is by using two orthogonal, counter-propagating laser beams having circular polarization (σ^+- σ^- configuration). The mechanism involving two orthogonal, linearly polarized, counter propagating beams is shown in Fig. 5. Using Eq. (22), it is shown that the polarization varies from linear to circular with a period of $\lambda/2$ where $k = 2\pi/\lambda$. There are four alternating linear to circular polarization changes for each period $\lambda/2$, the polarization state everywhere can be expressed as a superposition of two circular polarization states with vectors $(\hat{e_x} \pm \hat{e_y})/\sqrt{2}$. In contrast, for σ^+- σ^- configuration, the resulting light field has a constant magnitude and is linearly polarized everywhere but the direction rotates through an angle 2π every λ. In this case, the light shift is independent of position because the polarization is linear everywhere and the optical pumping mechanism is different than in the lin $\perp$ lin configuration.

Optical pumping is the transfer of population between atomic magnetic (Zeeman) sublevels. The optical pumping mechanism for the lin $\perp$ lin configuration is described in Fig. 6 for a $J = 1/2 \leftrightarrow J = 3/2$ transition. The Zeeman effect splits the ground state $J = 1/2$ to the $m_J = 1/2$ and $m_J = -1/2$ states, while the excited state is split

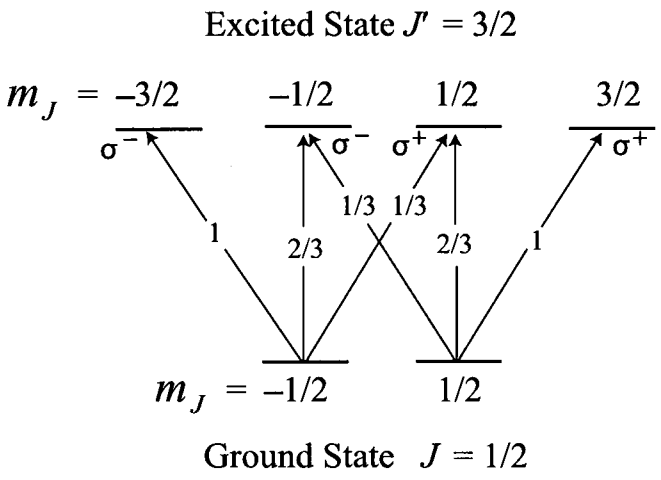

FIG. 6: Optical pumping in a $J = 1/2 - J = 3/2$ transition by σ^+, σ^-, and linearly polarized light. The Clebsch-Gordon coefficients for each allowable transition are shown.

to states with $m_J = -3/2$, $-1/2$, $1/2$, and $3/2$. Consider a point where the field is σ^+ circularly polarized. In such a field, atoms in a ground state $m_J = 1/2$ can only be coupled to the $m_J = 3/2$ excited state and decay back to the same ground state. Atoms with a ground state $m_J = -1/2$ can be coupled by the light field to $m_J = 1/2$ and decay back to either the $m_J = 1/2$ or $m_J = -1/2$ ground state. The Clebsch-Gordon coefficient for a transition from a ground state $m_J = 1/2$ to $m_J = 1/2$ is bigger than from a ground state $m_J = -1/2$ to $m_J = 1/2$, the atoms at $m_J = 1/2$ excited state are more likely to decay spontaneously to a ground state $m_J = 1/2$. The net result of the cycles of absorption and spontaneous emission in σ^+ circularly polarized light is the optical pumping of atoms from the $m_J = -1/2$ ground state to the $m_J = 1/2$ ground state which has lower energy. The optical pumping due to σ^- circularly polarized light works on the same principle as σ^+ circularly polarized light in the opposite sense; atoms from ground state $m_J = 1/2$ are pumped into $m_J = -1/2$ which has a lower energy.

As atoms move through a polarization-changing light field, the atoms must increase their potential energy (climb a hill) to overcome the polarization change. The ground state $m_J = 1/2$ becomes less strongly coupled to the light field until the atom reaches the region where the light field has σ^- circular polarization and the atom is optically pumped to $m_J = -1/2$. In other words, as an atom reaches the top of

the hill and is about to start gliding down, optical pumping transfers the atom to another lowest energy ground state, the previously gained potential energy carried away by the spontaneously emitted photon, again the atoms are at the bottom of the hill, and start to climb until they reach the next different polarized light field. This cooling mechanism reminded Dalibard and Cohen-Tannoudji of the Greek myth Sisyphus who was punished to keep pushing a heavy rock up hill hence they named the technique "Sisyphus cooling" [51, 18]. Like Sisyphus, the atom is running up potential hills more frequently than down. When it climbs a potential hill, its kinetic energy is transformed into potential energy. Dissipation then occurs by light, since the spontaneously emitted photon has an energy higher than the absorbed laser photon. After each Sisyphus cycle, the total energy E of the atom decreases by an amount of the order of U_0, where U_0 is the depth of the optical potential wells of Fig. 7. When E becomes smaller than U_0, the atom remains trapped in the potential wells with final Sisyphus cooling temperature $T_{\rm Sis}$ given by

$$T_{\rm Sis} \simeq \frac{U_0}{k_{\mathbf{B}}}. \tag{24}$$

We ignored in this discussion the recoil energy due to the spontaneously emitted photons which increase the kinetic energy of the atom by an amount on the order of

$$E_{\rm rec} = \frac{\hbar^2 k^2}{2M} \tag{25}$$

where $E_{\rm rec}$ is the recoil energy of an atom absorbing or emitting a single photon. When U_0 becomes on the order or smaller than $E_{\rm rec}$, the cooling due to the Sisyphus mechanism becomes weaker than the heating due to the recoil, and Sisyphus cooling no longer works. This shows that the lowest temperatures which can be achieved with such a scheme, the so-called recoil temperature, is given by

$$T_{\rm rec} = \frac{E_{\rm rec}}{k_{\rm B}} = \frac{\hbar^2 k^2}{2M k_{\rm B}}. \tag{26}$$

Typical values for $T_{\rm rec}$ of atoms are of the order of 1μK. This means $T_{\rm Sis}$ is on the order of a few micro-Kelvins for rubidium atoms.

In a low intensity field and with large detuning, redistribution between these ground states due to optical pumping can be slow compared to the change of light polarization, therefore the process is not adiabatic. Since the optical pumping takes out the energy of atoms (energy loss) as the atoms move, the efficiency of this cooling

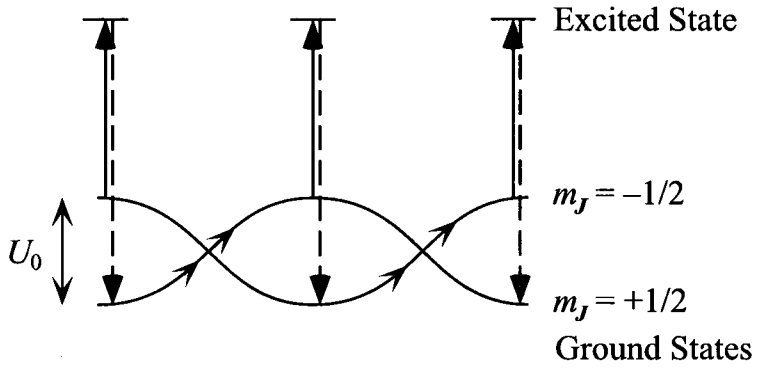

FIG. 7: Sisyphus cooling mechanism. For an atom with two ground state sublevels $m_J = \pm 1/2$, the spatial modulation of the laser polarization results in correlated spatial modulations of the light shifts of these two ground state sublevels and of the optical pumping rates between them.

mechanism depends on the velocity of the atoms. Sisyphus cooling works best for optimum velocity $v_s \approx \lambda/4\tau_p$ or when the atoms undergo one optical pumping process while traveling over a distance $\lambda/4$ [42, 48]. Atoms which are moving too fast do not respond to the optical pumping hence they do not lose energy, while atoms which are moving too slowly will be pumped to other sublevels before reaching the hill and hence lose less energy. The damping force $F = -\beta v$ for this mechanism can be estimated from the distance dependence of the energy loss. Using relations $\tau_p \equiv 1/\gamma_p$ and $v_s \cong \gamma_p/k$, the force at the optimum velocity can be written as

$$F = \triangle W/\Delta z \cong \Delta E\ k \equiv -\beta v_s, \tag{27}$$

where τ_p is the pumping time, γ_p is the pumping rate which is related to the scattering rate, β is the friction coefficient or the damping rate that needs to be estimated, and ΔE is the energy shift. At large detuning $|\Delta| \gg \Gamma$ the pumping rate becomes $\gamma_p = s\Gamma^3/4\Delta^2$. By choosing $C_{\rm ge}^2 = 1$, the damping rate and the energy shift can be written as

$$\beta/M = \hbar k^2 \Delta/2M\Gamma, \quad \Delta E = \frac{\hbar\Gamma^2 s}{4\Delta}. \tag{28}$$

It can be shown that by comparing the damping coefficient of Doppler cooling from Eq. (10), the damping rate of sub-Doppler cooling is larger by a factor of $2|\Delta|/\Gamma$ and it does not depend on the laser intensity while the energy shift and the pumping rate depend on the intensity. The damping force is smaller compared to the damping

force due to Doppler cooling, however, the damping coefficient becomes larger when the pumping rate becomes smaller, because the optimum velocity becomes smaller also.

Loading the ultracold atoms from a Magneto-Optical Trap (as will be explained in the next chapter) to an Optical Dipole Force Trap needs an efficient method of cooling during the loading process. Once the atoms are trapped, further cooling can be applied to achieve high phase-space density and lower temperature if needed for further applications. Doppler cooling has been used frequently to cool the atoms during loading while sub-Doppler cooling has also been used for improving the loading efficiency and to cool the trapped atoms. A Magneto-Optical Trap can provide a temperature down to 10 $T_{\rm rec}$ when its operation is optimized by sub-Doppler cooling. Other cooling techniques that are most commonly used for cooling the trapped atoms are Raman cooling, sideband cooling, evaporative cooling, and adiabatic cooling [52].

II.4 MAGNETO-OPTICAL TRAP

Doppler cooling in a one-dimensional molasses can be extended into three dimensions by using six laser beams. The optical molasses alone does not trap atoms, the atoms simply perform a spatially diffusive random walk and there is no confinement in space. The scattering force, which is velocity-dependent, however can be made position-dependent. The position-dependent force is created by adding an inhomogeneous magnetic field to an optical molasses which is built using circularly polarized laser beams. The configuration is known as a magneto-optical trap (MOT) which was originally conceived by Chu *et al.* upon suggestion by Dalibard [15]. A complete study of the MOT including the development of the external cavity diode laser system used as the MOT laser beams was demonstrated by Wieman and co-workers [53, 54] and has become a standard procedure to produce ultracold atoms.

The details of atom dynamics in a MOT in three dimensions are rather sophisticated to illustrate here, therefore, we will use the simple one-dimensional case to explain the basic principles. For an atom with a $J = 0$ ground state and a $J = 1$ excited state in a gradient magnetic field, the excited state splits into three Zeeman sublevels with $m_J = -1$, 0, and 1 (Fig. 8). If the atom is illuminated by circularly-polarized counter-propagating laser beams with frequency ω in the z-direction, because of its polarization orientation, the beam from the left can only excite transitions to the $m_J = +1$ state while the beam from the right can only excite transitions to the

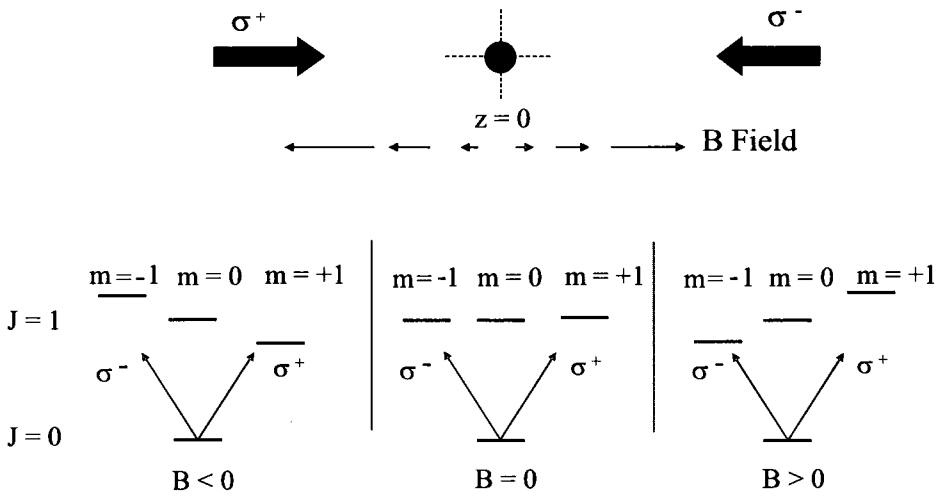

FIG. 8: The magneto-optical trap (MOT) in one dimension. The top part of the diagram shows a one-dimensional MOT with a pair of circularly-polarized counter-propagating beams and a magnetic field gradient which is zero at the center and increases linearly from the center. The bottom of the diagram shows schematically the Zeeman shifting of a $J = 0$ to $J = 1$ transition with an allowable transition related to the circular polarized laser light.

$m_J = -1$ state. The magnetic field is zero at the origin $z = 0$ and varies along the z axis. For an atom at $z > 0$, the magnetic field shifts the energy levels so that the $\Delta m_J = -1$ transition shifts to lower frequency while the $\Delta m_J = +1$ transition shifts to higher frequency. Since the laser frequency is detuned below the atomic resonance frequency, it is now closer to the $\Delta m_J = -1$ transition frequency. So this atom is more likely to scatter σ^- photons than σ^+ photons, and thereby get pushed back towards $z = 0$. For an atom at $z < 0$, the opposite happens, the magnetic field shifts the the energy levels so that the $\Delta m_J = +1$ transition shifts to lower frequency while the $\Delta m_J = -1$ transition shifts to higher frequency. The laser frequency is closer to the $\Delta m_J = +1$ transition frequency, and the atom will scatter the σ^+ laser light and get pushed back towards $z = 0$. An atom at $z = 0$ sees no net radiation pressure because of the two counter propagating beams and hence remains in its position.

In this configuration, the damping force or the scattering force in Eq. (10) which is due to the optical molasses gets a position dependence resulting in a trapping force or a restoring force which is proportional to position z,

$$\vec{F}_{\text{av}} = -\kappa_1 \vec{v} - \kappa_2 \vec{z}. \tag{29}$$

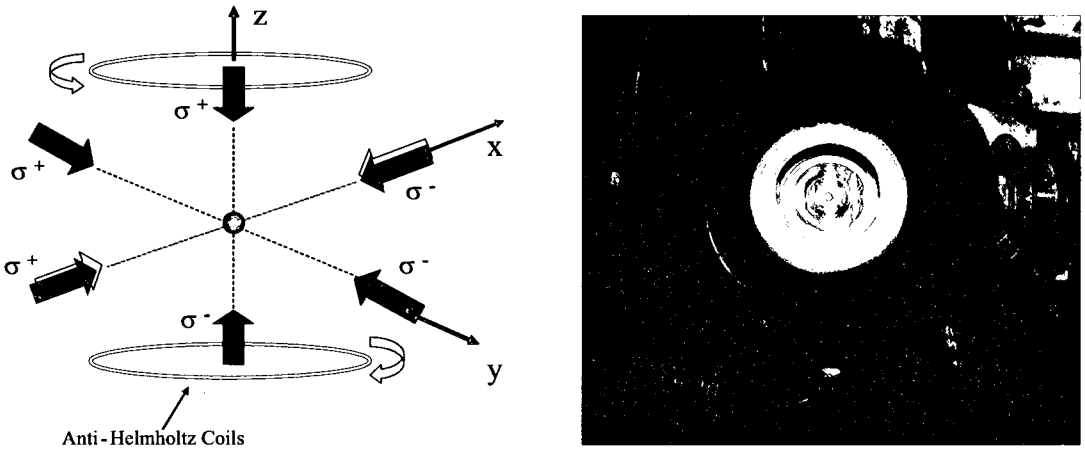

(a) (b)

FIG. 9: The magneto-optical trap (MOT) in three dimensions is comprised of 3 sets of counter-propagating beams (solid black arrow) with two opposite circular polarizations and a pair of anti-Helmholtz coils to create a magnetic field gradient, with zero at the center (a). There is also a pair of repump beams (white arrow) which optically pumps atoms that decay to different ground states by off-resonance transitions. The MOT cloud is seen at the center of a vacuum chamber (b).

Here κ_1 is the damping coefficient as defined in Eq. (10), κ_2 is the spring constant of the restoring force which depends on the magnetic moment for the transitions used and the magnetic field strength (Zeeman shifts) [42]. Eq. (29) is an equation of a damped harmonic oscillator. So the atoms in the MOT undergo a damped harmonic motion with the damping rate given by $\Gamma_{\rm MOT} = \kappa_1/M$ and the oscillation frequency $\omega_{\rm MOT} = \sqrt{\kappa_2/M}$.

The three-dimensional MOT is illustrated in Fig. 9 (a). The MOT is built using three sets of counter-propagating laser beams with opposite circular polarizations and a pair of anti-Helmholtz coils with opposite electric current to create a gradient magnetic field. In Fig. 9 (b), a MOT cloud at the center of a vacuum chamber is shown.

II.5 OPTICAL DIPOLE FORCE TRAP

The optical dipole force trap can be looked at from two different physical approaches. First, the atom is considered as a simple classical or quantum-mechanical oscillator

and then in the second approach, we consider the atom as a multilevel system [52].

When placing a polarizable atom into a laser light source, the electric field $\vec{\mathcal{E}}$ of the light induces an atomic dipole moment $\vec{d}$ that oscillates at the applied laser frequency ω. The amplitude of the dipole moment is proportional to the electric field amplitude and is given by:

$$\tilde{d} = \alpha(\omega)\,\mathcal{E}. \tag{30}$$

Here, $\alpha(\omega)$ is the complex polarizability which depends on the field frequency ω. The interaction potential of the induced dipole moment $\vec{d}$ in the driving field $\vec{\mathcal{E}}$ is given by

$$U_{\rm dip}(r) = -\frac{1}{2}\langle \vec{d}\cdot\vec{\mathcal{E}}\rangle = -\frac{1}{2\epsilon_0 c}\,\mathrm{Re}(\alpha)\,I, \qquad I = 2\epsilon_0 c|\mathcal{E}|^2. \tag{31}$$

In Eq. (31), the angular brackets denote the time average over the rapidly oscillating terms, I is the field intensity and the factor $\frac{1}{2}$ takes into account that the dipole moment is an induced, not a permanent one. The optical dipole force arises from the dispersive interaction of the dipole moment with the intensity gradient of the light field which is given as the gradient of $U_{\rm dip}$:

$$\vec{F}_{\rm dip}(\vec{r}) = -\nabla U_{\rm dip}(\vec{r}) = \frac{1}{2\epsilon_0 c}\,\mathrm{Re}(\alpha)\,\nabla I(\vec{r}). \tag{32}$$

So the optical dipole force is a conservative force which is proportional to the gradient of the field intensity. It acts in the direction of the gradient of the laser intensity while the dissipative force for laser cooling (radiation pressure or scattering force) acts in the direction of laser propagation.

The power absorbed by the oscillator from the driving field (and re-emitted) as dipole radiation is given by

$$P_{\rm abs} = \langle \dot{\vec{d}}\cdot\vec{\mathcal{E}}\rangle = 2\omega\ \mathrm{Im}(d\,\mathcal{E}^*) = \frac{\omega}{\epsilon_0 c}\,\mathrm{Im}\,(\alpha)\ I. \tag{33}$$

The absorption results from the imaginary part of the polarizability, which describes the out-of-phase component of the dipole oscillation. By considering the light as a stream of photons with photon energy $\hbar\omega$, the absorption can be interpreted in terms of photon scattering in cycles of absorption and subsequent spontaneous re-emission. The scattering rate can be defined as

$$\Gamma_{\rm scat} = \frac{P_{abs}}{\hbar\omega} = \frac{1}{\hbar\epsilon_0 c}\,\mathrm{Im}\,(\alpha)\ I. \tag{34}$$

The interaction potential in Eq. (31) and the scattering rate in Eq. (34) are the two main parameters that are always considered in the discussion of optical dipole force

traps. Creating a deep interaction potential well while having a low scattering rate is the main goal in building an optical dipole force trap.

In order to come up with applicable expressions for both parameters, the frequency dependent polarizability $\alpha(\omega)$ is derived. The derivation starts by considering the atoms as a *Lorentzian atom*, which consists of an electron elastically bound to a core with an eigenfrequency ω_0 corresponding to the optical transition frequency. In the oscillating light field, the atom (electron) behaves as a driven oscillator whose oscillation is driven by the light field. The polarizability is obtained by solving the equation of motion for the driven oscillation of the electron,

$$\ddot{x} + \Gamma_\omega \dot{x} + \omega_0^2 x = -eE(t)/m_e, \tag{35}$$

with the result being

$$\alpha = \frac{e^2}{m_e} \frac{1}{\omega_0^2 - \omega^2 - i\omega\Gamma_\omega}. \tag{36}$$

Here, Γ_ω is the classical damping rate due to the radiative energy loss, it is given by

$$\Gamma_\omega = \frac{e^2\omega^2}{6\pi\epsilon_0 m_e c^3}. \tag{37}$$

By extracting e^2/m_e from Eq. (37), introducing $\Gamma \equiv \Gamma_{\omega_0} = (\omega_0/\omega)^2\, \Gamma_\omega$ and substituting into Eq. (36), the classical polarizability is written as

$$\alpha = 6\pi\epsilon_0 c^3 \frac{\Gamma/\omega_0^2}{\omega_0^2 - \omega^2 - i(\omega^3/\omega_0^2)\Gamma}. \tag{38}$$

The polarizability can also be calculated using a semi-classical approach by considering the atom as a multilevel quantum system interacting with the classical radiation field. The damping rate for the semi-classical approach, which corresponds to the spontaneous decay rate of the excited level, is calculated using the dipole matrix element between the ground state and the excited states. One finds that when saturation effects can be neglected, which is true in our experiment (the far detuned case, very low saturation), the semi-classical result is similar to the classical calculation above. Therefore it can be used in deriving the dipole potential and the scattering rate in the case of large detuning and low scattering rate. So using Eq. (38), the dipole potential in Eq. (31) is written as

$$U_{\text{dip}}(\vec{r}) = -\frac{3\pi c^2}{2\omega_o^3}\left(\frac{\Gamma}{\omega_0 - \omega} + \frac{\Gamma}{\omega_0 + \omega}\right) I(\vec{r}), \tag{39}$$

and the scattering rate in Eq. (34) is given by

$$\Gamma_{\text{scat}}(\vec{r}) = \frac{3\pi c^2}{2\hbar\omega_0^3}\left(\frac{\omega}{\omega_0}\right)^3\left(\frac{\Gamma}{\omega_0-\omega}+\frac{\Gamma}{\omega_0+\omega}\right)^2 I(\vec{r}). \tag{40}$$

Eqs. (39) and (40) show two resonant contributions at $\omega = \omega_0$ and $\omega = -\omega_0$. In most experiments, the laser is tuned relatively close to the resonance ω_0 such that $\Delta \equiv \omega - \omega_0 \ll \omega_0$, in this case the second term in the equations above can be neglected and this approximation is known as the *rotating wave approximation* (RWA), hence the equation can be simplified to

$$U_{\text{dip}}(\vec{r}) = \frac{3\pi c^2}{2\omega_0^3}\frac{\Gamma}{\Delta} I(\vec{r}), \tag{41}$$

and the scattering rate in Eq. (34) is given by

$$\Gamma_{\text{scat}}(\vec{r}) = \frac{3\pi c^2}{2\hbar\omega_o^3}\left(\frac{\Gamma}{\Delta}\right)^2 I(\vec{r}). \tag{42}$$

Eqs. (41) and (42) can also be derived from a quantum mechanical point of view where the interaction of atoms with the light radiation field is represented by a time-dependent Schrödinger equation. The Hamiltonian for the interaction with the radiation field $\vec{E}(\vec{r},t)$ is given by [42, 52]

$$\mathcal{H}_1(t) = -\vec{\mu}\cdot\vec{E}(r,t)\,,\ \vec{\mu} = -e\vec{r}. \tag{43}$$

Here $\vec{\mu}$ is the electric dipole operator. The solution of the total Hamiltonian leads to an energy shift of the ith unperturbed energy ε_i which can be written as

$$\Delta E_i = \sum_{j\neq i}\frac{|\langle j|\mathcal{H}_1|i\rangle|^2}{\varepsilon_i-\varepsilon_j}. \tag{44}$$

For a two-level atom, using the "dressed state" picture [55], Eq. (44) simplifies to

$$\Delta E = \pm\frac{|\langle e|\mu|g\rangle|^2}{\Delta}|\mathcal{E}|^2 = \pm\frac{3\pi c^2}{2\omega_0^3}\frac{\Gamma}{\Delta}I, \tag{45}$$

where I is defined from Eq. (31). This perturbative result for the energy shifts reveals a very important fact that the ground state of the atoms gets shifted by the amount in Eq. (45) while the excited state get shifted in the opposite direction which is known as the AC Stark shift. This equation gives the same result as Eq. (41).

For the red-detuned case, the detuning Δ is less than zero since the laser frequency is tuned below atomic resonance, the dipole potential is negative and atoms are

attracted into the light field. The minimum of the potential is found at the position where the intensity is maximum. In relation to Eq. (45), for the low saturation case, the atoms spend most of their time in the ground state, the light-shifted ground state can be interpreted as the relevant potential for the motion of the atoms. This red detuned trap is easily built using a single focused Gaussian laser beam where the atoms are trapped at the focus. For the blue detuned case, the detuning is larger than zero, the dipole interaction repels atoms out of the field and the potential is minima at the minima intensity. This kind of trap is likely hard to build since the laser beam used needs to have a minimum at the center (box-like potentials with hard repulsive wall).

Eqs. (41) and (42) are also valid for the far-off-resonance trap (FORT). In contrast, if the laser frequencies are much lower than the atomic resonance frequency, the polarizability is considered to be well approximated by its zero frequency (DC) value. The trap using this laser light is known as a quasi-electrostatic trap (QUEST). This trap does not rely on a specific transition, therefore it can trap all internal states of an atom simultaneously, as well as different atomic or molecular species. For the FORT, as in Eq. (41) and (42), the dipole potential scales as I/Δ and the scattering rate scales as I/Δ^2. The relation between the dipole potential and the scattering rate can be written as

$$\hbar\Gamma_{\text{scat}} = \frac{\Gamma}{\Delta} U_{\text{dip}}. \tag{46}$$

To have an optical dipole force trap with a very low scattering rate at a given potential depth, it is desirable to use laser light with high intensity and very large detuning.

For multi-level atoms that have fine structure such as in alkali-metal atoms, the potential in Eq. (41) is modified to include the effect of two D-lines in the fine structure,

$$U_{\text{dip}} = \frac{\pi c^2 \Gamma}{2\omega_o^3} \left(\frac{1}{\Delta_{\text{D}_1}} + \frac{2}{\Delta_{\text{D}_2}} \right) I, \tag{47}$$

and the scattering rate in Eq. (42) is given by

$$\Gamma_{\text{scat}} = \frac{\pi c^2 \Gamma^2}{2\hbar\omega_o^3} \left(\frac{1}{\Delta_{\text{D}_1}^2} + \frac{2}{\Delta_{\text{D}_2}^2} \right) I. \tag{48}$$

Here Δ_{D_1} and Δ_{D_2} are detunings from the D_1 and D_2 lines, respectively. These formulas are valid for the case of large detuning compared to the excited state hyperfine splitting and the excited state linewidth and for linearly polarized laser light. For ^{85}Rb with the transition $5^2\text{S}_{1/2} - 5^2\text{P}_{1/2}$ for the D_1 line and the transition $5^2\text{S}_{1/2} -$

$5^2P_{3/2}$ for the D_2 line, and with $I_{sat} = 2\pi^2\hbar c\Gamma/3\lambda^3$ as the saturation intensity, Eqs. (47) and (48) can be rewritten as

$$U_{dip} = \frac{\hbar\Gamma^2 I}{24 I_{sat}}\left(\frac{1}{\Delta_{1/2}} + \frac{2}{\Delta_{3/2}}\right), \tag{49}$$

and the scattering rate in Eq. (34) is given by

$$\Gamma_{scat} = \frac{\Gamma^3 I}{24 I_{sat}}\left(\frac{1}{\Delta_{1/2}^2} + \frac{2}{\Delta_{3/2}^2}\right). \tag{50}$$

As mentioned earlier, for the red detuned case, the minima of the potential is found at the position where the intensity is maximum and thereby a trap can easily be built using a single focused Gaussian laser beam. The general equation for a focused Gaussian beam of peak intensity I_0 is written as [56]

$$I(z,r) = I_0 \frac{w_0^2}{w^2(z)} e^{-2r^2/w^2(z)}. \tag{51}$$

Here $I_0 = 2P/\pi w_0^2$ = the peak intensity at the waist, w_0 is the minimum spot size (waist size), z and r are the axial and radial position, respectively, and $w(z)$ is the $1/e^2$ radius at z and r,

$$w(z) = w_0\sqrt{1 + (\frac{z - z_0}{z_R})^2}, \tag{52}$$

where $r = \sqrt{x^2 + y^2}$, an $z_R = \pi w_0^2/\lambda$ is the Rayleigh range. z_0 is the axial position at $w(z) = w_0$. The experimental form of the potential energy for a red-detuned FORT then is given by

$$U(z,r) = -U_0 \frac{w_0}{w^2(z)} e^{-2r^2/w^2(z)}. \tag{53}$$

U_0 is the minimum potential (well depth) of the trap at $z = 0$ and $r = 0$ which is already given in Eq. (89). For radial shape ($z = 0$), Eq. (53) is rewritten as

$$U(r) = -U_0 e^{-2r^2/w_0^2}. \tag{54}$$

II.6 MAGNETIC TRAP

Magnetic traps are used to confine the ultracold atoms produced by laser cooling by exerting a force from a magnetic field gradient on the atomic magnetic dipole moment without the downside of laser heating as in a FORT. If the initial atomic density is sufficiently high, the simple technique of evaporative cooling in the magnetic trap allows experiments to reach quantum degeneracy where the occupation of the quantum states approaches unity. This leads either to Bose–Einstein condensation (BEC) or to Fermi degeneracy, depending on the spin of the atoms [57].

II.6.1 Principle of magnetic trapping

Similar to the famous Otto Stern and Walter Gerlach experiment in which the force on an atom as it passed through a strong inhomogeneous magnetic field was used to separate the spin states in a thermal atomic beam, magnetic trapping uses the force produced by a system of magnetic field coils to bend the trajectories of cold atoms within a small region close to the center of the trap.

A magnetic dipole moment μ in a magnetic field has energy

$$U = -\vec{\mu} \cdot \vec{B}. \tag{55}$$

For an atom in the state $|I, J, F, m_F\rangle$ this corresponds to a Zeeman energy

$$U = g_F \mu_B m_F B. \tag{56}$$

The energy depends only on the magnitude of the field $B = |\vec{B}|$. The energy does not vary with the direction of $\vec{B}$ because as the dipole moves (adiabatically) it stays aligned with the field. From this we find the magnetic force along the z-direction:

$$F = -g_F \mu_B m_F \frac{\mathrm{d}B}{\mathrm{d}z}. \tag{57}$$

II.6.2 Confinement in the radial direction

Assume the four parallel wires arranged at the corners of a square (Fig. 10) which produce a quadrupole magnetic field when the currents in adjacent wires flow in opposite directions. Clearly this configuration does not produce a field gradient along the axis (z-direction), therefore from Maxwell's relation $\mathrm{div}\vec{B} = 0$ we deduce that

$$\frac{\mathrm{d}B_x}{\mathrm{d}x} = -\frac{\mathrm{d}B_y}{\mathrm{d}y} = b'. \tag{58}$$

These gradients have the same magnitude b', but opposite sign. Therefore the magnetic field has the form

$$\vec{B} = b'(x\hat{\mathrm{e}}_x - y\hat{\mathrm{e}}_y) + \vec{B}_0. \tag{59}$$

In the special case of $B_0 = 0$, the field has a magnitude

$$\left|\vec{B}\right| = b'(x^2 + y^2)^{1/2} = b'r. \tag{60}$$

Thus the magnetic energy in Eq. (56) has a linear dependence on the radial coordinate $r = \sqrt{x^2 + y^2}$. This conical potential has the V-shaped cross-section shown in Fig. 11(a), with a force in the radial direction of

$$\vec{F} = -\nabla U = -g_F \mu_B m_F b' \hat{\mathrm{e}}_r. \tag{61}$$

This force confines atoms in a low-field-seeking state, i.e. one with $g_F m_F > 0$, so that the magnetic energy decreases as the atom moves into a lower field. However, a quadrupole field has a fundamental problem—the atoms congregate near the center where $B = 0$ and the Zeeman sublevels ($|I, J, F, m_F\rangle$ states) have a very small energy separation. In this region of very low magnetic field the states with different magnetic quantum numbers mix together and atoms can transfer from one value of m_F to another because of perturbations caused by noise or fluctuation in the field. These non-adiabatic transitions allow the atoms to escape and reduce the lifetime of atoms in the trap. A field $\vec{B}_0 = B_0 \hat{\mathrm{e}}_z$ along the z-axis, has the desired effect on the magnitude of the field near the center of the trap to prevent the atoms from escaping. Eq. (59) becomes

$$\left|\vec{B}\right| = \left[B_0^2 + (b'r)^2\right]^{1/2} \simeq B_0 + \frac{b'^2 r^2}{2B_0}. \tag{62}$$

This approximation works for small r where $b'r \ll B_0$. The bias field along z rounds the point of the conical potential, as illustrated in Fig. 11(b), so that near the z-axis the atoms of mass M see a harmonic potential. From Eq. (56) we find

$$U(r) = U_0 + \frac{1}{2} M \omega_r^2 r^2. \tag{63}$$

The radial oscillation has an angular frequency given by

$$\omega_r = \sqrt{\frac{g_F \mu_B m_F}{M B_0}} \times b'. \tag{64}$$

II.6.3 Confinement in the axial direction

The Ioffe trap, shown in Fig. 12, uses the combination of a linear magnetic quadrupole and an axial bias field described above to give radial confinement for

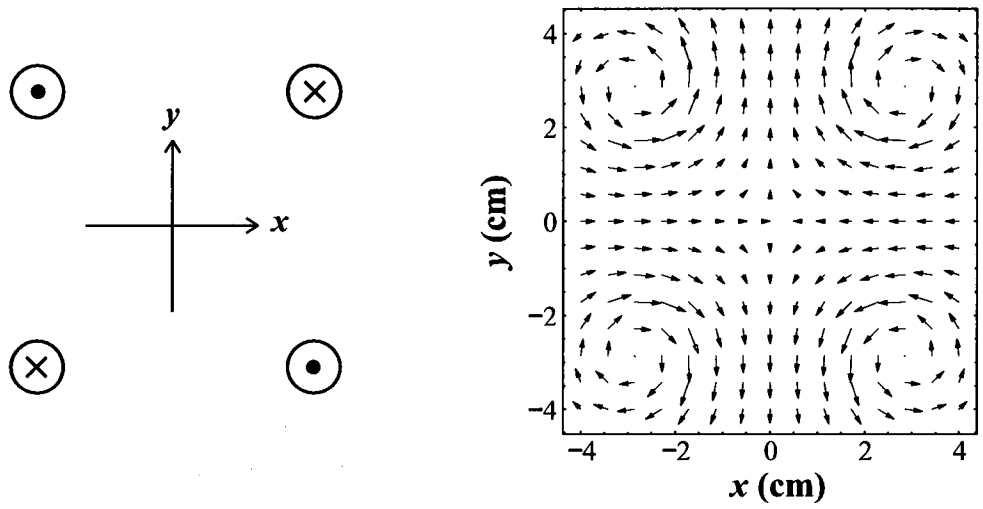

(a) (b)

FIG. 10: (a) Four parallel straight wires with currents into and out of the page as indicated. These create a magnetic quadrupole field. (b) The direction of the created magnetic field around the wires.

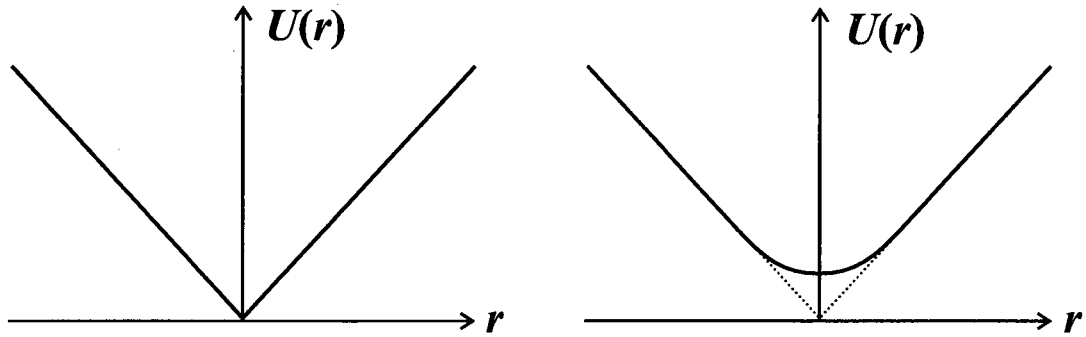

(a) (b)

FIG. 11: (a) The magnetic potential in a radial direction along the x- or y-axis. The cusp at the bottom of the conical potential leads to non-adiabatic transitions of the trapped atoms. (b) A bias field along the z-direction rounds the bottom of the trap to give a harmonic potential near the z-axis.

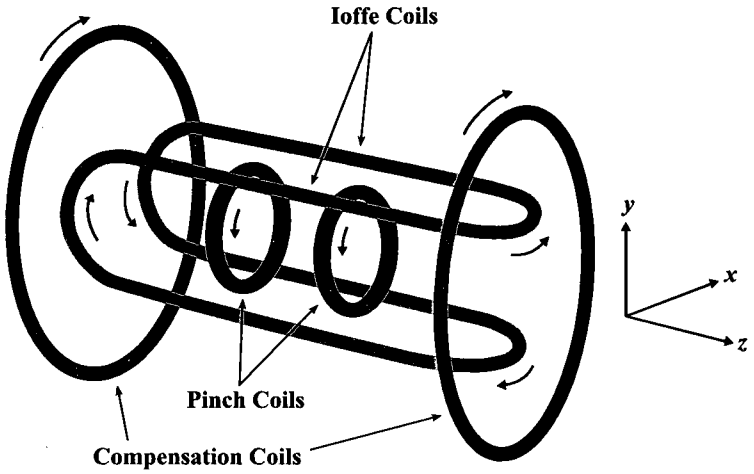

FIG. 12: The Ioffe–Pritchard magnetic trap. The different current directions are shown for each coil.

atoms in low-field-seeking states. To confine these atoms in the axial direction the trap has two pairs of co-axial coils with currents that flow in the same direction to produce a field along the z-axis whose magnitude is shown in Fig. 13. These so-called pinch coils have a separation greater than that of Helmholtz coils, so the field along z has a minimum midway between the coils (where $\mathrm{d}Bz/\mathrm{d}z = 0$). The field has the form

$$B_{pinch}(z) = B_{pinch}(0) + \frac{\mathrm{d}^2 B_z}{\mathrm{d}z^2}\frac{z^2}{2}. \tag{65}$$

This gives a corresponding minimum in the magnetic energy and hence a harmonic potential along the z-axis. Typically, the Ioffe trap has an axial oscillation frequency ω_z with an order of magnitude lower than ω_r, thus the atoms congregate in a cigar-shaped cloud along the z-axis. The curvature of the magnetic field along z depends only on the dimensions of the pinch coils and their current. Therefore a uniform field along z does not affect ω_z, but it does change ω_r through the dependence on B_0 in Eq. (64). The pairs of compensation coils shown in Fig. 12 create a uniform field along the z-axis that opposes the field from the pinch coils. This allows experimenters to reduce B_0 and make the trap stiff in the radial direction.

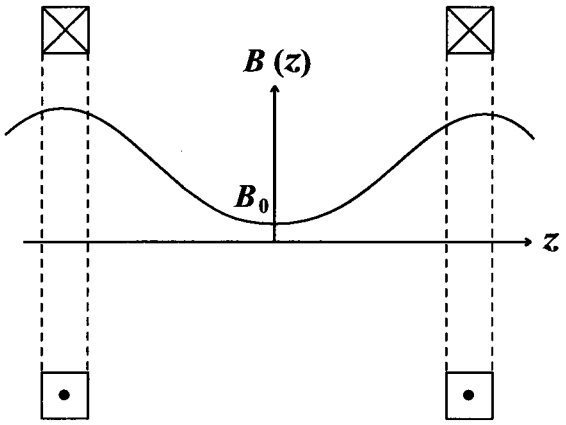

FIG. 13: The pinch coils have currents in the same direction as shown and create a magnetic field along the z-axis, with a minimum located midway between them at $z = 0$. This leads to a potential well for atoms in low-field-seeking states along this axial direction.

II.7 INHOMOGENEOUS BROADENING

The development in cooling and trapping of atoms was a very important step to achieve more precise spectroscopic measurements. When atoms are held in a trap, there is no Doppler broadening, but on the other hand, the trapping fields also perturb the internal states of the atoms in addition to holding them. In an optical trap opposite AC Stark shifts of the ground and excited states lead to a position-dependent shift in the resonance frequency and inhomogeneous broadening of the transition. For a two-level system in an optical trap, the AC Stark shift of the ground state and that of the excited state are opposite to each other, as shown in Fig. 14(a), which leads to an inhomogeneous broadening of a transition between the two levels. Such an inhomogeneously broadened AC Stark shift can turn off the Doppler cooling of atoms inside an optical trap [58]. When the multi-level nature of an atom is considered, however, the situation is different. The coupling between this first excited state with another higher excited state by a well chosen light field, can result in the same AC Stark shift for the ground state and the first excited state, Fig. 14(b). Such a situation has been identified in Cesium [59]. This will enable us to construct an optical dipole trap without the inhomogeneous AC Stark broadening to study its characteristics.

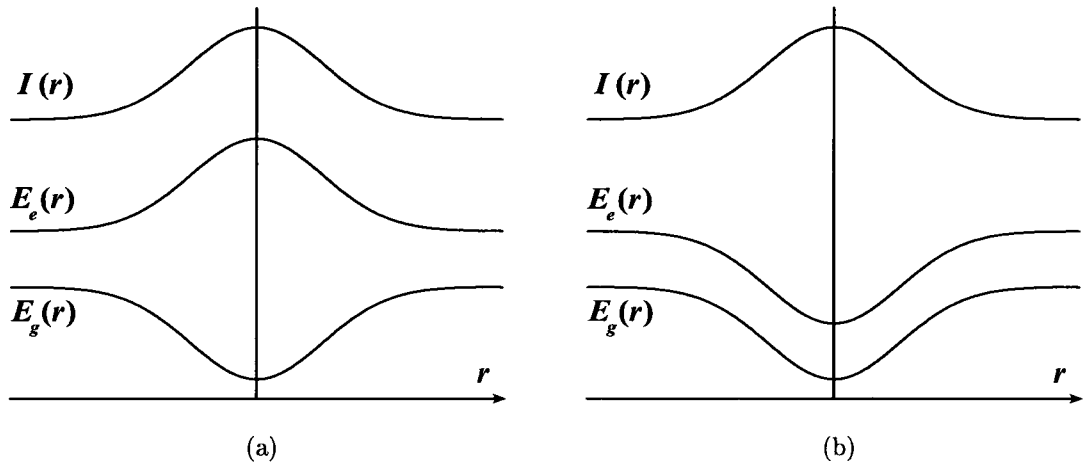

FIG. 14: (a) Energy levels of the ground and the excited states of a two-level atom inside an optical trap. $I(r)$ is the Gaussian intensity profile of a trap beam. (b) Energy levels of the two low-lying states in a three-level atom inside an optical trap with the addition of a second laser to eliminate the differential AC Stark shift.

One way to eliminate the differential AC Stark shift in an optical trap is the use of the vector polarizability of the atom. When the light is elliptically polarized, the circular component can give rise to a first-rank tensor interaction. The vector part of an AC Stark shift takes the form of a Zeeman shift, and one can associate an artificial magnetic field with the shift [60]. In particular, the pair of ground hyperfine levels of an alkali-metal atom have Landé g-factors of opposite sign, and with a proper polarization, the differential AC Stark shift from the scalar part can be canceled by the tensor part. The AC Stark shift in a spherical tensor form is presented as follows [61]:

When an alkali-metal atom in its ground state $|\Psi_0\rangle$ is illuminated by a laser field with an oscillating electric component $\vec{E}(t) = \vec{\mathcal{E}}e^{-i\omega t} + \vec{\mathcal{E}}^* e^{i\omega t}$ of angular frequency ω, it experiences an AC Stark shift given by,

$$U_{\mathrm{AC}}(\Psi_0) = \sum_{n\neq 0} \frac{\langle\Psi_0|\,\vec{d}\cdot\vec{\mathcal{E}}^*\,|\Psi_n\rangle\,\langle\Psi_n|\,\vec{d}\cdot\vec{\mathcal{E}}\,|\Psi_0\rangle}{\omega_0-\omega_n+\omega} + \sum_{n\neq 0} \frac{\langle\Psi_0|\,\vec{d}\cdot\vec{\mathcal{E}}\,|\Psi_n\rangle\,\langle\Psi_n|\,\vec{d}\cdot\vec{\mathcal{E}}^*\,|\Psi_0\rangle}{\omega_0-\omega_n-\omega}, \tag{66}$$

where atomic units are used. ω_n is the unperturbed energy eigenvalue of the state $|\Psi_n\rangle$ and $\vec{d}$ is the electric dipole moment (EDM) operator. The second term, which is

off-resonant, is much smaller than the first in most cases and can be ignored (however, for large detuning, it may not be neglected)

$$U_{\mathrm{AC}}(\Psi_0) \approx \sum_{n\neq 0} \frac{\langle\Psi_0|\,\vec{d}\cdot\vec{\mathcal{E}}^*\,|\Psi_n\rangle\,\langle\Psi_n|\,\vec{d}\cdot\vec{\mathcal{E}}\,|\Psi_0\rangle}{\omega_0-\omega_n+\omega}. \tag{67}$$

The AC Stark shift can be written as an expectation value

$$U_{\mathrm{AC}}(\Psi_0) = \langle\Psi_0|\,\Omega\left(\vec{\mathcal{E}},\omega\right)|\Psi_0\rangle\,, \tag{68}$$

with the operator Ω in the Cartesian form is given by

$$\Omega\left(\vec{\mathcal{E}},\omega\right) = \sum_{i,j}\mathcal{E}_i^* d_i\left(\omega_0 - H_0 + \omega\right)^{-1} d_j\mathcal{E}_j, \tag{69}$$

where H_0 is the unperturbed atomic Hamiltonian. $\mathcal{E}_i$ and d_i for $i = x, y, z$ are the Cartesian components of $\vec{\mathcal{E}}$ and $\vec{d}$, respectively. The Ω operator can be rewritten in a spherical tensor form,

$$\Omega\left(\vec{\mathcal{E}},\omega\right) = \sum_{L=0}^{2}(-1)^L\sum_{m=-L}^{L}(-1)^m\,\mathcal{D}_m^{(L)}(\omega)\mathcal{F}_{-m}^{(L)}, \tag{70}$$

where $\mathcal{D}^{(L)}$ and $\mathcal{F}^{(L)}$ with $L = 0, 1, 2$ are the scalar, vector and the second-rank spherical tensor operators:

$$\mathcal{D}_m^{(L)}(\omega) = (-1)^{m+1}\sqrt{2L+1}\sum_{\mu=-1}^{1}\begin{pmatrix}1 & 1 & L\\ \mu & m-\mu & -m\end{pmatrix} d_\mu(\omega_0 - H_0 + \omega)^{-1}d_{m-\mu}. \tag{71}$$

Here $d_0 = z$ and $d_{\pm 1} = \mp(x \pm iy)/\sqrt{2}$. $\mathcal{F}_m^{(L)}$ is similarly defined in terms of $\mathcal{E}_i^*$ and $\mathcal{E}_j$ [62]:

$$\mathcal{F}_0^{(0)} = \frac{1}{\sqrt{3}}|\vec{\mathcal{E}}|^2, \tag{72}$$

$$\mathcal{F}_m^{(1)} = -\frac{i}{\sqrt{2}}(\vec{\mathcal{E}}^*\times\vec{\mathcal{E}})_m, \tag{73}$$

$$\mathcal{F}_0^{(2)} = \frac{1}{\sqrt{6}}\left(|\vec{\mathcal{E}}|^2 - 3|\mathcal{E}_0|^2\right), \tag{74}$$

$$\mathcal{F}_{\pm 1}^{(2)} = -\frac{1}{\sqrt{2}}(\mathcal{E}_0^*\mathcal{E}_{\pm 1} + \mathcal{E}_{\pm 1}^*\mathcal{E}_0), \tag{75}$$

$$\mathcal{F}_{\pm 2}^{(2)} = -(\mathcal{E}_{\pm 1}^*\mathcal{E}_{\pm 1}), \tag{76}$$

where $\mathcal{E}_0 = \mathcal{E}_z$ and $\mathcal{E}_{\pm 1} = \mp(\mathcal{E}_x \pm i\mathcal{E}_y)/\sqrt{2}$.

The scalar term in Eq. (70) is proportional to $|\vec{\mathcal{E}}|^2$. The vector term leads to an AC Stark shift proportional to $\langle\Psi_0| \mathcal{D}^{(1)} |\Psi_0\rangle \cdot (\vec{\mathcal{E}}^* \times \vec{\mathcal{E}})$. The second-rank term is non-vanishing only if the total angular momentum of the state Ψ_0 is at least 1. Alkali metal atoms have a nuclear spin in addition to the electron spin. The resulting total angular momentum for the rubidium ground state, for example, is 2 or 3, and there is a contribution to the AC Stark shift from the second-rank term. However, when the detuning of the applied field from the D-transitions is much larger than the hyperfine splitting, as in a FORT, the second-rank term can be neglected. Under this approximation, the AC Stark shift of the ground hyperfine level $|nS_{1/2}, F, m_F\rangle$, where F is the total angular momentum and m_F is the magnetic quantum number, can be written as

$$U_{\mathrm{AC}} = -\alpha|\vec{\mathcal{E}}|^2 - i\beta \langle S_{1/2}, F, m_F| \vec{\sigma} |nS, F, m_F\rangle \cdot (\vec{\mathcal{E}}^* \times \vec{\mathcal{E}}), \tag{77}$$

where $\mathcal{D}^{(1)}$ in the vector term is replaced with the Pauli spin operator $\vec{\sigma}$ using the Wigner-Eckart theorem. α and β are the scalar and the vector polarizabilities, respectively.

The expression in Eq. (77) can be further simplified to

$$U_{\mathrm{AC}} = -\alpha|\vec{\mathcal{E}}|^2 - \beta g_F m_F \eta |\vec{\mathcal{E}}|^2, \tag{78}$$

where g_F is the Landé g-factor for the given F and $\eta = |\hat{\epsilon} \times \hat{\epsilon}^*|$ is a measure of ellipticity. $\hat{\epsilon}$ is the Jones vector representing the polarization state of $\vec{\mathcal{E}}$. When the trapping field is linearly polarized, $\eta = 0$ and the AC Stark shift takes a simple form of $U_{\mathrm{AC}} = -\alpha|\vec{\mathcal{E}}|^2$. Then we have for a linearly polarized field $\vec{E}(t) = \vec{\mathcal{E}}e^{-i\omega t} + \vec{\mathcal{E}}^* e^{i\omega t}$ of angular frequency ω, with $\vec{\mathcal{E}} = \mathcal{E}_0\hat{z}$, the energy shift of the $|5S_{1/2}, F, m_F\rangle$ state and that of the $|5P_{3/2}, F, m_F\rangle$ state in rubidium are given by [59]:

$$U_{\mathrm{AC}}\left(5S_{1/2}, F, m_F\right) = -\alpha_S \left|\mathcal{E}_0\right|^2, \tag{79}$$

$$U_{\mathrm{AC}}\left(5P_{3/2}, F, m_F\right) = -\alpha_P \left|\mathcal{E}_0\right|^2 - \gamma_P \frac{3m_F^2 - F(F+1)}{F(2F-1)} \left|\mathcal{E}_0\right|^2, \tag{80}$$

where α_S is the scalar polarizability of the $5S_{1/2}$ state, and α_P and γ_P are the scalar and the second-rank tensor polarizabilities of the $5P_{3/2}$ state, respectively.

The corresponding scattering rate Γ_{scat} after using the rotating wave approximation is given by [52]:

$$\Gamma_{\text{scat}}(r) = \frac{3\pi c^2}{2\hbar\omega_0^3}\left(\frac{\Gamma}{\Delta}\right)^2 I(r) \tag{81}$$

where Γ is the natural linewidth of the excited state, ω_0 is the resonance frequency of the transition between the ground state and the considered excited state (in our case it is the $5P_{3/2}$ state), Δ is the detuning from the resonance frequency, and I is the intensity of the laser used.

The scalar and tensor polarizabilities are given by [60, 62]:

$$\begin{aligned}\alpha &= \frac{1}{3}\sum_{n,J'}\frac{\left|\left\langle nSLJ\left\|D\right\|n'S'L'J'\right\rangle\right|^2}{(2J+1)} \\ &\quad\times\left(\frac{1}{\left[E(n,J)-E(n',J')\right]+\hbar\omega}+\frac{1}{\left[E(n,J)-E(n',J')\right]-\hbar\omega}\right)\end{aligned} \tag{82}$$

$$\begin{aligned}\gamma &= -\left[\frac{10J(2J-1)}{3(2J+3)(J+1)(2J+1)}\right]^{1/2}\sum_{n,J'}\left|\left\langle nSLJ\left\|D\right\|n'S'L'J'\right\rangle\right|^2 \\ &\quad\times\left(\frac{1}{\left[E(n,J)-E(n',J')\right]+\hbar\omega}+\frac{1}{\left[E(n,J)-E(n',J')\right]-\hbar\omega}\right) \\ &\quad\times(-1)^{J+J'+1}\left\{\begin{array}{ccc} J & J' & 1 \\ 1 & 2 & J\end{array}\right\}\end{aligned} \tag{83}$$

where the $\{\}$ indicates the $6j$ symbol. The reduced matrix element of D can be simplified by the following equation,

$$\left\langle nSLJ\left\|D\right\|n'S'L'J'\right\rangle = (-1)^{S+L'+J+1}\delta_{SS'}\left\{\begin{array}{ccc} J & J' & 1 \\ 1 & 2 & J\end{array}\right\}\left\langle L\left\|D\right\|L'\right\rangle \tag{84}$$

In the case of a single external electron we have

$$\left\langle l\left\|D\right\|l'\right\rangle = e(-1)^{l_>-l}\int R_n r R_{n'}\,dr \tag{85}$$

where $l_>$ means the greater of l and l'. The reduced matrix element in Eq. (85) can be replaced by the lifetime of the excited state considering the oscillator strengths of the possible transitions between that state and any other state.

For some atoms, like cesium, there exists a wavelength of the trapping light (magic wavelength) where the scalar polarizabilities of the ground state and the first excited state have the same value. This will lead to a similar AC Stark shift for both states, ignoring the second-rank tensor part of the excited state energy shift. Such a situation does not exist in rubidium, therefore another idea was implemented. If a laser that is red detuned from the $5P_{3/2}$ to one of the $5D_J$ resonance frequencies is used, these two states will be coupled which will result in a negative shift for the $5P_{3/2}$ state. Applying that laser with specific power and detuning along with the Nd:YAG laser on the atoms in the FORT, the $5S_{1/2}$ and $5P_{3/2}$ can have the same AC Stark shift, as in Fig. 14(b), which will eliminate the inhomogeneous broadening provided that the two lasers have the same spatial intensity profile. Calculation of the polarizabilities and the energy shift as functions of the wavelength of the applied second laser is given in Sec. IV.3.

II.8 THE AUTLER-TOWNES EFFECT

The interaction between the field of a laser beam and an atom can lead to a change in the absorption spectrum of the atom. Intense coupling lasers can create "dressed" atomic states [55] that make the absorption and dispersion of another weak probe laser change from one peak to multi-peaks. This effect is called the Autler-Townes splitting (or AC Stark effect). Originally, Autler and Townes developed a theory and proved experimentally the AC Stark splitting (named the Autler-Townes doublet) of energy levels driven by a microwave field [63]. The effect was later introduced into optics [64, 65] and then implemented in laser spectroscopy of ultracold atoms [66] which initiated numerous experiments to explore the features of two- and three-level atomic systems driven by resonant laser fields. The results of these experiments have made a significant step to precise spectroscopy and were used to measure the hyperfine intervals of atoms. Autler-Townes spectroscopy can also be used as a sensitive probe of atoms in an optical dipole force trap.

For example, let us consider the three-level Λ-type system in ^{87}Rb, where the coupling laser initiates the transition from one ground state, and the probe laser measures absorption from the other ground state. In this system, the coupling laser creates two dressed states due to the AC Stark shift and the probe absorption splits into an Autler-Townes doublet. When the coupling laser is detuned from resonance,

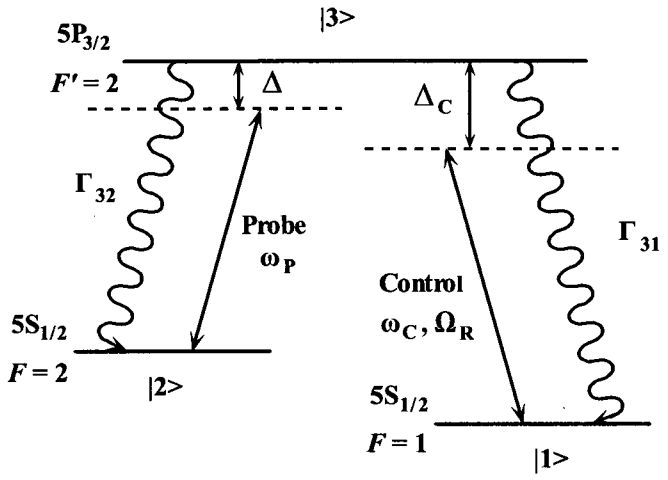

FIG. 15: Three-level Λ system in ^{87}Rb. The control laser drives the $|1\rangle \leftrightarrow |3\rangle$ transition with Rabi frequency Ω_R and detuning Δ_C. The probe laser measures the absorption on the $|1\rangle \leftrightarrow |2\rangle$ transition at a detuning Δ. Γ_{31} and Γ_{32} are the spontaneous decay rates from the excited state.

the two dressed states have asymmetric linewidths, such that their sum is the unperturbed linewidth. The basic energy levels and transitions are shown in Fig. 15. The lower levels $|1\rangle$ and $|2\rangle$ are the $F = 1$ and $F = 2$ hyperfine levels in the $5S_{1/2}$ ground state, while the upper level $|3\rangle$ is the $5P_{3/2}$ excited state. The excited state has four hyperfine levels, of these, only the levels with $F' = 1$ and 2 couple to both the lower levels and can act as level $|3\rangle$. The coupling laser induces the $|1\rangle \leftrightarrow |3\rangle$ transition with Rabi frequency Ω_R and detuning Δ_C. The weak probe laser measures the absorption on the $|1\rangle \leftrightarrow |2\rangle$ transition at a detuning Δ. The excited state lifetime is 26 ns, and therefore the spontaneous decay rates Γ_{31} and Γ_{32} are both equal to $2\pi \times 6.1$ MHz.

Due to the splitting of the upper level into two dressed states, the probe absorption shows peaks at the locations of the two dressed states given by

$$\Delta_\pm = \frac{-\Delta_C}{2} \pm \frac{1}{2}\sqrt{\Delta_C^2 + \Omega_R^2}, \tag{86}$$

where Δ_+ and Δ_- are the values of the probe detuning where the peaks occur. The corresponding linewidths ($\Gamma_\pm$) of these peaks are different because of the coherence between the two dressed states, and given by

$$\Gamma_{\pm} = \frac{\Gamma_{31} + \Gamma_{32}}{4} \left(1 \mp \frac{\Delta_C}{\sqrt{\Delta_C^2 + \Omega_R^2}} \right). \tag{87}$$

It is clear from the above Eq. (87) that, if $\Delta_C = 0$, the two peaks are symmetric and have identical linewidths of $(\Gamma_{31} + \Gamma_{32})/4$. However, for any nonzero detuning, the peaks have asymmetric linewidths. The first peak has a larger linewidth while the second peak has a smaller linewidth by precisely the same factor, in such a way that the sum of the two linewidths is equal to the unperturbed linewidth $(\Gamma_{31} + \Gamma_{32})/2$. While our three-level system in this example is Λ-type system, the Autler-Townes splitting will also be observed if coupling of the second laser is between excited states, as in our experiment.

CHAPTER III

THE EXPERIMENTAL APPARATUS

In this chapter, we describe the key components of the apparatus in which the spectroscopy experiments discussed in the next chapter are performed. The principal components of the system are 1) the semiconductor diode lasers used to make the magneto-optical trap (MOT); 2) the ultrahigh vacuum system where the atoms are trapped; 3) the Nd:YAG laser which forms the optical dipole force trap; 4) additional diode lasers used for spectroscopy; and 5) the data acquisition system. Of course, all of these items have a myriad of accompanying optics and electronics, as shown in the photographs of Fig. 16.

III.1 OVERVIEW

The experiment starts by loading the MOT using laser light which comes from a master-slave (also referred to as "injection-locked") diode laser system and a repump laser beam. Although it is common to derive the needed repump laser frequency by adding radio frequency (RF) sidebands to the trap laser, here the repump laser beam comes from a separate laser to enable full control over the intensity, detuning and switching of the repump light. The output of each laser system is coupled separately into a single mode fiber optic cable for easy alignment to the vacuum chamber. The fiber optic also serves as a spatial filter yielding a nice Gaussian beam at the exit of the fiber. The power of the trap laser beam after the fiber is about 8 mW, which is expanded in size to a $1/e^2$ intensity radius of 0.55 cm and divided into three beams, each of which is circularly polarized before entering the vacuum chamber. These three beams are then retro-reflected after passing through a second quarter wave plate. For the repump laser we have about 1 mW going into the chamber, expanded to the same size as that of the trap laser beam before going into the chamber. Two anti-Helmholtz coils with a magnetic field gradient of about 10 G/cm are used to trap the atoms in the MOT. We also use a set of shim coils to overcome the stray magnetic field around the chamber so the MOT can be formed at the center for easy alignment with the FORT beam. To obtain a stable MOT, we first stabilize the trapping and repump lasers using Doppler free saturated absorption spectroscopy. After a stable MOT is observed, we overlap the MOT with the waist of the far-off-resonance-trap

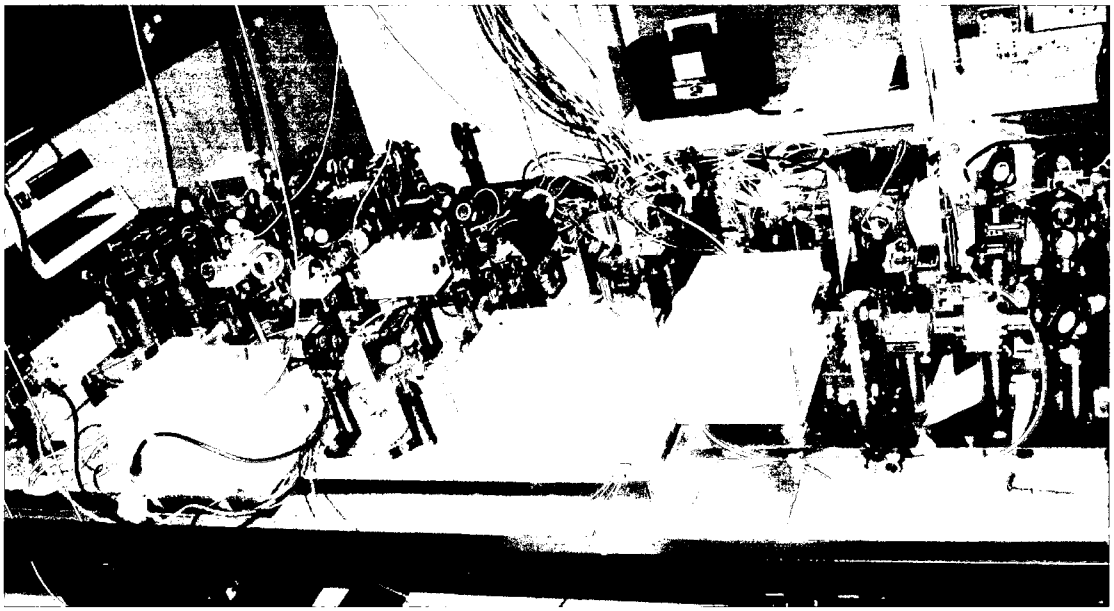

(a) Laser Table

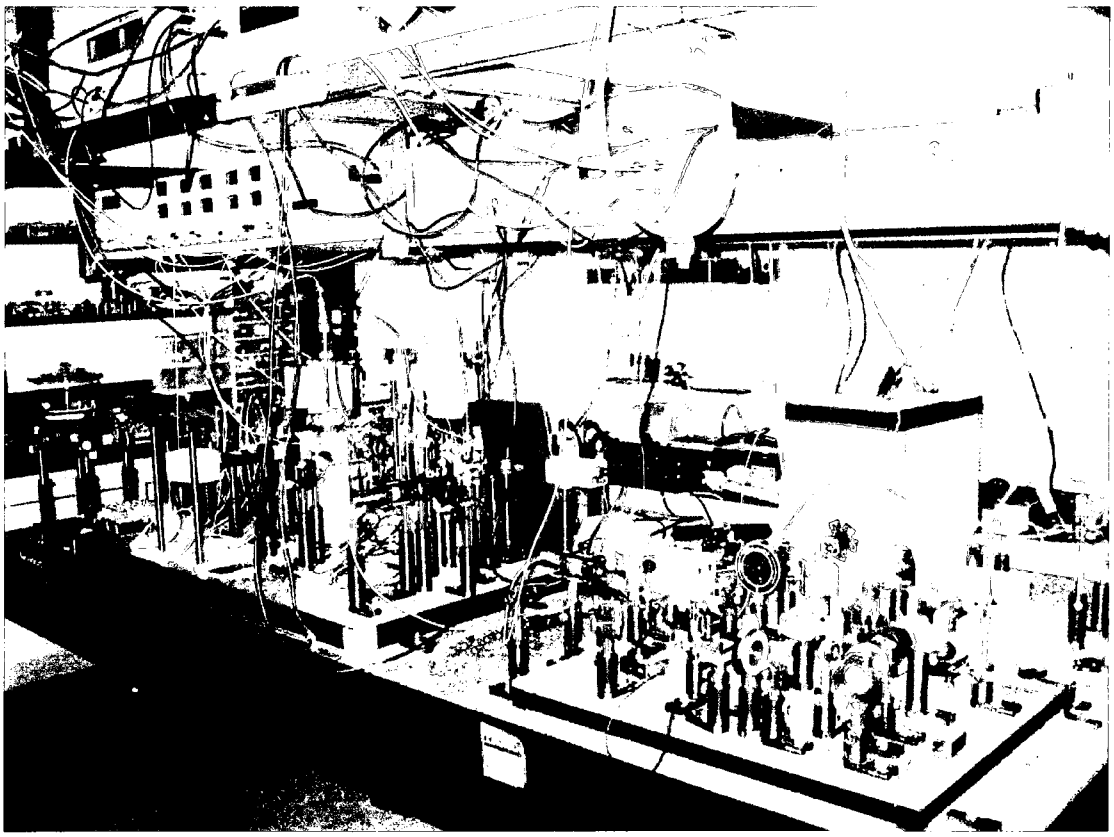

(b) Science Chamber Table

FIG. 16: Laser and Science Chamber Tables

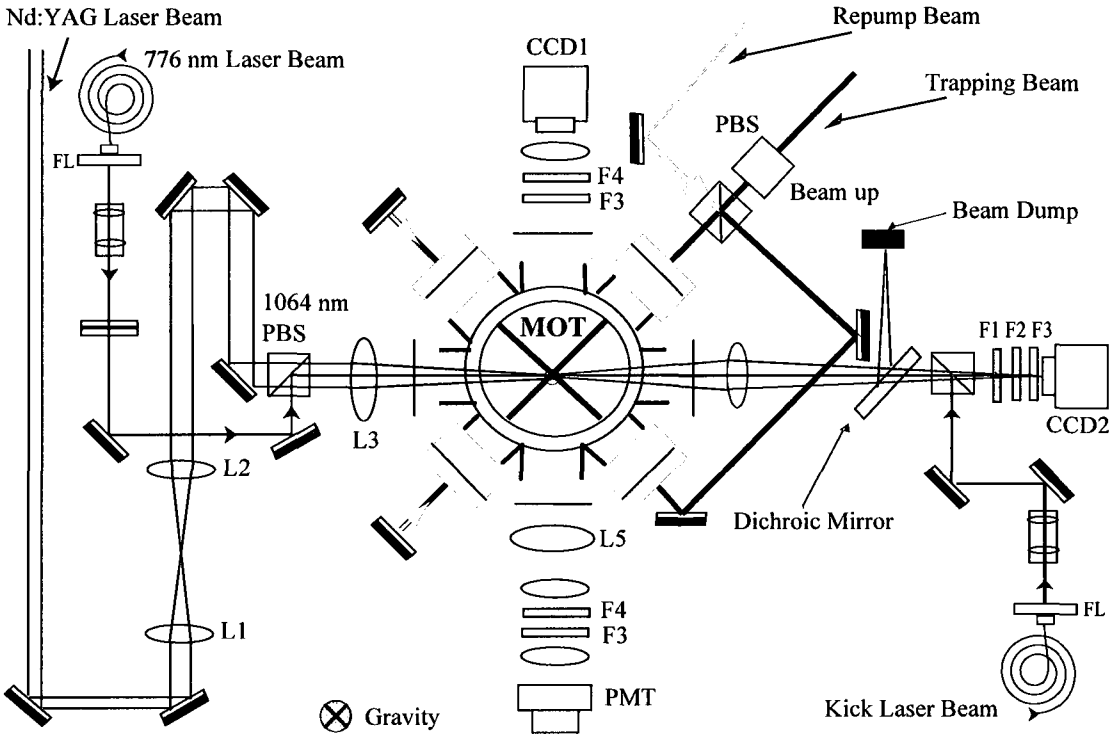

FIG. 17: The experimental setup for the cw and pulsed FORT. L1 = 100 mm and L2 = 200 mm. F1 = neutral density filter, F2 = colored glass filter, F3 = interference filter, and F4 = short pass filter. PBS = polarized beam splitter and PMT = photomultiplier.

(FORT) beam formed by the tightly focused Nd:YAG laser beam in preparation for loading the atoms into the FORT.

The FORT is then loaded according to the optimized protocols determined by Shiddiq [40]. Briefly, loading is achieved by turning on the YAG laser while changing the detuning of the MOT laser and the intensity of the repump laser. After the loading stage, the atoms are held in the FORT and we start our spectroscopic studies. As described later, several techniques are used to perform the spectroscopy, but all rely on determining the number of atoms remaining in the FORT after the spectroscopy beams are applied. Detection is always done by measuring the fluorescence of remaining FORT atoms with a photomultiplier tube. Fig. 17 shows the setup of the MOT and the FORT. The construction of the MOT and the FORT was done by the previous graduate student Dr. Minarni Shiddiq. The setup is well illustrated in her dissertation [40]. In this chapter, I will provide a summary of the apparatus and the data acquisition control with particular attention to modifications and additions which have supplemented our capabilities. These include addition of two independent spectroscopy lasers, one at 780 nm and the other at 776 nm.

III.2 VACUUM SYSTEM

The experiment is conducted in an Ultra High Vacuum (UHV) stainless steel chamber. First we evacuate the chamber from atmospheric pressure to a pressure of about 10^{-7} Torr with a turbo-molecular pump. The turbo pump is then removed from the system after closing a bakeable valve and we pump the chamber to lower pressure with an 11 liter/second ion pump which is continuously pumping the chamber, yielding an estimated pressure in the low 10^{-9} Torr region. The vacuum chamber is custom-built with ten 2-3/4″ conflat ports. Six of the ports are used for the MOT lasers, two for the FORT beam with co-linear spectroscopy beams, and two for detection. The source of Rb was an alkali dispenser from SAES Getters which is mounted directly in the vacuum chamber. During the experiment, the source current for the dispenser was typically set to 3 A.

III.3 TRAPPING LASER SYSTEM

The lasers that are used to form the MOT are Littman-Metcalf configuration External Cavity Diode Lasers (ECDL). A Piezo Electric Transducer (PZT) is attached to the

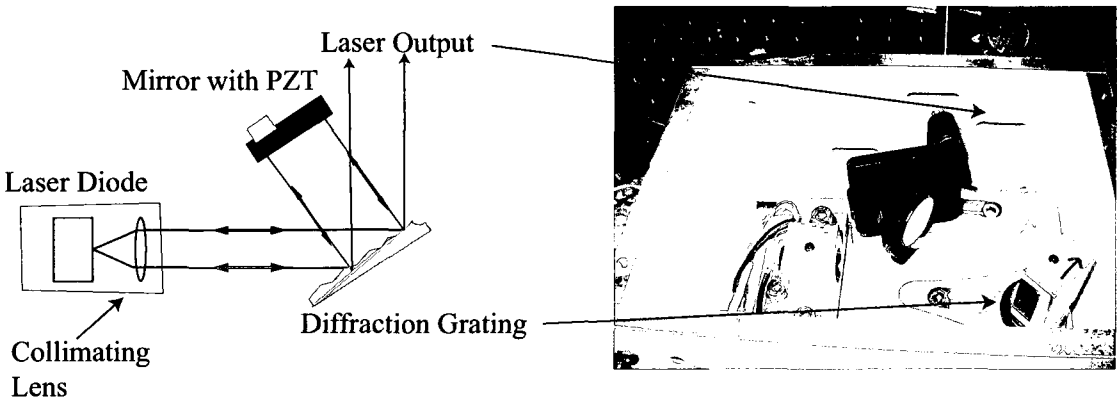

FIG. 18: The components of an ECDL in Littman–Metcalf configuration.

horizontal adjustment screw of the mirror mount in order to tune the laser frequency, as shown in Fig. 18. The temperature of the diode is stabilized using a Peltier cooler, sometimes referred to as a "thermoelectric cooler" (TEC). The laser diode and the collimating lens are enclosed within a collimating tube (Thorlabs LT230P-B), and mounted on a mounting block, its temperature is monitored using a thermistor. The TEC and the thermistor are connected to a feedback circuit of a homemade temperature controller. The diode injection current is controlled by a homemade current controller.

For long-term laser frequency stabilization, we use the saturation absorption technique, also known as Doppler-free Saturated Absorption Spectroscopy (SAS), along with a lock-in amplifier to lock the laser to a specific frequency. The setup for the saturated absorption spectroscopy is shown in Fig. 19 with the master-slave configuration used in our experiment.

The master-slave configuration enables us to obtain higher power trap laser beams than would be achieved from the ECDL alone. Both lasers are built using Sanyo DL 7140-201S diode lasers. We use Acousto-Optic Modulators (AOM) to detune the laser frequency and also for easy switching, a single pass AOM for the slave and a double pass AOM for the master is used in order to maintain coupling into the fiber with detuning the laser during the experimental runs [67]. The switching circuit is shown in Fig. 20. The power of the slave laser before going into a fiber launcher is $\sim$ 16 mW. A telescope with magnification 1$\times$ is set to collimate the beam going

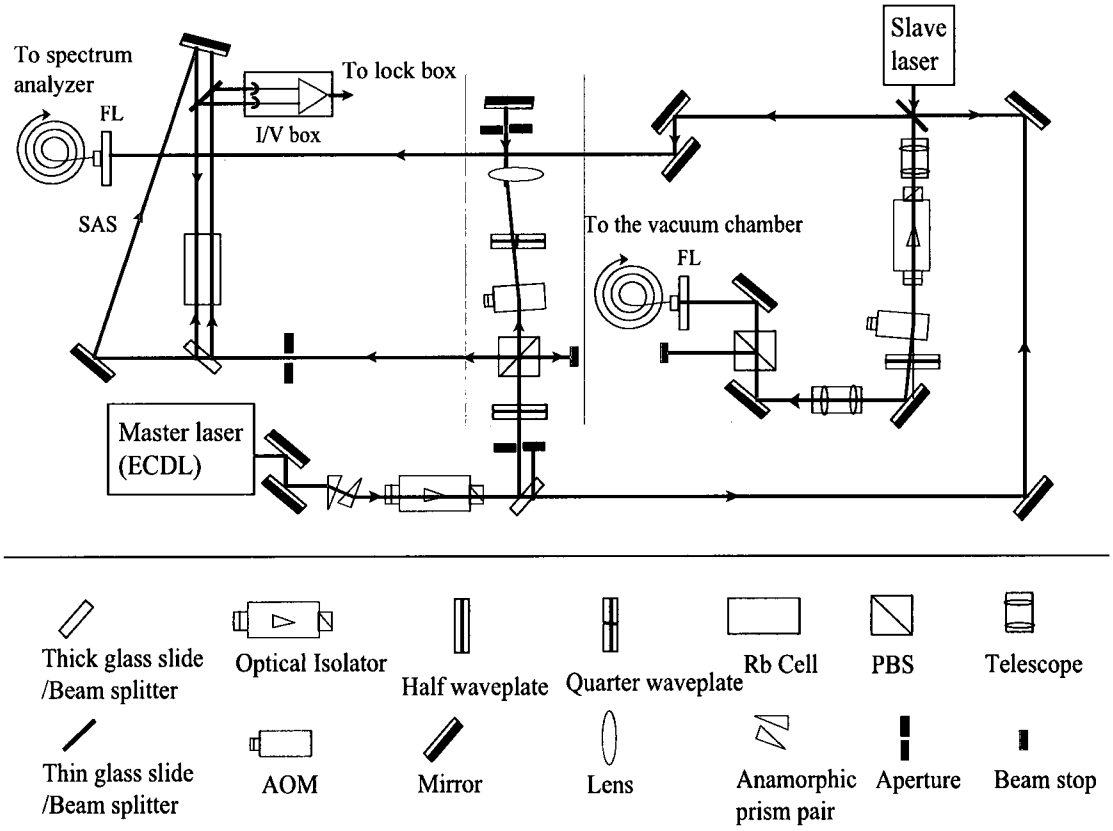

FIG. 19: The optical alignment of the master-slave laser system. Here FL = fiber launcher.

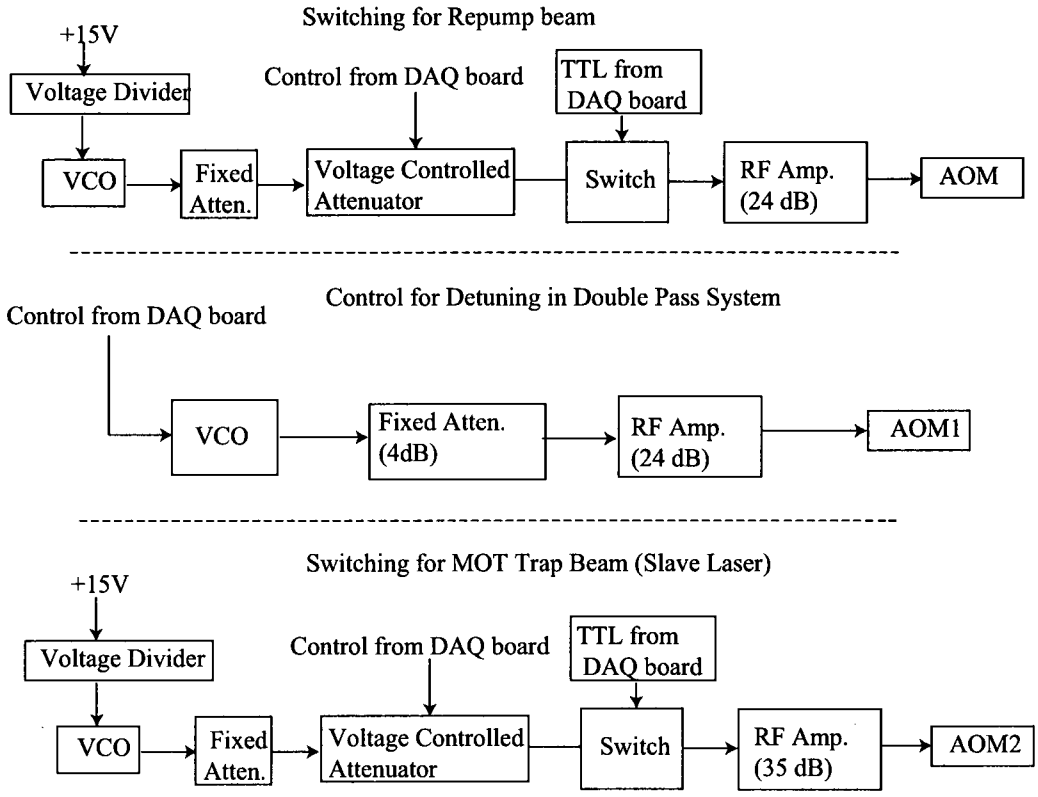

FIG. 20: Schematic diagrams of the AOM switching for the trap and repump laser beams, and the detuning system.

into the fiber cable launcher. Using a half wave plate and a polarized beam splitter cube before the fiber, we were able to stabilize the laser power after the fiber due to polarization changes. The coupling setup we used results in about 7-8 mW trap laser light going into the vacuum chamber. The MOT trap laser light is used to excite the atoms from the ground state $F = 3$ to excited state $F' = 4$ (^{85}Rb) or from the ground state $F = 2$ to excited state $F' = 3$ (^{87}Rb).

The repump laser is also an ECDL and built using a Sanyo DL 7140-201S diode laser. It is used to optically pump the atoms that fall to the ground state $F = 2$ (^{85}Rb) or $F = 1$ (^{87}Rb). The repump laser setup is shown in Fig. 21. The laser power output before entering the fiber launcher is ~ 2.5 mW, but after coupling into the fiber we get 1 mW to the chamber. The intensity of the repump laser beam going to the vacuum chamber is changed by adjusting the RF power going into the

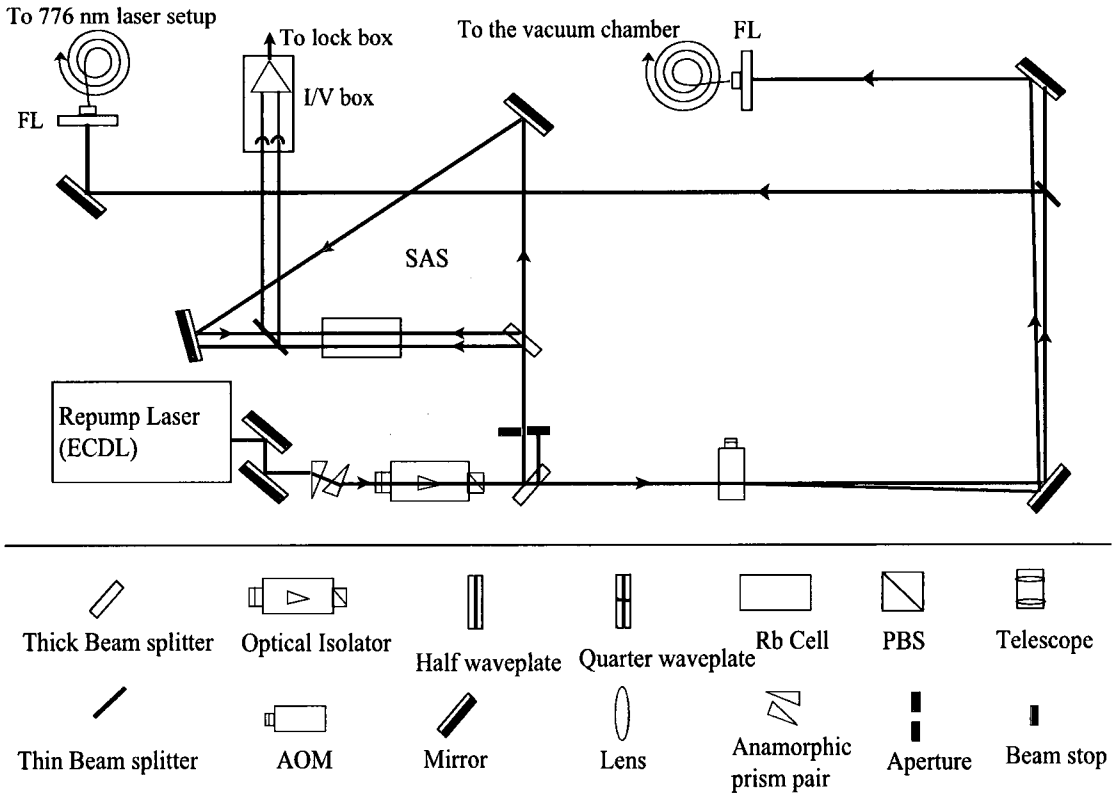

FIG. 21: The optical setup of the repump laser beam. Here FL = fiber launcher.

AOM, this is done using a voltage controlled attenuator as shown in Fig. 20. It has been shown previously that the FORT loading efficiency is strongly dependent on the repump laser intensity. As a result, fine control of the repump intensity is a critical component of the MOT to FORT transfer [40, 38].

We performed spectroscopy on both ^{85}Rb and ^{87}Rb. In each, a single isotope MOT was formed. Switching between the two isotopes was done by changing only the settings of the AOMs and recoupling into the fibers. Fig. 22 shows the saturation absorption spectra for locking the master and the hyperfine repump lasers for ^{85}Rb. The spectrum of the master laser has main peaks as a result of transitions from $F = 3$ to $F' = 2, 3, 4$ and crossover peaks $F = 3$ to $F' = (2, 3), (2, 4), (3, 4)$. These crossover peaks occur when two transitions share a common ground state, but different excited state. Since crossover peaks are often more intense than the normal transitions, we lock the trap laser at a crossover peak $F' = (2, 4)$ whose frequency ~ -92 MHz from $F' = 4$. The AOM inside the double pass system, which is set before the SAS, is

shifted -80 MHz, the result will be shifting the master laser $+160$ MHz then the AOM in the slave laser setup is shifted -80 MHz in order to get a total shift of $+80$ MHz and a detuning of $\Delta = -2\Gamma$ from $F = 3$ to $F' = 4$ transition. The hyperfine spectrum main peaks are transitions from $F = 2$ to $F' = 1, 2, 3$ and crossover peaks $F = 2$ to $F' = (1,2), (1,3), (2,3)$. The laser is locked at $F = 2$ to $F' = 1$ peak and it is shifted by $+92$ MHz using the AOM to be on resonance with the $F = 2$ to $F' = 3$ transition.

The saturation absorption spectra for locking the master and the hyperfine repump lasers for ^{87}Rb is shown in Fig. 23. The spectrum of the master has main peaks because of the transitions from $F = 2$ to $F' = 1, 2, 3$ and crossover peaks $F = 2$ to $F' = (1,2), (1,3), (2,3)$. The master laser is locked at $F' = (2,3)$ crossover peak whose frequency ~ -133.5 MHz from $F' = 3$. The AOM inside the double pass system is now at -93.3 MHz, the result will be shifting the master laser $+186.6$ MHz then the AOM in the slave laser setup is shifted -65 MHz in order to get a total shift of $+121.6$ MHz so now the detuning is $\Delta = -2\Gamma$ from $F = 2$ to $F' = 3$ transition. The hyperfine spectrum main peaks are transitions from $F = 1$ to $F' = 0, 1, 2$ and crossover peaks $F = 1$ to $F' = (0,1), (0,2), (1,2)$. The laser is locked at $F = 1$ to $F' = (1,2)$ crossover peak and it is shifted by $+78.6$ MHz using the AOM to be on resonance with the $F = 1$ to $F' = 2$ transition.

III.4 MOT SETUP AND PERFORMANCE

Fig. 24 shows the setup of the MOT. The setup is the familiar setup for most MOTs where a main beam is divided into three beams x, y, and z and then they are retro reflected. All beams are overlapped at the center of the chamber. The repump laser beam overlaps with the trap beams, though its alignment is far less critical. The intersection of the three trap beams at the center of the chamber is also where the zero of the anti-Helmholtz coil pair is located and this is where the trap forms. The Rb dispenser is mounted in the chamber and is operated at ~ 3 A. A pair of anti Helmholtz coils with 4.5 A current is mounted outside the chamber which give a magnetic field gradient of about 10 G/cm used to trap the atoms in the MOT. To get rid of any stray magnetic fields, especially due to the ion pump magnet, and to have the MOT at the center for easy overlapping of the MOT with the focused FORT laser beam, we set five shim coils around the chamber. Each shim coil is independently controlled with a separate power supply. Also two CCD cameras are

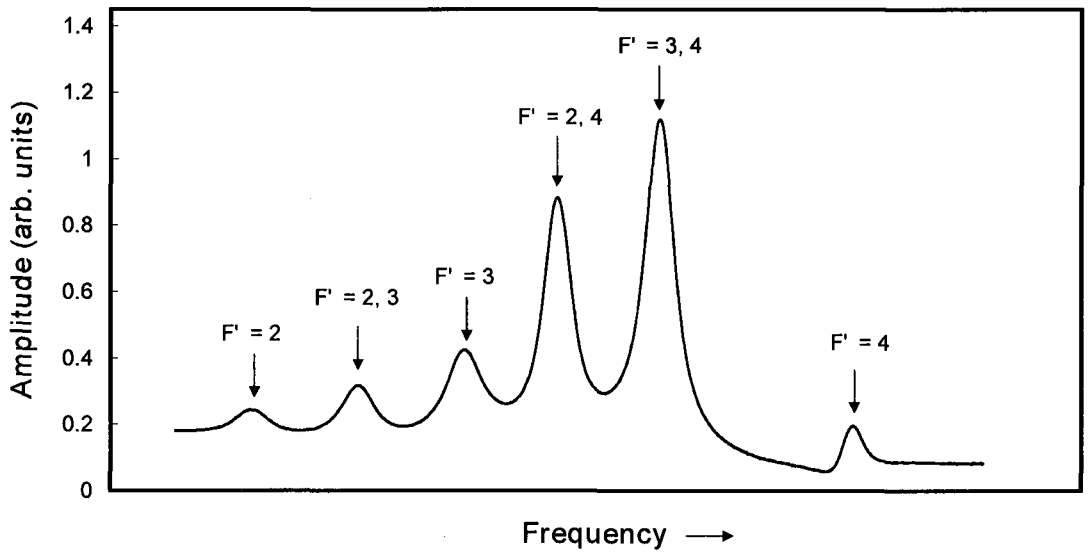

(a)

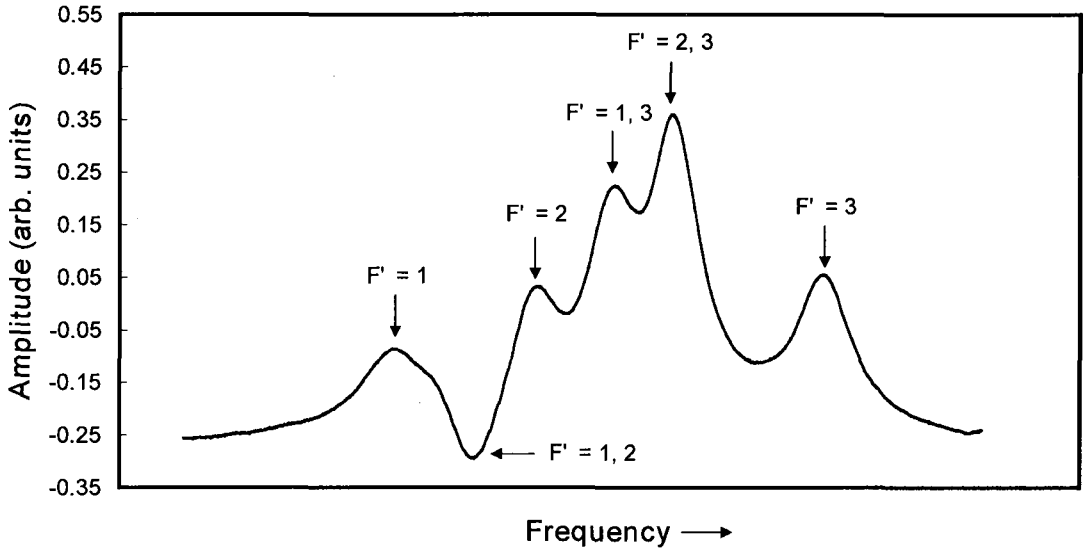

(b)

FIG. 22: The saturation absorption spectra for locking the master and the hyperfine repump lasers for ^{85}Rb. (a) For the master laser, the transitions are from $F = 3$ to F', and the laser is locked at crossover peak $F' = (2, 4)$. (b) For the hyperfine repump laser, the transitions are from $F = 2$ to F', and the laser is locked at $F' = 1$ peak.

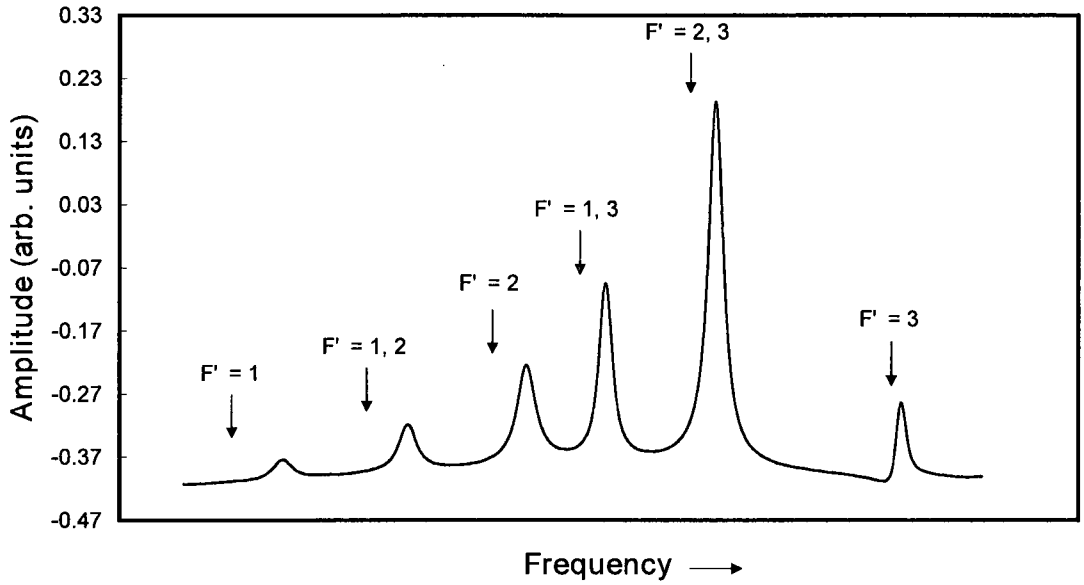

(a)

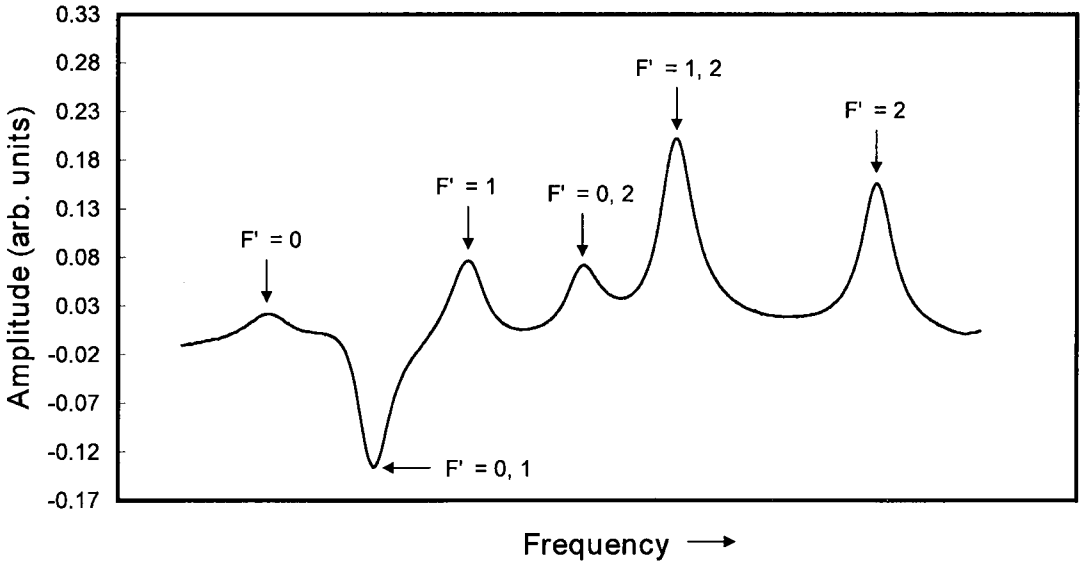

(b)

FIG. 23: The saturation absorption spectra for locking the master and the hyperfine repump lasers for ^{87}Rb. (a) For the master laser, the transitions are from $F = 2$ to F', and the laser is locked at crossover peak $F' = (2, 3)$. (b) For the hyperfine repump laser, the transitions are from $F = 1$ to F', and the laser is locked at crossover peak $F' = (1, 2)$.

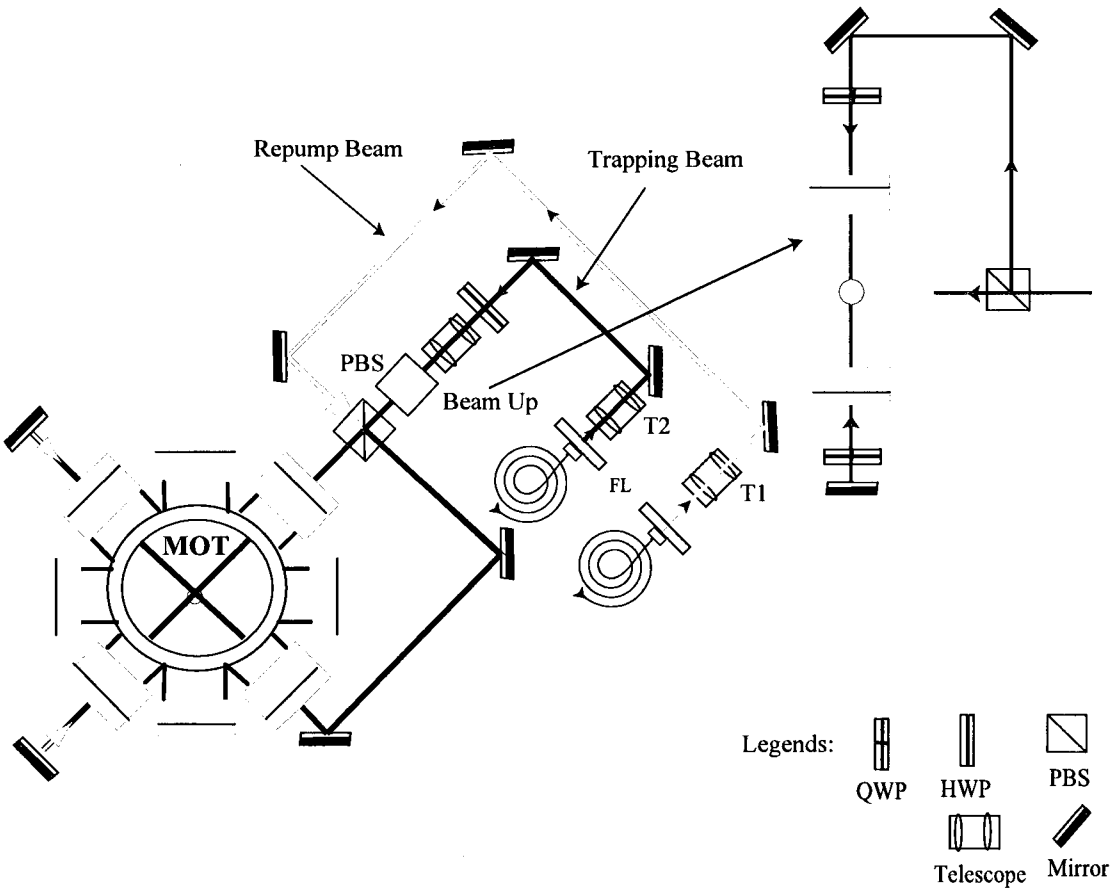

FIG. 24: The optical setup of the MOT laser beams. Here FL is fiber launcher, T2 is a beam collimator, and T1 and T3 are beam expanders. QWP is a quarter waveplate and HWP is a half waveplate.

used to monitor the MOT image from two different directions. The MOT position can be adjusted by varying the current for each shim coil. One important aspect of the detection of the FORT atoms is to have the forces from the MOT beams "balanced". While collection of the cold atoms in the MOT itself is not so sensitive to an imbalance in the forces coming from the individual MOT beams, an imbalance during the detection phase will blow away the atoms quickly making a fluorescence measurement difficult. In order to achieve the needed balance, we adjust the shim coils while switching on and off only the current to the anti-Helmholtz coils. This is done while simultaneously looking at the MOT image on a TV monitor or observing the MOT signal from the photomultiplier tube (PMT) on an oscilloscope. If the imbalance in the forces is sufficiently nulled, the atoms (now in an optical molasses only) will disperse slowly (in about 1 second). On the other hand, if the balance is not set properly, the atoms are pushed to one side in milliseconds. With everything optimized, our MOT system typically loads about 1.5×10^7 Rb atoms.

III.5 ND:YAG LASER SYSTEM

The FORT laser used in our experiment is a Spectra-Physics Model 3800 Nd:YAG Laser, operated either in continuous-wave (cw) or mode-locked (pulsed), at 1064 nm wavelength. The average power for cw mode is 11 Watts while for mode-locked beam is 10 Watts. Laser safety precautions have to be taken while working with the laser since it is class IV-high power. Safety goggles as well as warning signs are used. The laser system consists of four parts [68], the first is the power supply which controls everything in the laser system; shutters, water cooling flow, current to the krypton lamp in the laser head, and electrical connections to the laser head. The power supply front and rear panels are shown in Fig. 25. The second is the laser head shown in Fig. 26 which consists of the laser/optical cavity; Nd:YAG Rod with krypton arc lamp (lasing unit), high reflector, output coupler, pinhole, shutter and polarizer. The third is the mode locker system which consists of mode locker modulator, mode locker driver, and stabilizer. The last part is the switching system which consists of an acousto-optic modulator (AOM) and Model 3275 acousto-optic stabilizer/Q-switch for driving and controlling the AOM frequency.

During the experimental runs, the Nd:YAG beam needs to be switched on or off at certain times. While the laser is equipped with an AOM, it is intended for Q-switching or intensity stabilization and is therefore not a particularly efficient device.

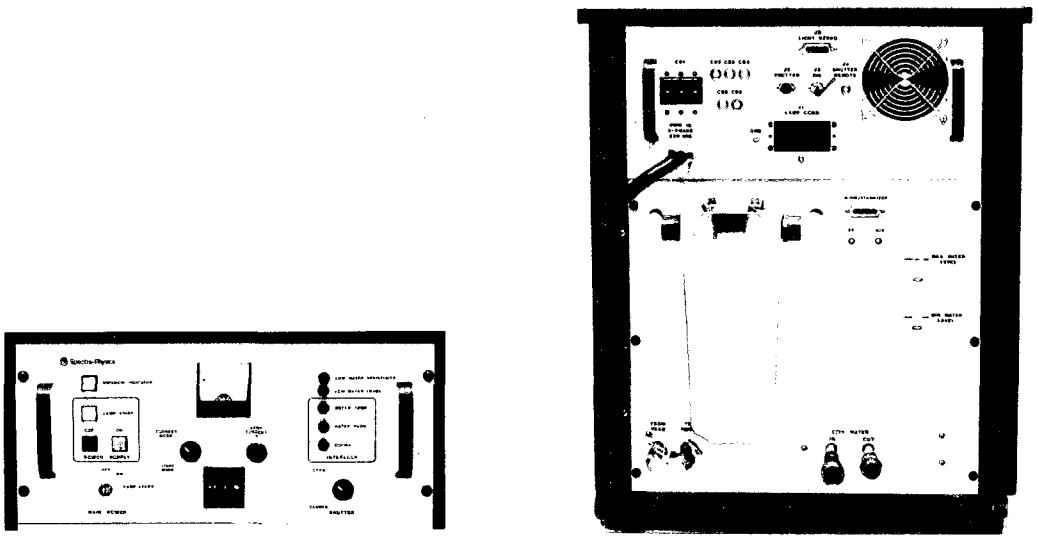

(a) Front Panel. (b) Rear Panel.

FIG. 25: The power supply panels of the Spectra Physics Nd:YAG laser system Model 3800.

Since we wanted as much usable power as possible to be available for the trap, we installed a high efficiency Intra-Action AOM. Our replacement AOM operated at the same 27 MHz as the original AOM and so the original AOM driver (with minor modification for computer control of switching) was used. This AOM gives a first order maximum power of 8.7 Watts in cw mode while running at 29 A lamp current. For mode-locked operation, the maximum power reached is 7 Watts at the same lamp current. Fig. 27 shows the optical setup of the Nd:YAG laser beam going into the chamber. The beam size coming out of the laser is about 1 mm, a beam expander which consists of 100 mm and 200 mm lenses is used to increase the size of the beam to a $1/e^2$ intensity radius of 4.2 mm and collimate it before going into the chamber. An anti-reflected coated achromatic lens (Thorlabs LAC506-B) with focal length 200 mm mounted in an XYZ stage is used to focus the beam to the center of the chamber with a calculated waist of 16 μm. A 100 mm lens is used on the opposite side of the chamber to collect the divergent beam and to image the MOT cloud and a dark spot to the CCD2 camera. The dark spot (shown in Fig. 28) arises because

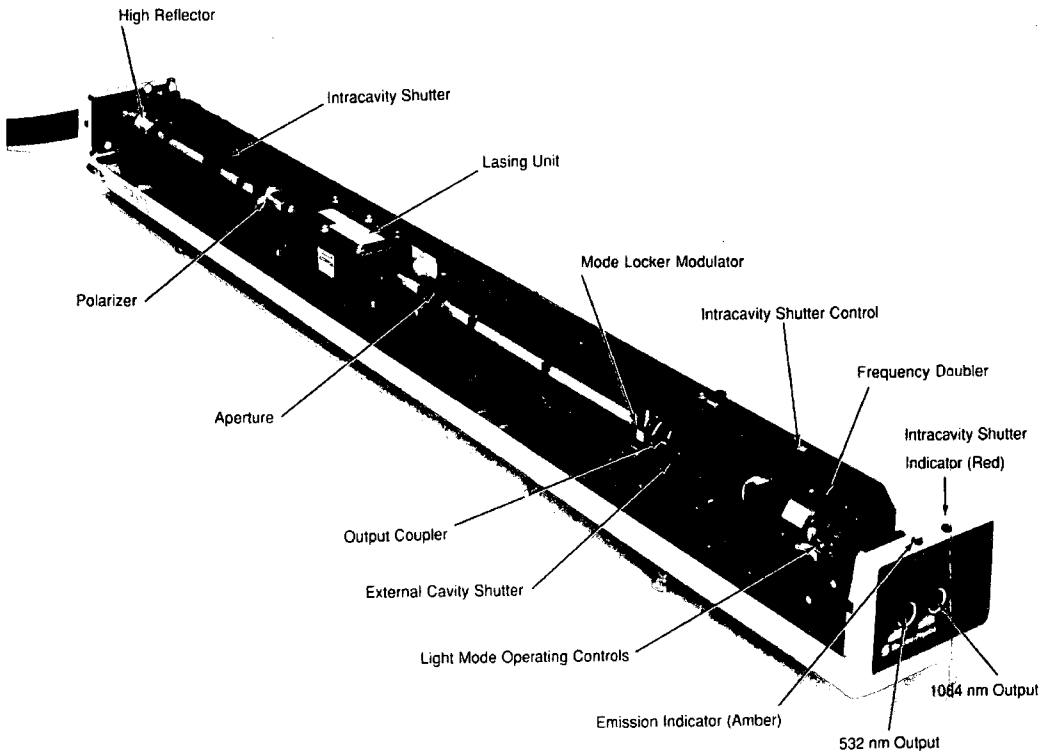

FIG. 26: Parts of the Spectra Physics Nd:YAG Laser Head Model 3800.

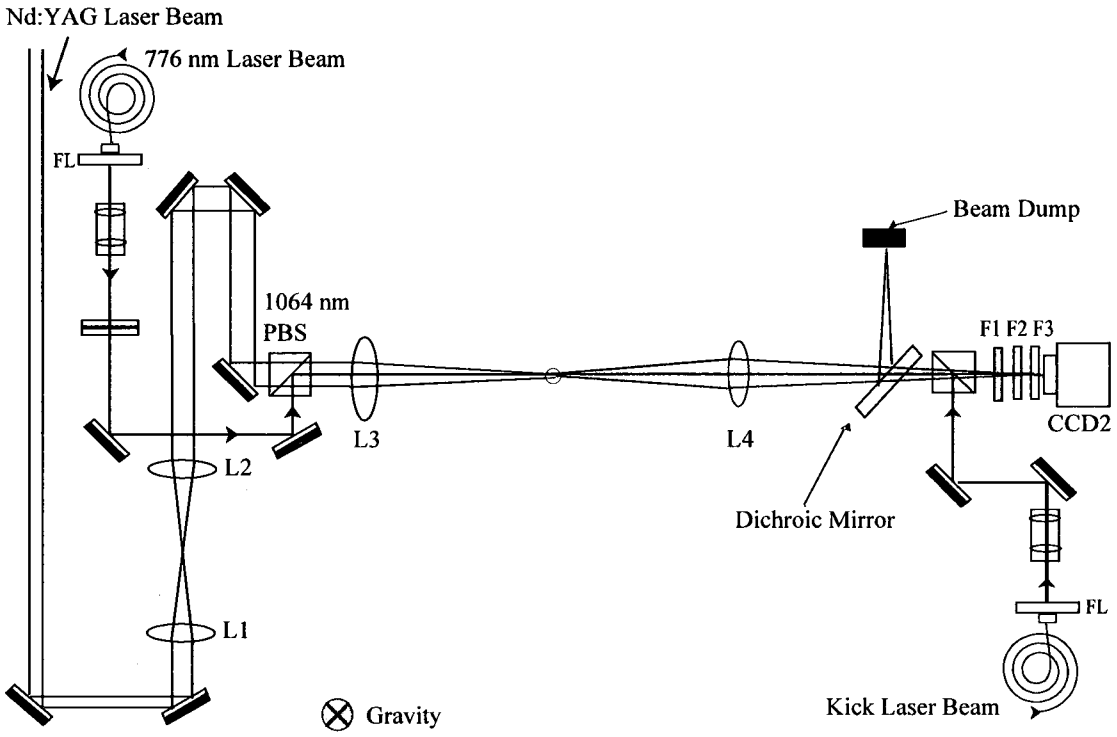

FIG. 27: The experiment setup for sending the FORT, kick, and 776 nm beams to the vacuum chamber.

the ultracold atoms at the focus of the Nd:YAG beam are AC Stark shifted out of resonance with the MOT light, therefore they do not scatter any photons from the MOT light and they look dark on the monitor. We use a dichroic mirror (CVI Model SWP RS1064/TU780) to reflect the 1064 nm Nd:YAG beam to the beam dump and to let through the 780 nm light to the CCD2 camera.

III.6 KICK LASER SYSTEM

As discussed in the next chapter, we have used several techniques to perform spectroscopy of atoms confined in the FORT. One such technique is to overlap a traveling wave spectroscopy laser with the FORT atoms and scan the laser. When the laser is resonant with atoms in the FORT, it will scatter photons. If it is not resonant, it will not. If a sufficient number of photons are scattered, the atom will be heated to an extent where it can longer be trapped, i.e. it is "kicked" out of the trap. When we use a laser in this way, we refer to it as the "kick beam". By determining the number

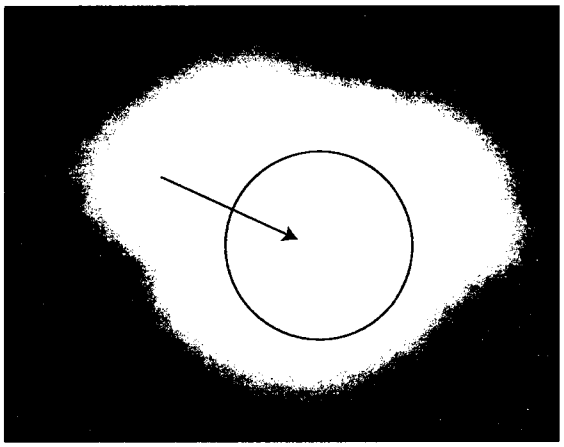

FIG. 28: The dark spot at the center of the MOT cloud indicates the focus of the FORT (Nd:YAG) laser.

of atoms kicked out of the trap when the kick beam frequency is scanned, we can determine the spectra of the confined atoms.

For each frequency where data is taken, the kick laser is locked to a reference cavity (details of reference cavity lock will be given later). This enables us to scan the laser over an extended frequency range, while keeping the frequency stabilized for each data point. In order to monitor the laser frequency when taking data and ensure that it was indeed stable, we had to use one of our MOT lasers as a reference. The master laser was a good choice because it is locked to one of the peaks of the trap saturation absorption signal and also it had a free beam that we could use. The master beam was sent by a fiber optic to overlap with the kick laser beam before going into a Fabry-Perot optical spectrum analyzer. The two lasers were sent to the same spectrum analyzer whose output was sent to a digital scope. A Thorlabs spectrum analyzer with 1.5 GHz Free-Spectral Range (FSR) was used; it was convenient to use one with relatively small FSR to be able to monitor the kick laser detuning by increments on the order of few MHz.

Before implementing the reference cavity lock, we used another technique to lock and scan the kick laser. A coil carrying current was added around the rubidium vapor cell in the saturation absorption setup. By placing the cell in the center of the coil, it will be exposed to a homogeneous magnetic field along its length, resulting in a Zeeman shift to the atomic energy levels. Since a magnetic field splits the

hyperfine levels according to their magnetic quantum numbers m_F, the absorption of a left or right circularly polarized photon by an atom in a magnetic field that is along the photon's propagation direction depends on whether the resonant transition in the atom has the corresponding change in the magnetic quantum number. Two quarter wave plates were used in the saturation absorption setup and they were set such that the pump and the probe beams interact with the same levels. First with zero field, we lock the laser (using a lock-in amplifier) to one of the peaks of the saturation absorption signal. Then we change the current of the coil while monitoring the frequency shift of the laser on the scope. This method only gave us about 70 MHz range of detuning which is not enough to scan over all the different hyperfine transitions. Fig. 29 shows the saturation absorption signal for different magnetic field values.

III.6.1 Reference Cavity

In order to perform our spectroscopic studies on the atoms in the FORT, we needed to scan the kick laser over a few hundreds MHz range and at the same time to record the frequency detuning for each data point taken. Locking the laser to a reference cavity enabled us to achieve that. The reference cavity is a Fabry-Perot interferometer that was originally used for frequency stabilization of a cw dye laser (Coherent 699).

Fig. 30 shows the setup of the reference cavity. A small portion of the laser beam that will be used for the experiment is sent to the reference cavity setup using a beam splitter (BS1). At BS2 the reflected beam goes to the reference cavity where the intensity of the output beam is monitored by a photodiode (PD1) and the transmitted beam goes to PD2 which acts as a reference.

The signals from the photodiodes are sent to separate I-to-V (current-to-voltage) converters. After balancing the two photodiodes, we used an electronic circuit to divide the intensity of PD1 by that of PD2. This was done to get rid of any laser intensity changes that are caused by any effect other than the reference cavity. The division circuit is made using Analog Devices (AD734) 10 MHz, 4-Quadrant Multiplier/Divider. The circuit also has an input that can be used as a dc offset which allows one to null the background signal. The output is sent to an integrator box before it goes to the laser lock box as the error signal that can be used to lock the laser frequency. The laser source is an external cavity diode laser whose frequency can be swept through atomic absorption lines by varying the voltage across a PZT

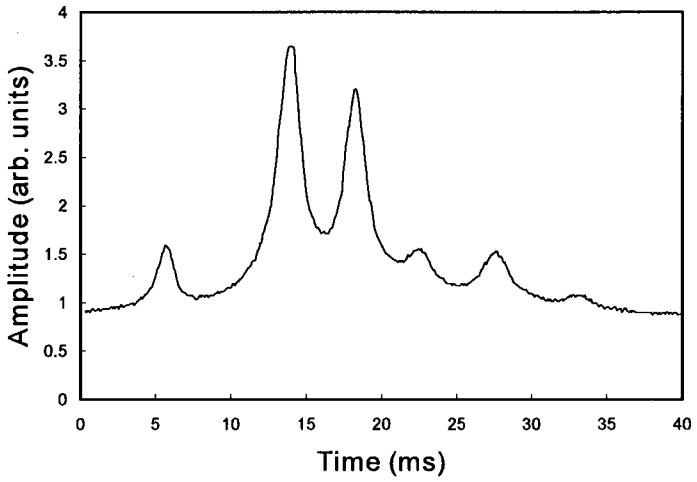

(a) 0 G.

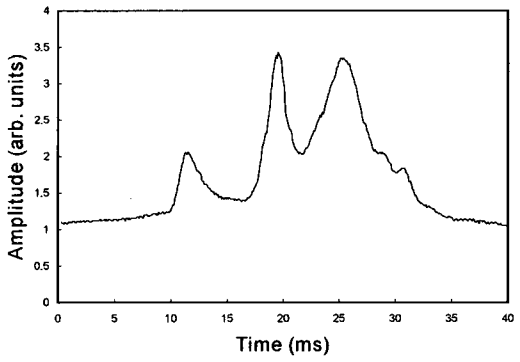

(b) 25 G.

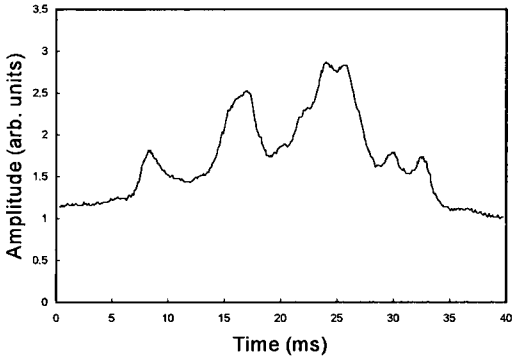

(c) 50 G.

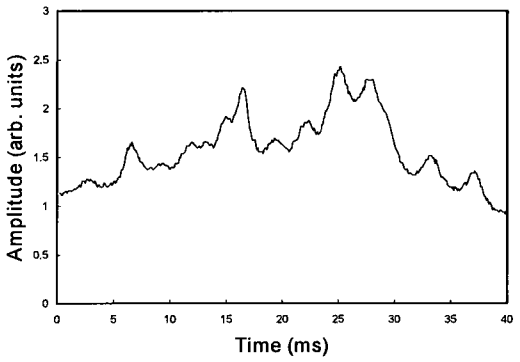

(d) 75 G.

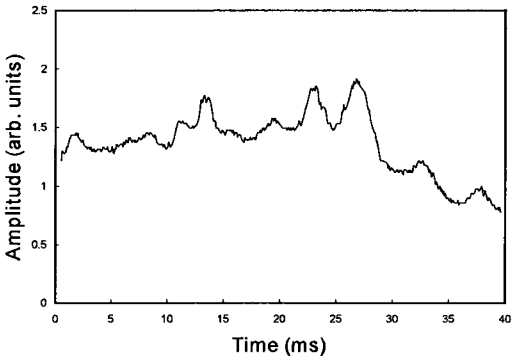

(e) 100 G.

FIG. 29: Kick laser saturation absorption signal for different magnetic field values.

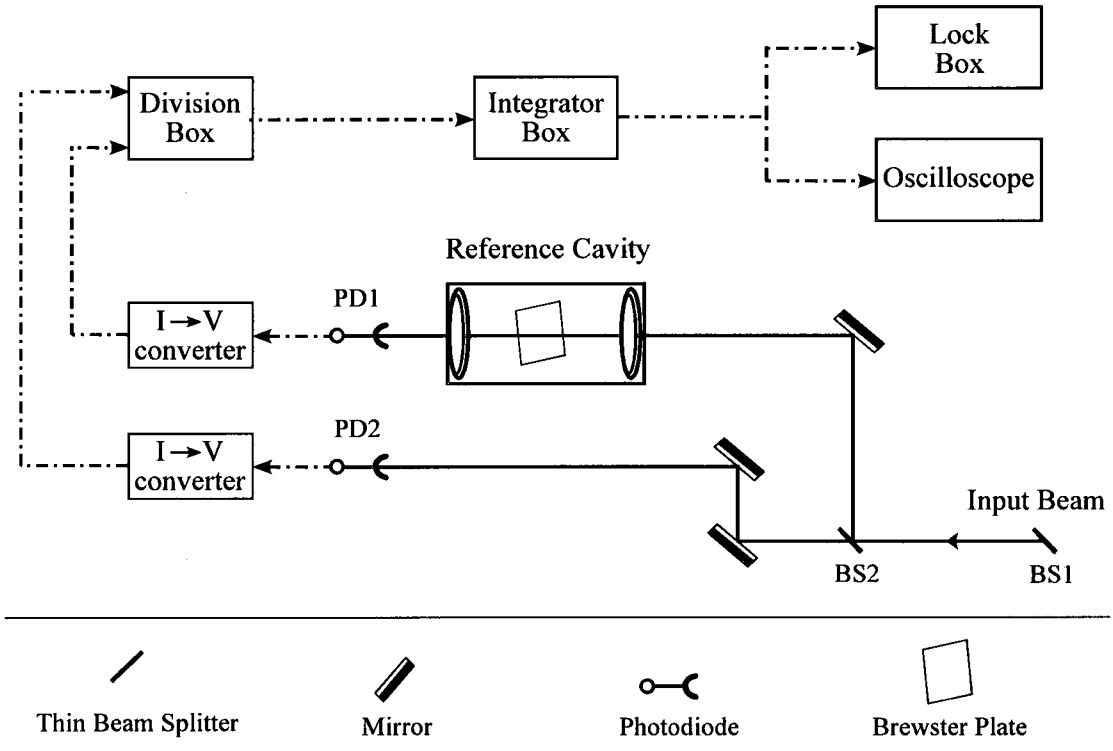

FIG. 30: Reference cavity setup and electronics used to lock the kick laser frequency.

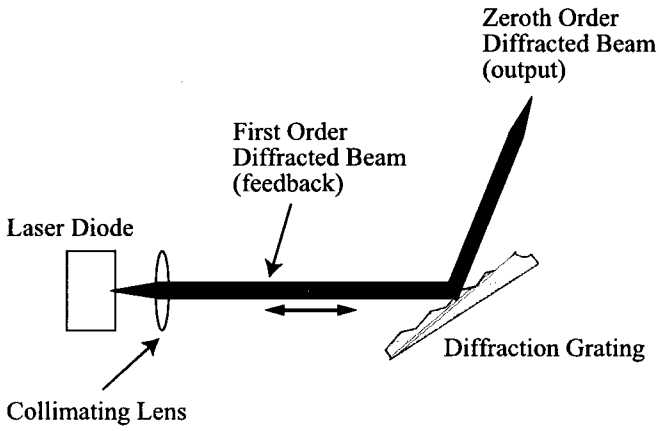

FIG. 31: Littrow configuration.

which changes the laser cavity's resonant frequency. An optical isolator is often used to prevent unwanted reflected light from going back into the laser system.

III.6.2 Kick Laser setup

The kick laser is an ECDL built using a Sanyo DL 7140-201S diode laser in a modified version of Littrow configuration [69]. In the popular Littrow configuration, shown in Fig. 31, the grating is aligned such that the first order diffraction from the grating is coupled directly back into the laser while the zeroth-order diffraction is reflected as the output beam. The lasing wavelength is dependent on the angle of the incident laser beam with respect to the grating. By changing the angle of incidence, precise wavelength tuning can be achieved. The Littrow configuration has the problem of beam angular displacement as the grating angle is adjusted. In the new version shown in Fig. 32, the main modification made to ensure a fixed direction of the output beam is the addition of a single plane mirror parallel to the diffraction grating and located rigidly with respect to it. The laser beam reflects from the grating and then from the mirror. When the grating is rotated by $\Delta\theta$, the beam reflected by the grating is rotated by twice that angle, or $2\Delta\theta$. Since the mirror rotates by the same angle as the grating, when the reflected beam from the grating hits the mirror, it is again reflected back by $2\Delta\theta$, such that the output beam experiences no angular deviation and just a negligible linear translation.

As with all of our diode laser systems, the kick laser system is enclosed by an

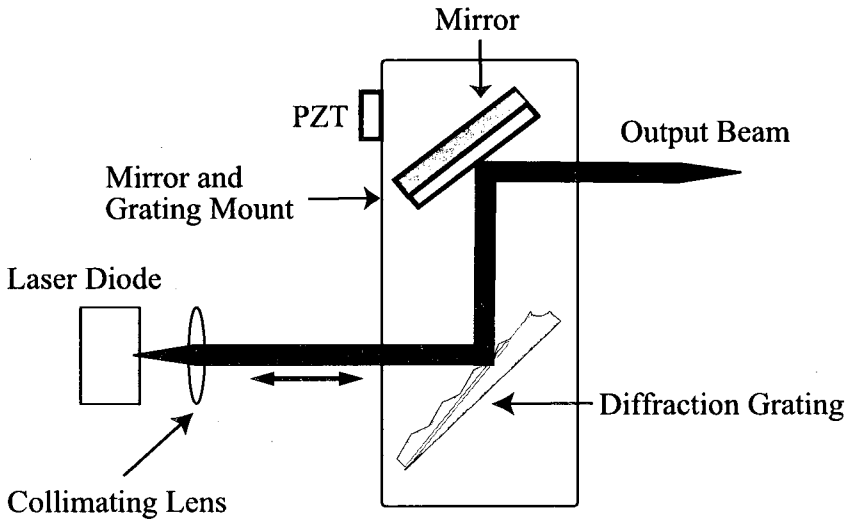

FIG. 32: Modified Littrow configuration.

aluminum box to reduce the air movement and sensitivity to frequent temperature changes in the lab. This box has openings for laser beam output and for adjusting the cavity length. Also, the temperature of the diode is stabilized using a TEC. The laser diode and the collimating lens are enclosed within a collimating tube (Thorlabs LT230P-B), and mounted on a mounting block. This block is mounted on another aluminum block such that the TEC can be placed between the two blocks. Its temperature is monitored using a thermistor that is inserted into a small hole near the TEC. Again as with the MOT lasers, the TEC and the thermistor are connected to a feedback circuit of a homemade temperature controller and the diode injection current is controlled by a homemade current controller.

The kick laser setup is shown in Fig. 33. As mentioned before, the laser is locked to a reference cavity but since we need to scan the laser around the different possible hyperfine transitions, we use saturation absorption spectroscopy as our reference to ensure that the laser is close to resonance. An AOM was used to enable the switching of the laser which is only turned on for a very short time (few ms) at the end of the FORT holding stage. The diffracted first order was coupled to a fiber optic and sent to the chamber. To avoid power broadening of the spectroscopy results, very little kick power was used $\sim$10 μW. We encountered two problems in maintaining that small power during that short time. The first was due to thermal effects in the

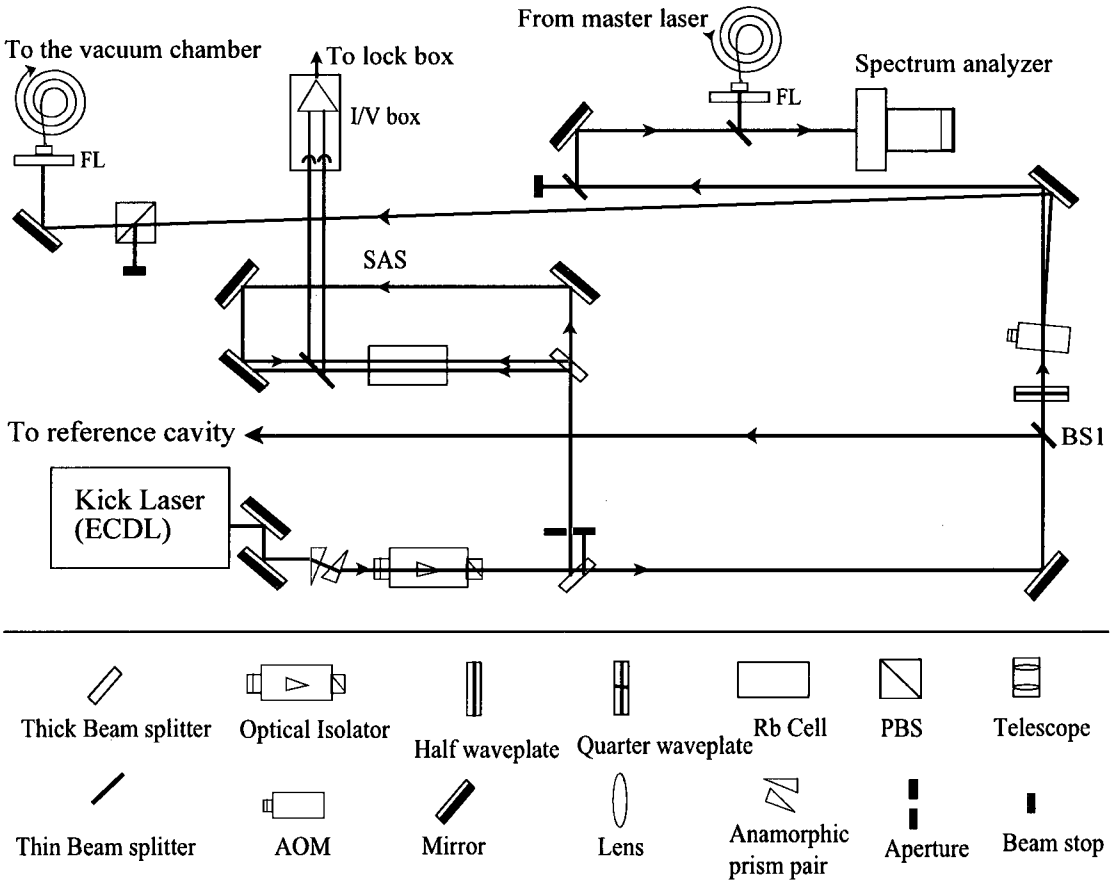

FIG. 33: The optical setup of the kick laser beam. Here FL = fiber launcher.

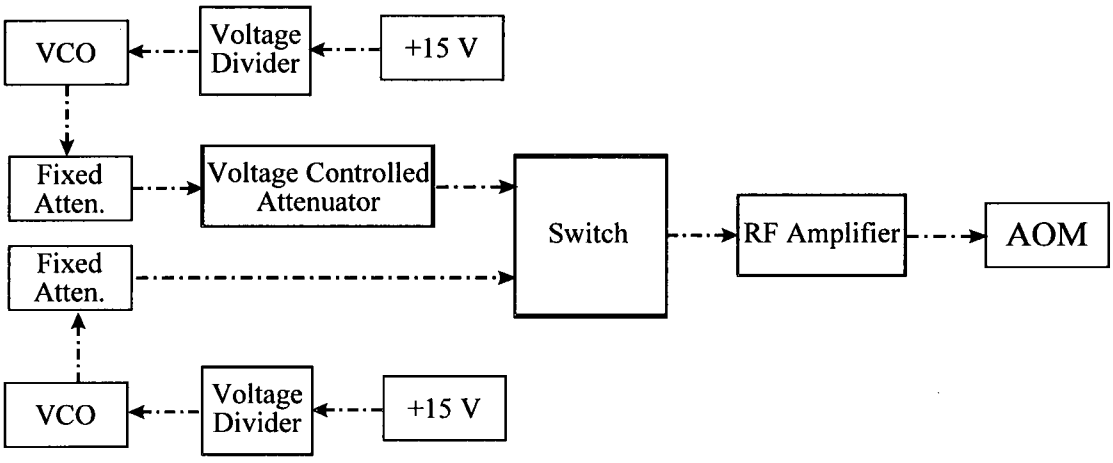

FIG. 34: Schematic diagram of the AOM switching for the kick laser beam.

AOM. We found that every time we switch the laser AOM on, the power output from the fiber does not reach the value it was set at until after a few ms. To overcome this problem, two Mini-Circuits ZOS-100 voltage controlled oscillators (VCO) set at two different but close frequencies were used in the switching circuit of the AOM, shown in Fig. 34. The AOM now switches between these two frequencies instead of switching on and off. One of the VCOs is set at 92 MHz and is used in the experiment, the other VCO is set at 77 MHz. Now the rf power being sent to the AOM does not vary and thermal effects are minimized. When the AOM is set to the "off" frequency, it is not phase matched for this second frequency, and little light is diffracted. Any light which may be diffracted, in any case, will come at a different diffraction angle from the "on" frequency and will not be coupled into the optical fiber. Another problem we noted was the change of the light polarization after the fiber when using the AOM to switch the laser on and off. Although the source of this polarization was not well understood, we found that use of a half wave plate and a polarized beam splitter cube before the fiber launcher fixed the problem.

Fig. 27 shows the setup for sending the kick beam into the chamber. Since we did not have any more free windows on the vacuum system, we used the Nd:YAG laser exit port which is also used to monitor the MOT image on CCD2. A polarized beam cube was placed between the dichroic mirror and the camera to change the beam direction by 90° to be sent to the chamber without blocking the camera. Overlapping the kick beam with the FORT is done by first overlapping it with the MOT. The

laser is locked at the trap transition and is sent into the chamber while the MOT signal from the PMT is monitored on the digital scope. The beam is then spatially adjusted. Once it hits the MOT it will cause some trap loss. Then the beam position is adjusted for maximum loss. For optimum overlap, the kick beam power was then reduced slightly and the position readjusted.

III.7 776 NM LASER SYSTEM

As we discuss in the next chapter, one of the obstacles in achieving precision spectroscopy is inhomogeneous broadening due to the different polarizabilities of the lower and upper energy levels of the transition being studied. One of the experiments we performed was an attempt to reduce this broadening by application of an additional laser frequency to tailor the polarizability of the upper level [59]. In the FORT the energy levels of the atoms experience an AC Stark shift which depends on the intensity of the laser light and the polarizability of the atomic level. For a two-level atom, the shift is opposite for a pair of states. The result is a shift in the resonance frequency and inhomogeneous broadening of the transition. As discussed in Sec. II.7, if another laser with the right intensity and detuning from the $5P_{3/2} \rightarrow 5D_{5/2}$ transition is present with the Nd:YAG laser during the FORT holding time, the AC Stark shift of the two low-lying states $5S_{1/2}$ and $5P_{3/2}$ will be the same. For such a situation, we would expect a decrease in the linewidth in our spectra.

In order to investigate this effect, an external cavity diode laser was built and set at 776 nm to drive the $5P_{3/2} \rightarrow 5D_{5/2}$ transition. Using this transition as a reference, we could then adjust the detuning using an acousto-optic modulator and apply this light to the trap while taking spectra on the $5P_{3/2} \rightarrow 5D_{5/2}$ transition.

This laser was also used in a related experiment to investigate the atoms in the FORT by also performing actual spectroscopy of the $5P_{3/2} \rightarrow 5D_{5/2}$ transition. Here, two lasers were needed for this two-photon spectroscopy, one at 780 nm to drive the $5S_{1/2} \rightarrow 5P_{3/2}$ transition and one at 776 nm to drive the $5P_{3/2} \rightarrow 5D_{5/2}$ transition. The MOT beams were used as the 780 nm light for the first step transition from $F = 3$ ground state to $F' = 4$ first excited state (^{85}Rb) or from $F = 2$ ground state to $F' = 3$ first excited state (^{87}Rb). For the second step transition, the 776 nm laser was used to stimulate all possible transitions from the intermediate excited state to the higher excited state $5D_{5/2}$. By scanning the frequency of the 776 nm laser and with the 780 nm laser frequency fixed, the two-photon transition spectra can

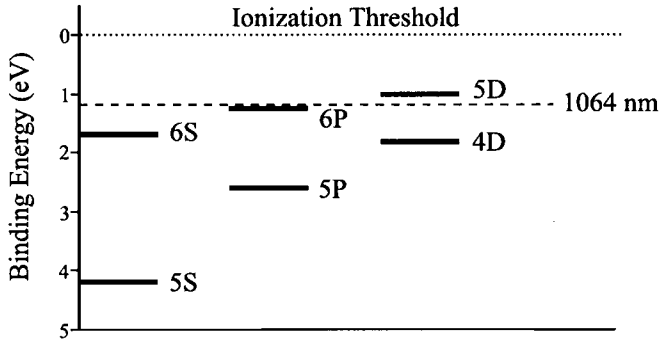

FIG. 35: Rubidium ionization threshold. The dashed line marks the binding energy which can be ionized by the Nd:YAG laser.

be detected. Before taking spectra in the FORT, we performed spectroscopy in the MOT. Our data was in agreement with other group's work [70]. We then switched to the FORT. While essentially the same experiment was done in both the MOT and the FORT, different detection methods were used for each case. For the MOT, we measured the absorption of a modulated 776 nm laser with a photodiode and a lock-in amplifier. It required the MOT to be present and stable for few seconds as we found the need to average over tens of scans to get a good signal to noise ratio. This is hard to do in the FORT since the number of atoms trapped will start to decrease after few hundreds of milliseconds because of two-body and background gas collisions as well as scattering of probe laser photons. Another method was used that depends on the fact that the presence of the 776 nm laser and the Nd:YAG laser at the same time with the MOT light can cause photo-ionization of the atoms in the dipole trap [71] as shown in Fig. 35. Detection methods used for both the MOT and the FORT will be discussed in more details in the next chapter.

III.7.1 Blue Signal and Doppler free spectroscopy

Early experiments [72] have demonstrated that the $5S_{1/2} \rightarrow 5P_{3/2} \rightarrow 5D_{3/2,5/2}$ two-photon transitions in Rb can be efficiently excited with a single diode laser at 778 nm, on the other hand, using two lasers to excite the two-photon transition can improve the signal obtained [73, 74]. As mentioned before the MOT beams were used to drive the first transition while another laser was built to drive the second transition. For Rb atoms, after excitation to the $5D_{5/2}$ state by absorbing photons

at 780 nm and 776 nm, decay with a 35% probability to the intermediate $6P_{3/2}$ state and then with a 31% probability to the ground state [75] takes place, emitting blue photons at 420 nm. These photons were used to form a blue signal that can be used as a reference to lock the laser near the $5P_{3/2} \rightarrow 5D_{5/2}$ transition. To obtain that signal, a Rb cell was used in the laser setup where a 776 nm beam is overlapped with and counter-propagating to a 780 nm beam. Using two counter-propagating beams allows all portions of the velocity distribution to contribute to the signal since the two wavelengths are so close. This 780 nm beam was the zeroth order of the repump laser AOM which was locked at $F = 2$ to $F' = 1$ transition peak for ^{85}Rb and at $F = 1$ to $F' = (1, 2)$ crossover peak for ^{87}Rb. The resulting blue signal for each isotope is shown in Fig. 36. A photomultiplier tube with a 420 nm filter was placed on top of the Rb cell to detect the blue signal which goes to an I-to-V converter before it acts as the input signal to a lock-in amplifier.

III.7.2 Laser Setup

Fig. 37 shows the setup of the 776 nm laser. An ECDL in Littman-Metcalf configuration using a Sanyo DL 7140-201S diode laser was built. A portion of the laser output is going to the first AOM which is used for switching the laser on and off, the first order was picked off by a fiber optic and sent to the chamber. The rest goes to another AOM which was double-passed to provide even more frequency detuning. The output from the double-passed AOM was sent to the Rb cell where it overlaps with the 780 nm beam to obtain the blue signal. Note that the laser setup for the inhomogeneous broadening experiment and for two-photon spectroscopy experiment was mainly the same, the main difference being settings of the AOMs which will be given in the next chapter.

Sending the 776 nm beam into the chamber was achieved by using a polarized beam splitter cube and a half waveplate to couple it with the Nd:YAG laser beam. The polarized beam cube used (PBS 05BC16) was made for 1064 nm wavelength to minimize the loss of the Nd:YAG power. The setup to send the beam into the chamber is shown in Fig. 27. Overlapping the 776 nm beam with the FORT was quite a challenge. For preliminary alignment with the MOT, the kick beam (780 nm) was used. With the same setup shown in Fig. 27, the kick beam was sent into the chamber instead of the 776 nm beam. So now we can monitor the MOT loss while moving the beam around. Following the same technique described in the

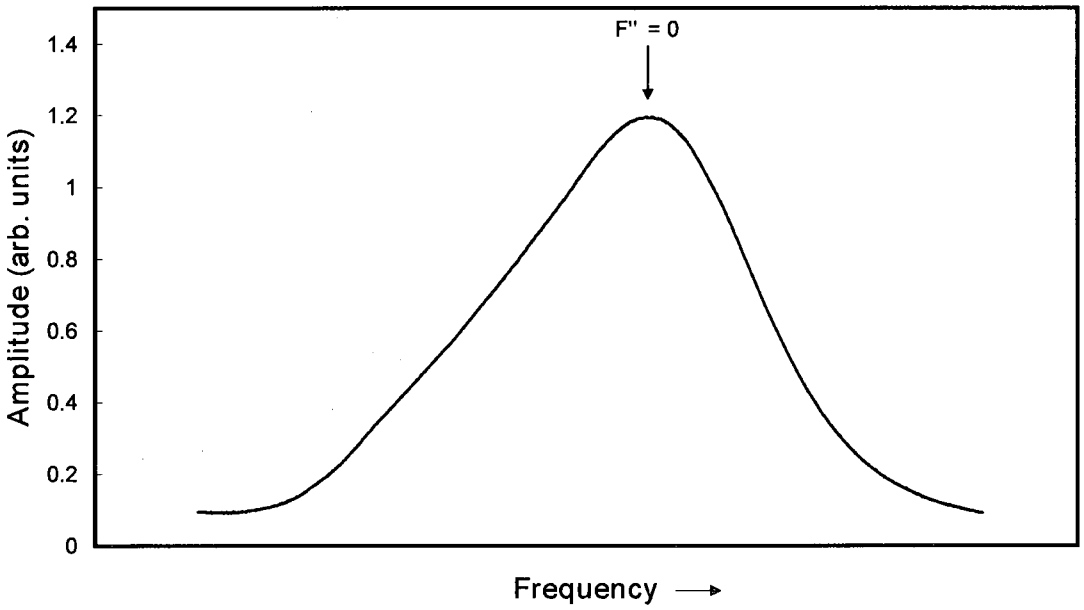

(a) ^{85}Rb

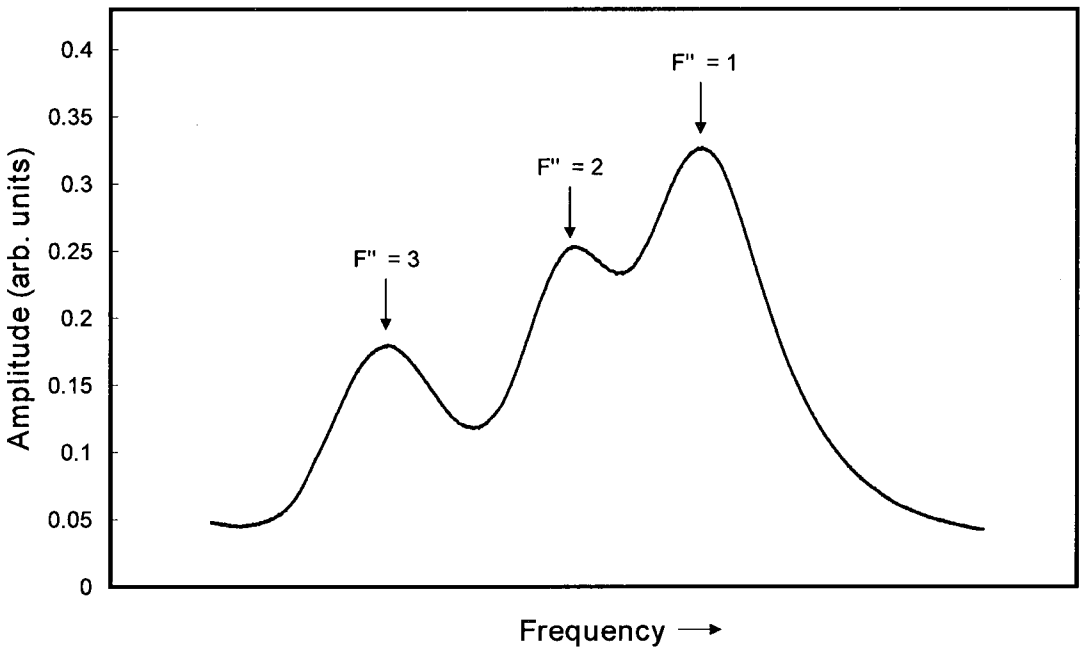

(b) ^{87}Rb

FIG. 36: The signal detected at 420 nm (blue signal) as a result of the decay from $6P_{3/2}$ state to $5S_{1/2}$ state in (a) ^{85}Rb and (b) ^{87}Rb.

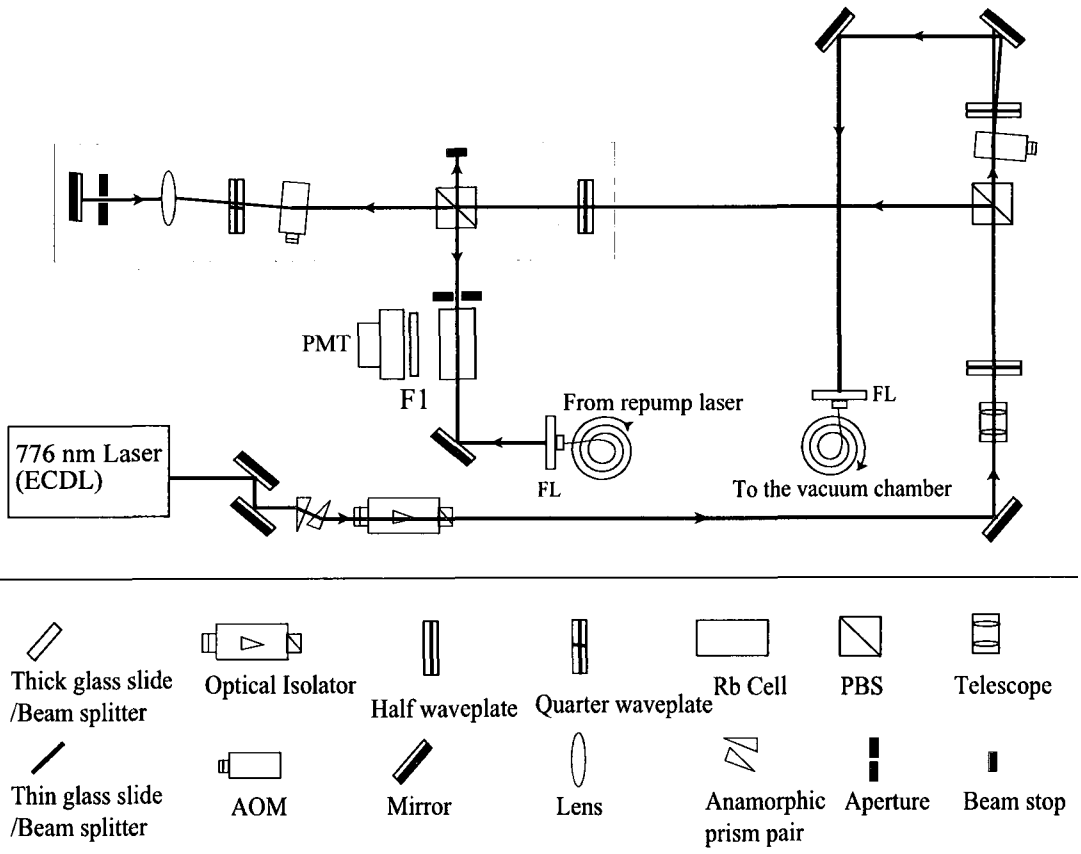

FIG. 37: The optical setup of the 776 nm laser beam. Here FL = fiber launcher and F1 = 420 nm filter.

last section for the kick beam, it was overlapped with the MOT. Then we put back the 776 nm beam for final alignment with the FORT. The beam size at the MOT is about the same as that of the Nd:YAG beam which has a calculated waist of 16 μm for the inhomogeneous broadening experiment. For the two-photon spectroscopy experiment, the beam size is about half the size of the MOT to ensure that the atoms in the FORT experience a spatially uniform intensity. So overlapping the beam with the MOT does not necessarily mean it is overlapped with the FORT. We noticed that when locking the 776 nm laser to one of the $5P_{3/2} \rightarrow 5D_{5/2}$ possible transitions, the MOT signal decreases as the 776 nm laser beam starts to overlap with the Nd:YAG laser beam. This effect is due to photo-ionization of the atoms by the 1064 nm Nd:YAG laser [71]. This was used to ensure the perfect overlapping of the two beams by monitoring the MOT signal from the PMT on the digital scope while changing the position of the 776 nm beam. The beam was set at the position where we notice maximum loss of the MOT signal with the lowest 776 nm power used.

III.8 MEASUREMENT AND DATA ACQUISITION CONTROL

The timing of lasers, magnetic field, and measuring the MOT level and FORT level is performed by a control and data acquisition (DAQ) system. As mentioned before the number of atoms in the MOT and FORT is measured using a photomultiplier tube (PMT) which relies on detecting the fluorescence signal and knowing both the laser parameters and the geometry and efficiency of the detector. Fig. 38 shows the optical and electronic setup to convert the fluorescence signal to a voltage and integrate it before sending it to the data acquisition (DAQ) system. The current from the PMT output is sent to an integrator box which consists of an I-to-V converter with a gain control and a dc offset, an IC switch which allows control from the DAQ system, and an integrator. The integrated output is then sent to the DAQ system where the MOT voltage and the FORT voltage are measured and compared to determine how many atoms are loaded from the MOT to the FORT.

The experiment control system consists of a personal computer (PC), National Instrument data acquisition (DAQ) cards and breakout boxes, and a program using LabVIEW 6 to run the sequences of loading. A LabVIEW program is comprised of two parts; a front panel and a block diagram. The block diagram contains command icons as a replacement of command lines in other program languages such as

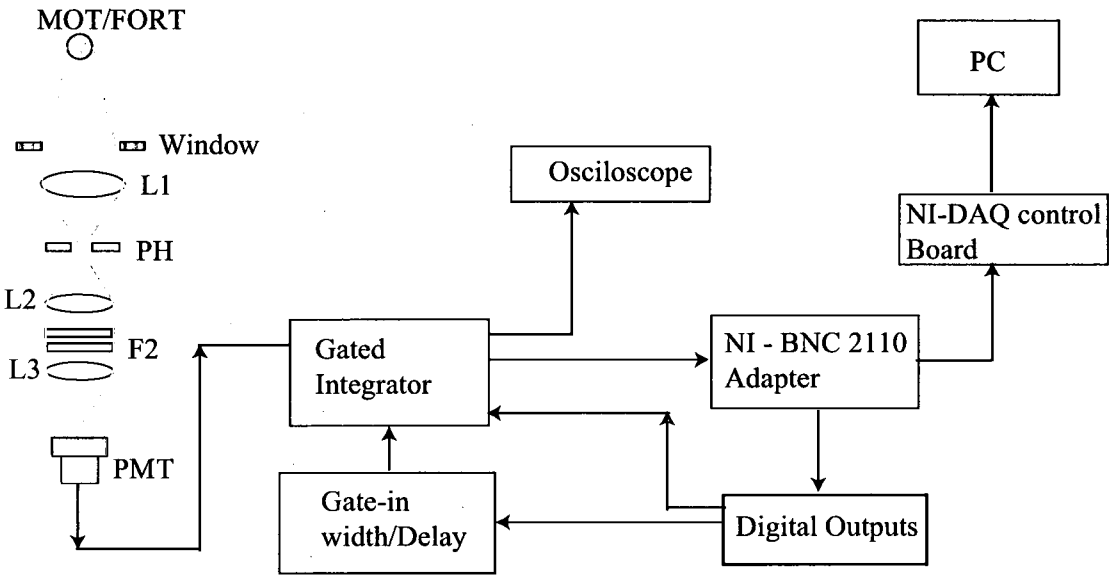

FIG. 38: Optical setup and electronics used to convert the fluorescence of the MOT and FORT cloud to voltage signals and to measure them with the DAQ system. L1 = 44 mm, L2 = 38.01 mm (KPX079 Newport), and L3 = 60 mm (LA1134 Thorlabs) are lenses. F1 = interference filter (MG03F1L056) and F2 = short pass filter (FES0850 Thorlabs). PMT = photomultiplier tube (Hamamatsu R928) and PH = pinhole.

FORTRAN and C. The front panel has controls and indicators that have a direct connection to the experiment hardware via a PCI card. Figs. 39 and 40 show a typical front panel and a typical block diagram of our LabVIEW program, respectively. The program controls the trap beam, repump beam, kick beam, 776 nm beam, FORT laser beam and the magnetic anti-Helmholtz current via switching circuits. It also control the intensity of the repump beam by connecting the analog output of the DAQ devices to the voltage-controlled attenuator in the switching circuit. The detuning of trap beam frequency also can be controlled by varying the output voltage of the voltage controlled oscillator (VCO) in the detuning system. Fig. 41 shows the schematics for the data acquisition and measurement control system. The timing sequence for each experiment will be presented in Chapter IV.

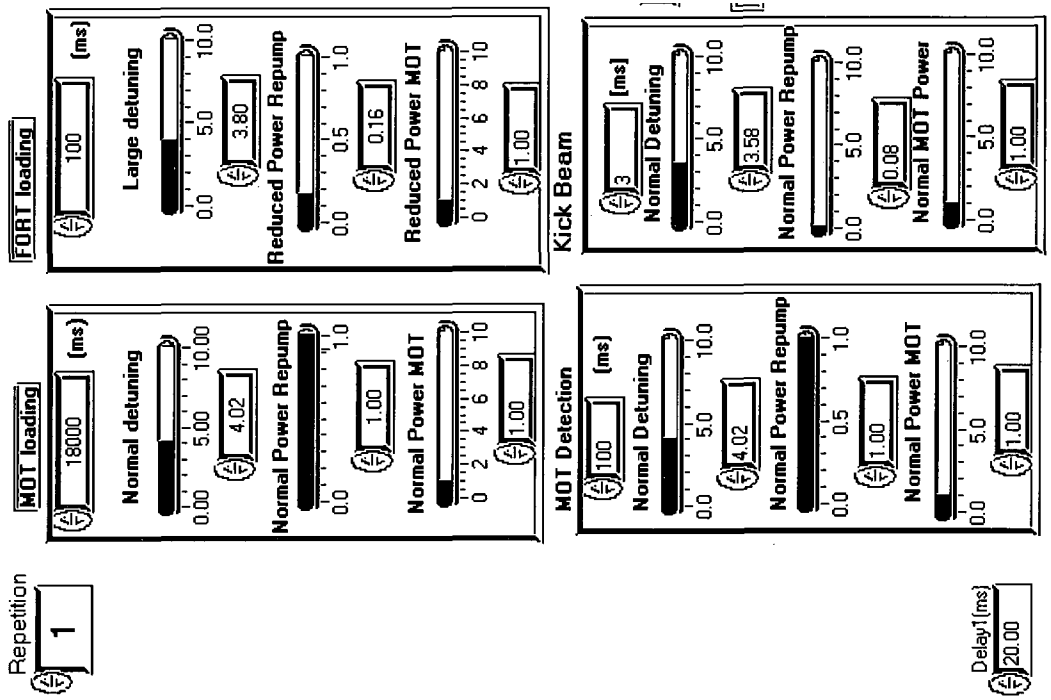

FIG. 39: A typical front panel of the LabVIEW programs we have written to control the data acquisition for these experiments.

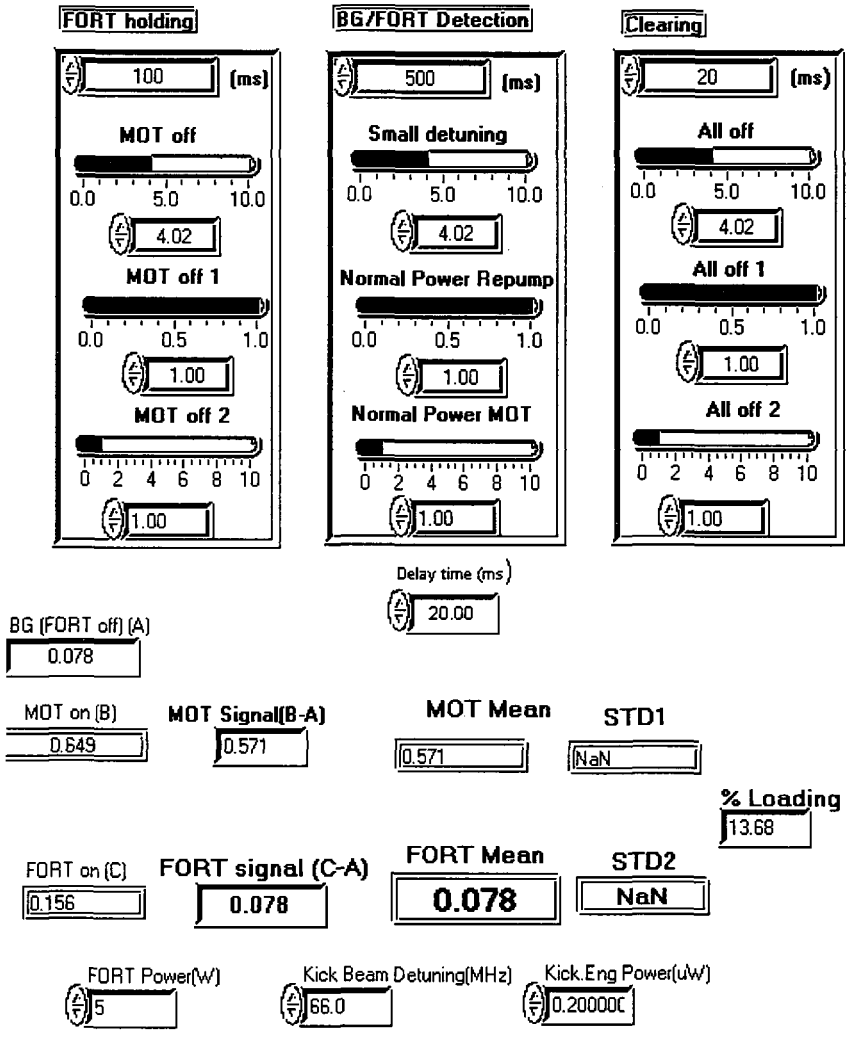
FORT holding
100
(ms)
MOT off
0.0 5.0 10.0
4.02
MOT off 1
0.0 0.5 1.0
1.00
MOT off 2
0 2 4 6 8 10
1.00
BG/FORT Detection
500
(ms)
Small detuning
0.0 5.0 10.0
4.02
Normal Power Repump
0.0 0.5 1.0
1.00
Normal Power MOT
0 2 4 6 8 10
1.00
Clearing
20
(ms)
All off
0.0 5.0 10.0
4.02
All off 1
0.0 0.5 1.0
1.00
All off 2
0 2 4 6 8 10
1.00
Delay time (ms)
20.00
BG (FORT off) (A)
0.078
MOT on (B)
0.649
MOT Signal(B-A)
0.571
MOT Mean
0.571
STD1
NaN
% Loading
13.68
FORT on (C)
0.156
FORT signal (C-A)
0.078
FORT Mean
0.078
STD2
NaN
FORT Power(W)
5
Kick Beam Detuning(MHz)
66.0
Kick.Eng Power(uW)
0.20000

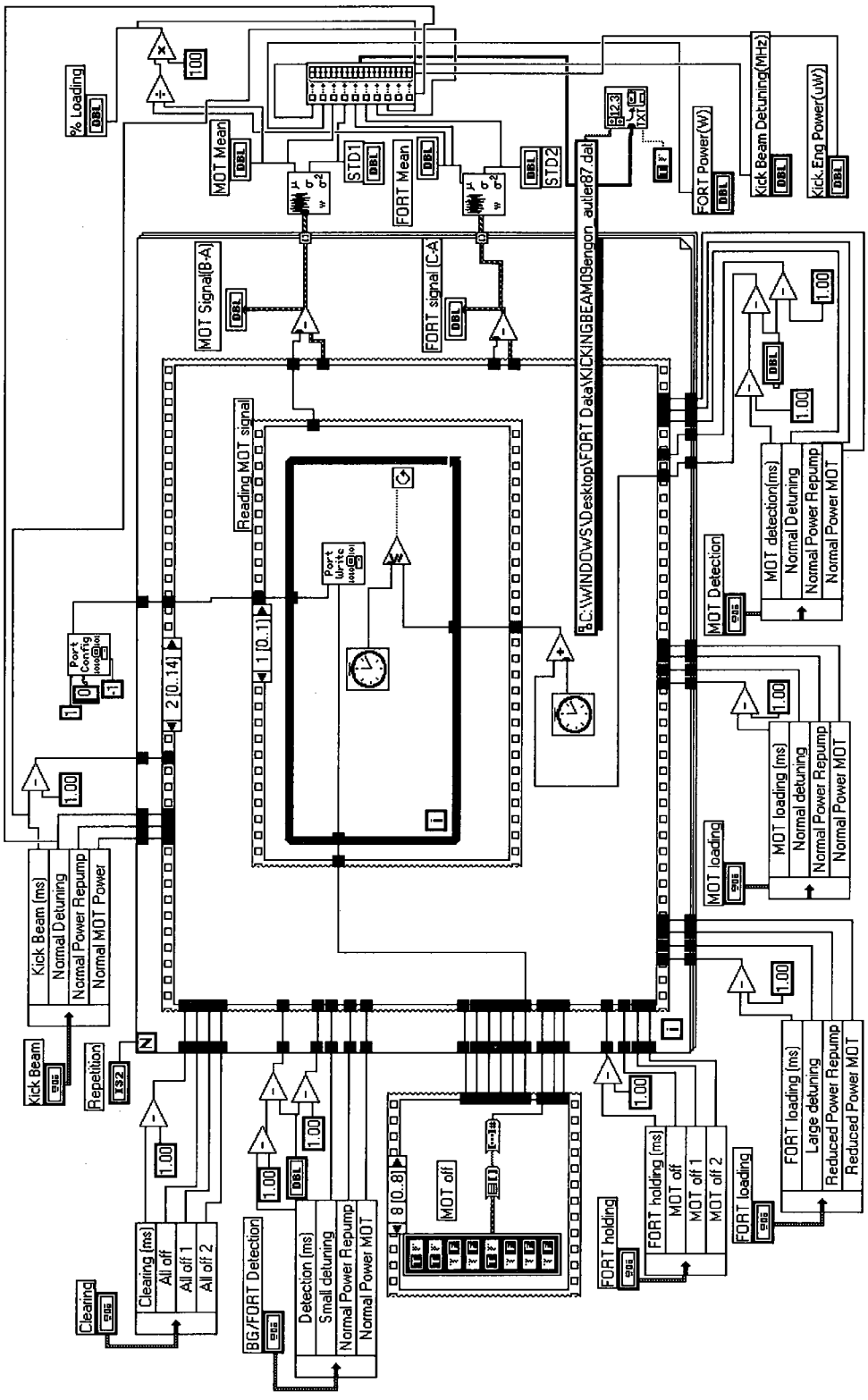

FIG. 40: A typical block diagram of the LabVIEW programs we have written to control the data acquisition for these experiments.

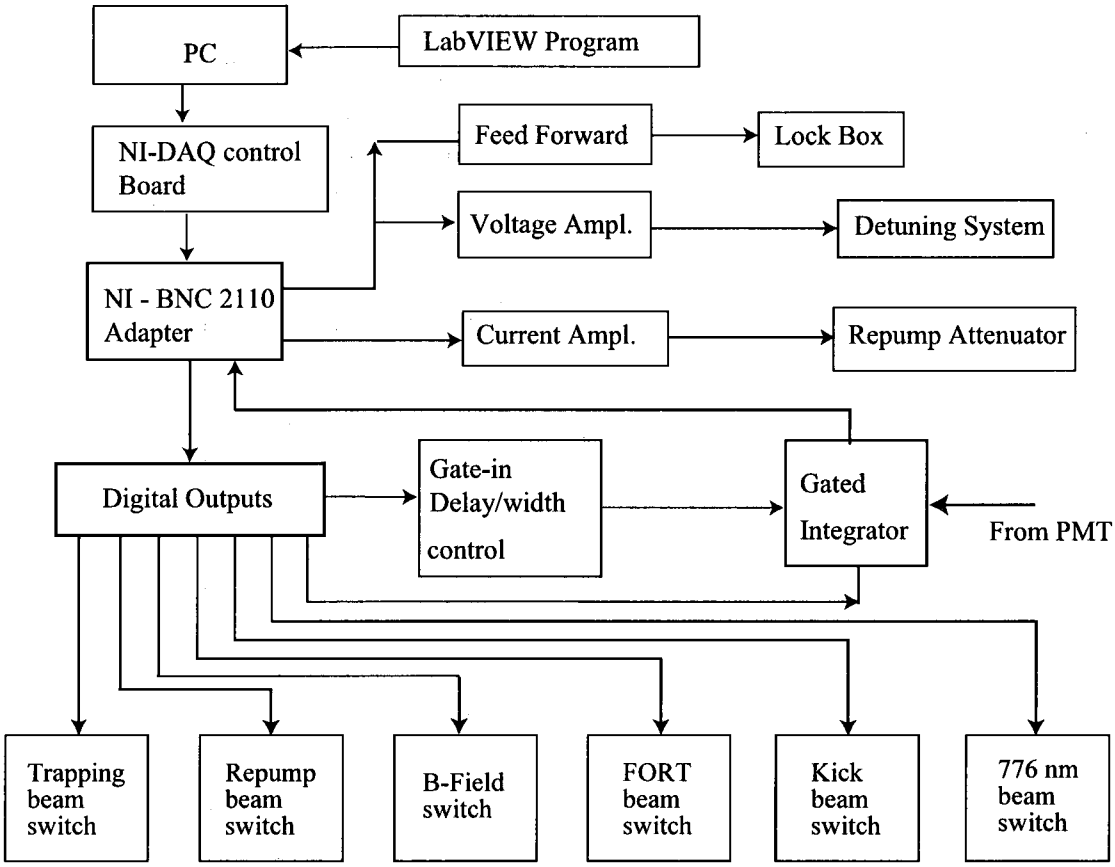

FIG. 41: Block diagram of the data acquisition (DAQ) control.

CHAPTER IV

RESULTS AND DISCUSSION

As mentioned before, different experiments were performed on the atoms in the FORT. The kick beam experiment, the Autler-Townes experiment and the inhomogeneous broadening experiment. A LabVIEW program was used in each experiment to control all the different parameters. The difference in the program between the three experiments is only during the spectroscopy stage. The program starts by loading the MOT for 18 s, then comes the FORT loading stage for 100 ms where we change the detuning of the MOT laser and the intensity of the hyperfine repump laser. After the loading stage, the atoms are held in the FORT for about 100 ms. Following the holding stage, the spectroscopy lasers are then turned on for about 3-6 ms. The status of different parameters during that time as well as the detection method used will be explained for the different experiments, and the results of the experiments will be presented and discussed.

IV.1 KICK BEAM EXPERIMENT

The first spectroscopy experiment we performed on the ^{85}Rb atoms in the optical dipole trap was the "kick beam experiment". The goal of this experiment was to study and compare the shift of the energy levels of the atoms in the cw and pulsed trap. Some data were also taken for circularly polarized trap versus linearly polarized trap. During the spectroscopy (kick) stage, we turn on the kick laser with the hyperfine repump laser for about 3-6 ms. Then we detect the number of atoms remaining in the FORT. This is done after turning off the Nd:YAG laser and turning on the MOT beams with the hyperfine repump laser and measuring the fluorescence of the scattered photons using the PMT. By determining the number of atoms kicked out of the trap when the kick beam frequency is scanned, we can determine the spectra of the confined atoms. The kick laser frequency was scanned over the $F = 3$ to $F' = 2, 3, 4$ transitions. Since the coupling strengths (from the Clebsch-Gordon coefficients) for the $F = 3$ to $F' = 2, 3, 4$ transitions are in the ratio of $1 : 4 : 8$, respectively [46], the time for the spectroscopy stage has to be changed while the kick laser was scanned over the different hyperfine transitions. The kick time was 6 ms for $F = 3$ to $F' = 2$ transition, 4 ms for $F = 3$ to $F' = 3$, and 3 ms for $F = 3$ to

$F' = 4$. The choice of a 3-6 ms duration for the kick beam was obtained after several trials on different kick beam powers and kick beam time and it was found that 3-6 ms kick beam duration and 10 μW kick beam power with 1 mm beam radius yielded the biggest attenuation with minimum power broadening of the spectra. The diameter of the beam is made bigger than the MOT cloud to ensure that the atoms in the FORT experience a spatially uniform intensity. Without the hyperfine repump laser during the kick stage, the atoms were not kicked out from the FORT when the kick laser frequency was scanned around the $F = 3$ to $F' = 2$ and $F' = 3$ transitions. This is because the atoms fall to $F = 2$ dark state and hence stop scattering by the kick beam. This was confirmed by performing the kick experiment on the atoms in the MOT first, Fig. 42. The timing sequence of the program used in this kicking experiment with the condition of the different parameters is shown in Fig. 43. In this section, the data and analysis will be presented and a comparison between the different trap kinds (cw, pulsed) and polarizations (linear, circular) will be done.

IV.1.1 Linearly Polarized FORT

From Sec. II.5, the dipole potential for linearly polarized laser light with a Gaussian profile is given by

$$U(r) = -U_0 e^{-2r^2/w_0^2}, \tag{88}$$

where U_0 is the minimum potential (well depth) of the trap at $r = 0$ which is already given in Eq. (49)

$$U_0 = \frac{\hbar \Gamma^2 I_0}{24 I_{\text{sat}}} \left(\frac{1}{\Delta_{1/2}} + \frac{2}{\Delta_{3/2}} \right). \tag{89}$$

For 5 Watts Nd:YAG laser power focused to a calculated waist of $\sim$ 16 μm, the potential well depth from Eq. (89), which uses the rotating wave approximation, is 1.6 mK ($\sim$ 30 MHz). Also, for linearly polarized laser light $\vec{E}(t) = \vec{\mathcal{E}} e^{-i\omega t} + \vec{\mathcal{E}}^* e^{i\omega t}$ of angular frequency ω, with $\vec{\mathcal{E}} = \mathcal{E}_0 \hat{z}$, the energy shift of the $5S_{1/2}$ state is given by

$$U_0 \left(5S_{1/2}\right) = -\alpha_S \left|\mathcal{E}_0\right|^2, \tag{90}$$

where α_S is the scalar polarizability of $5S_{1/2}$ state which has a calculated value of 680 a_o^3 at 1064 nm (the calculation of the polarizability is discussed in Sec. IV.3),

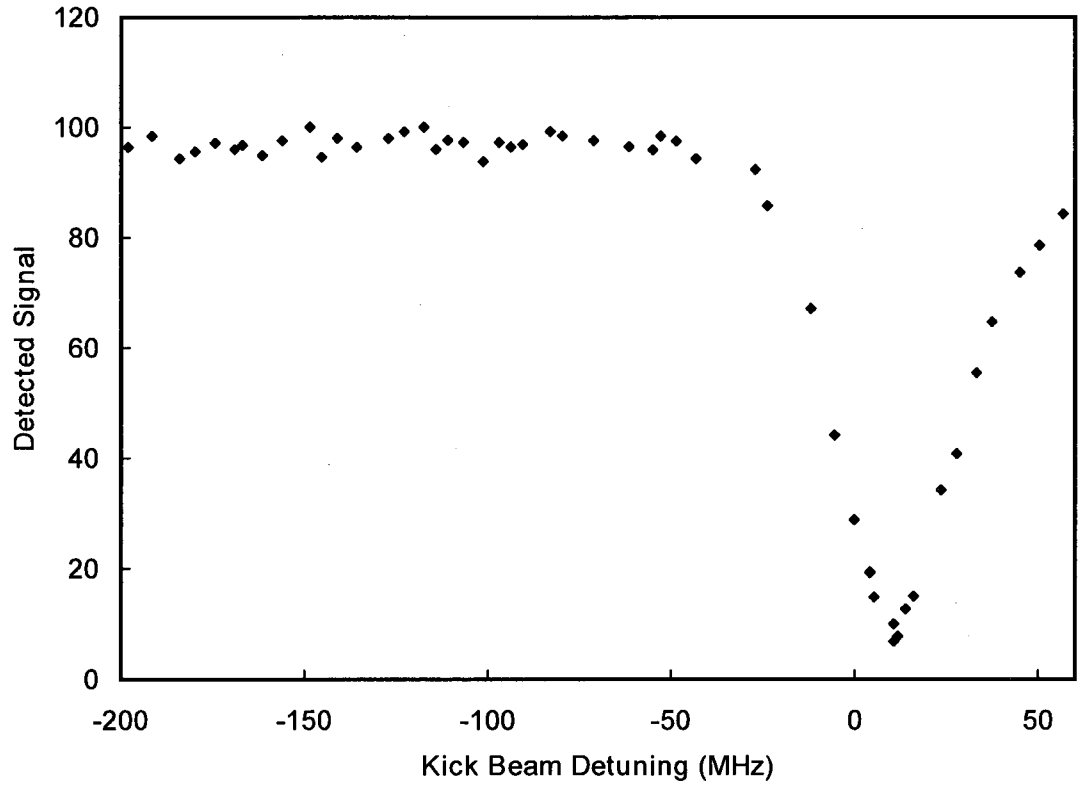

FIG. 42: Detected signal of the MOT as a function of the kick beam detuning from the $F = 3$ to $F' = 4$ resonance with hyperfine laser off during the kick time for 100 μW kick beam power, 1 mm beam radius, and 5.5 ms kick time.

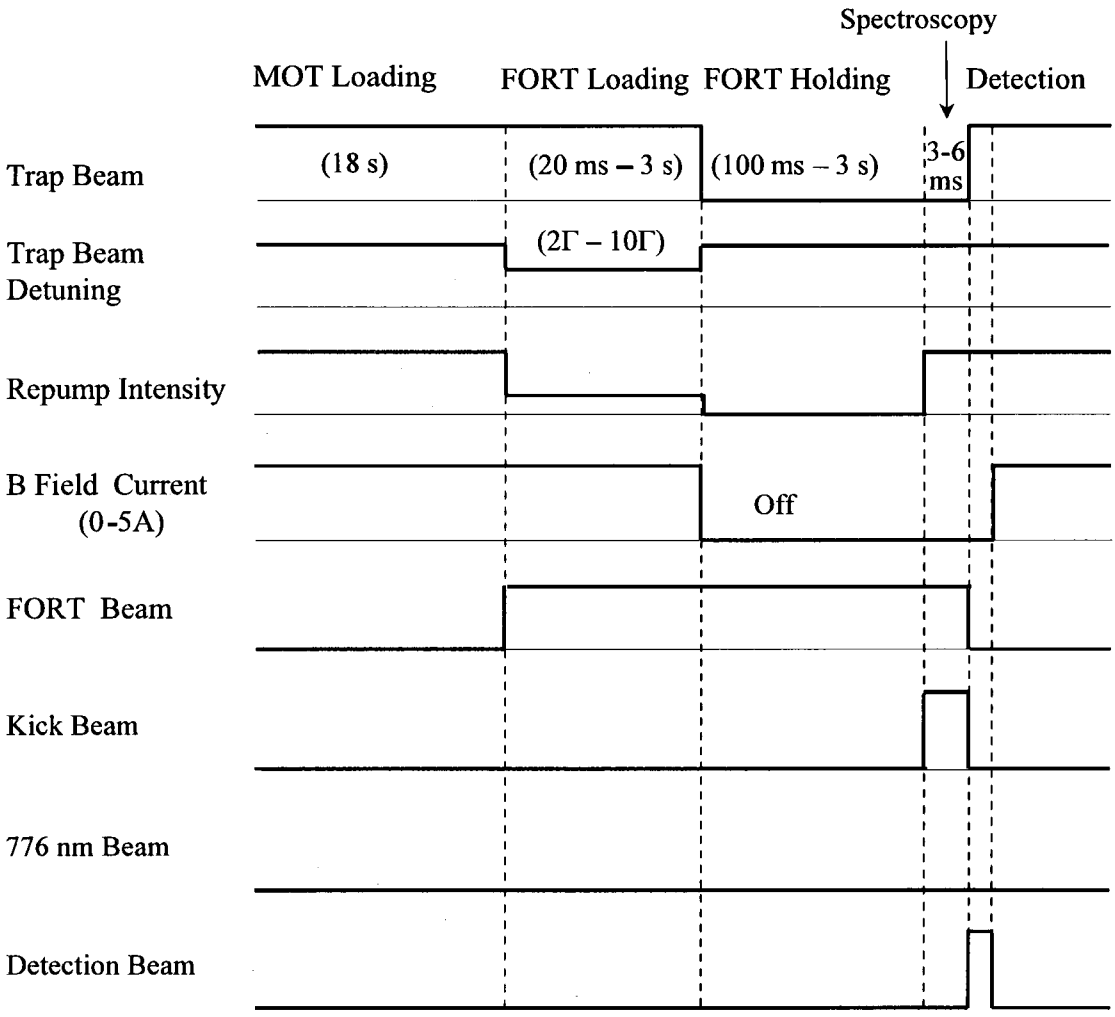

FIG. 43: Kick experiment timing sequence for the different parameters controlled by the DAQ system.

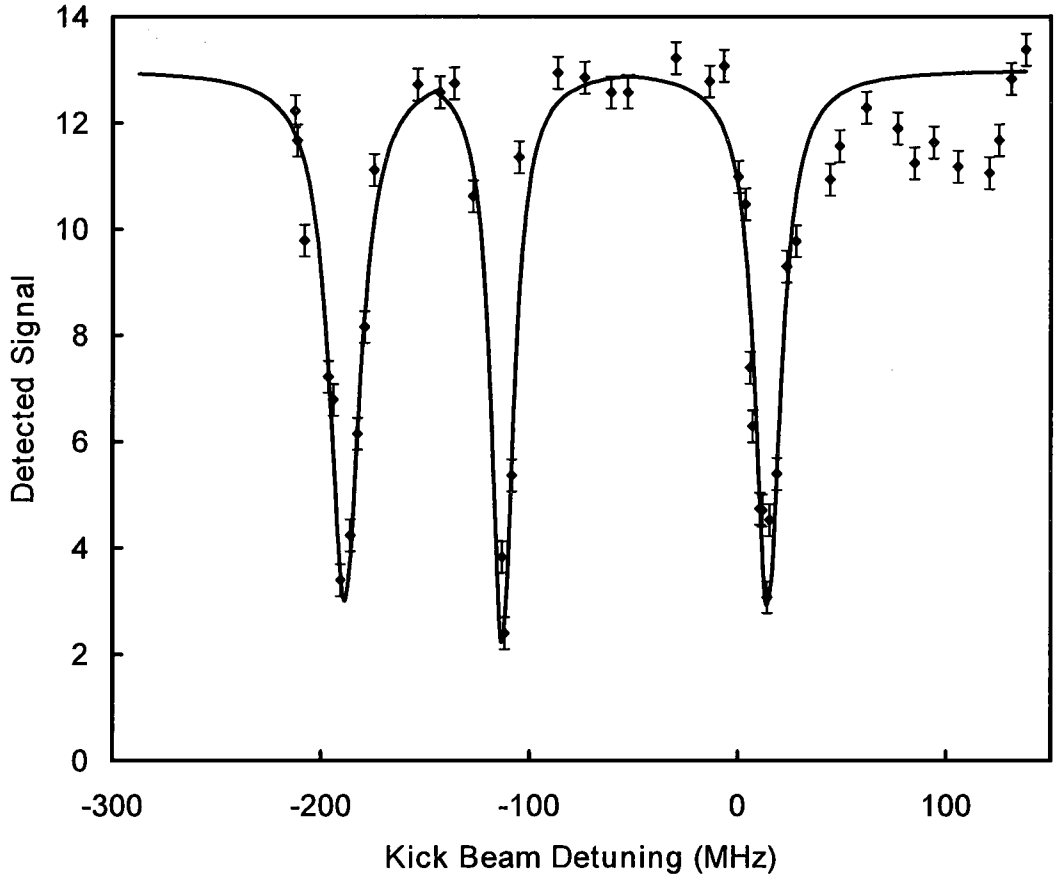

FIG. 44: Detected signal of the linearly polarized cw FORT as a function of the kick beam detuning from the unperturbed $F = 3$ to $F' = 4$ resonance for 5 Watts FORT laser power, 10 μW kick beam power and 1 mm kick beam radius.

$|\mathcal{E}_0|^2 = I_0/2\varepsilon_0 c$. Using Eq. (90) the resulting shift for 5 Watts of Nd:YAG laser power focused to a calculated waist of $\sim$ 16 μm is 1.88 mK ($\sim$ 39 MHz).

Fig. 44 shows the "detected signal" of the linearly polarized cw FORT vs the kick beam detuning in MHz from the unperturbed $F = 3$ to $F' = 4$ resonance. We use the term detected signal to represent the number of atoms in the FORT (as a percentage of the number of atoms initially in the MOT) after either loading, or loading and exposure to the probe beam. Resonances are observed to be AC Stark-shifted about 15 MHz with respect to the resonances in free atoms. Note that this is less than would be expected using the calculated trap waist of 16μm, indicating that our trap waist is likely somewhat larger than this value ($\sim 2\times$). This result is in agreement with the earlier work of Shiddiq. The solid lines are fittings to the data that were done manually using different Lorentzian functions to extract the widths of the transitions. The Lorentz function is given by

$$y = y_0 + \frac{2A}{\pi}\frac{w}{4(x - x_c)^2 + w^2}, \tag{91}$$

where y_0 is the offset, A is the area, w is the width, and x_c is the center.

The widths for $F = 3$ to $F' = 2, 3, 4$ transitions spectra are 17 MHz, 13 MHz, and 15 MHz, respectively. There are different factors that can contribute to the broadening of the spectra, such as the bandwidth of the diode laser used ($\sim$ 1 MHz), power broadening, and inhomogeneous broadening. The power broadening was minimized by trying out different kick beam powers and choosing the one that gives the biggest attenuation with minimum broadening of the spectra. Since the light field used to form the optical dipole trap is not homogeneous (it has a Gaussian intensity profile), it produces a spatially dependent light shift; $\Delta E(r)$, which causes the inhomogeneous broadening (which is discussed in more details in Sec. II.7, IV.3).

The data taken for the linearly polarized pulsed FORT along with the fitting is shown in Fig. 45. With the same parameters used for the cw FORT; 5 Watts FORT laser power, 10 μW kick beam power, 1 mm kick beam radius, and with the same timing, the extracted widths for $F = 3$ to $F' = 2, 3, 4$ transitions spectra are 23 MHz, 25 MHz, and 29 MHz, respectively. Notice that these are slightly larger than the widths measured for the cw FORT, thus indicating that atoms in the the cw and pulsed FORTs do not display identical responses to the spectroscopy probe beam under otherwise identical conditions.

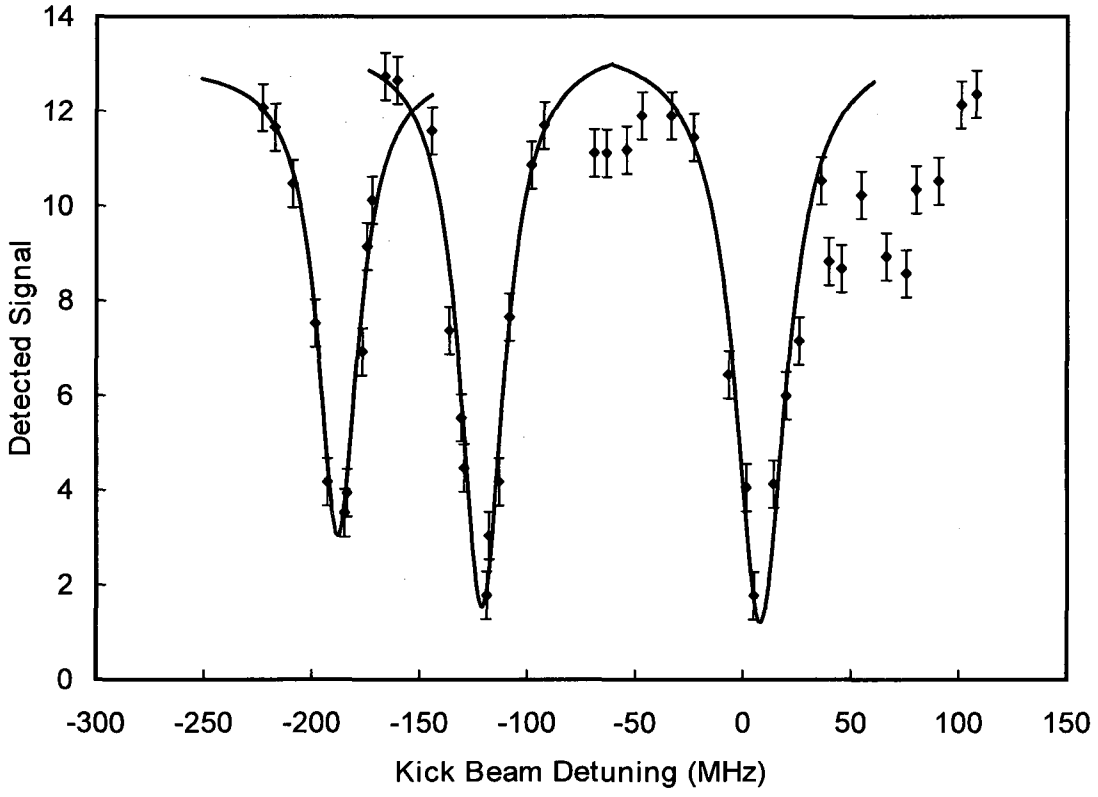

FIG. 45: Detected signal of linearly polarized pulsed FORT as a function of the kick beam detuning from the unperturbed $F = 3$ to $F' = 4$ resonance for 5 Watts FORT laser power, 10 μW kick beam power and 1 mm kick beam radius.

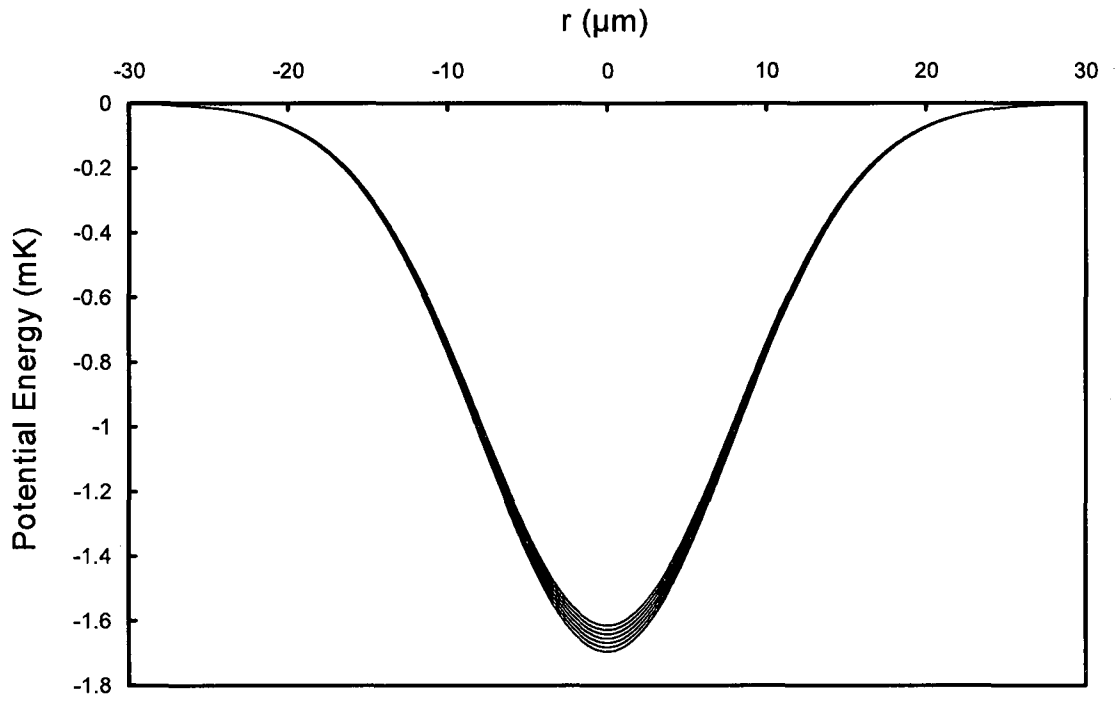

FIG. 46: Radial cross-sections of the potentials for different m_F levels of the $5^2S_{1/2}$ and $F = 3$ ground state in the focus of a circularly polarized Gaussian beam for 5 Watts Nd:YAG laser power and 16 μm focused beam waist.

IV.1.2 Circularly Polarized FORT

For FORT laser with polarization vector $\hat{\varepsilon} = 1/\sqrt{2}(\hat{x}\sqrt{1+\epsilon} + i\hat{y}\sqrt{1-\epsilon})$, where ϵ is the ellipticity, the potential depth is written as [38],

$$U_0\,(I,\,\lambda,\,F,\,m_F,\,\epsilon) = \frac{\hbar\Gamma^2 I_0}{24 I_{sat}}\left[\left(\frac{1}{\Delta_{1/2}} + \frac{2}{\Delta_{3/2}}\right) - g_F m_F \eta\left(\frac{1}{\Delta_{1/2}} - \frac{1}{\Delta_{3/2}}\right)\right], \quad (92)$$

where m_F is the Zeeman sublevel of the atom, $g_F = [F(F+1) + S(S+1) - I(I+1)]/[F(F+1)]$ is the Landé g-factor for the given F, and $\eta = |\hat{\varepsilon} \times \hat{\varepsilon}^*| = \sqrt{1-\epsilon^2}$. For circularly polarized FORT light $\eta = 1$, hence the degeneracy of the energy level is broken.

The general equation for a focused Gaussian beam of peak intensity I_0 is written as [56]

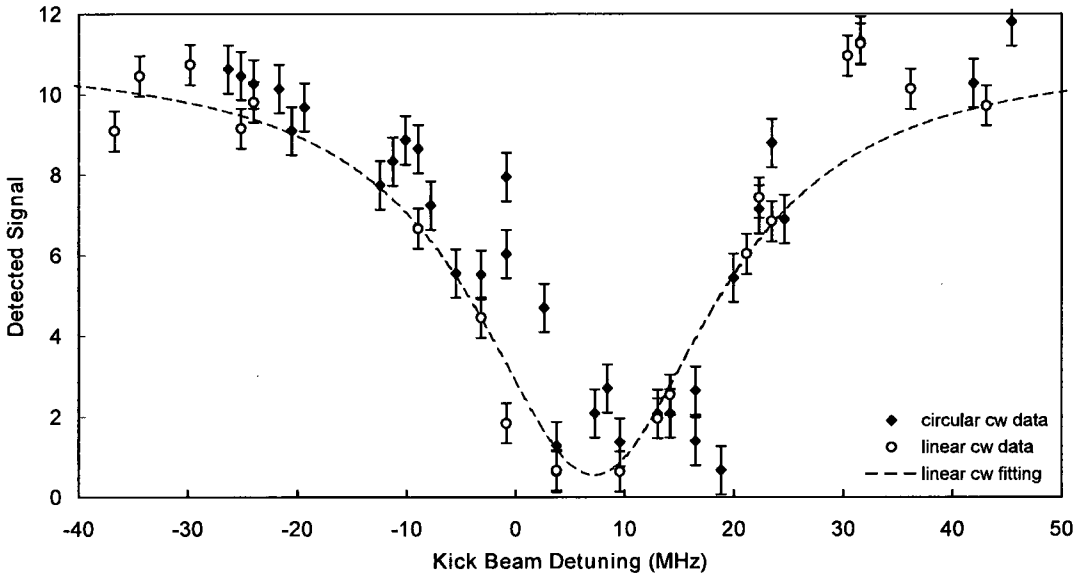

FIG. 47: Detected signal of the circularly polarized cw FORT as a function of the kick beam detuning from the unperturbed $F = 3$ to $F' = 4$ resonance for 5 Watts FORT laser power, 3 ms kick time, 10 μW kick beam power and 1 mm kick beam radius.

$$U(r) = \frac{\hbar\Gamma^2 I_0}{24 I_{sat}} \left[\left(\frac{1}{\Delta_{1/2}} + \frac{2}{\Delta_{3/2}} \right) - g_F m_F \eta \left(\frac{1}{\Delta_{1/2}} - \frac{1}{\Delta_{3/2}} \right) \right] e^{-2r^2/w_0^2}. \qquad (93)$$

Fig. 46 shows the AC Stark shift $U(r)$ in the focus of a circularly polarized Gaussian laser beam for different m_F levels of the $5^2S_{1/2}$ and $F = 3$ ground state, for FORT laser power of 5 Watts focused to 16 μm waist. The separation between the different m_F levels is 13 μK ($\sim$ 0.3 MHz) with $m_F = -3$ has the maximum shift. This difference in the shift between the sublevels is hard to resolve in the data taken for the circularly polarized FORT. Fig. 47 shows the data taken for linearly polarized cw FORT and that for circularly polarized cw FORT, the data were taken on the same day with the same experiment parameters (5 Watts FORT laser power, 3 ms kick time, 10 μW kick beam power and 1 mm kick beam radius). The dashed line represents the fitting for the linearly polarized FORT data. The data shows that there is a slight difference between the linearly polarized and the circularly polarized FORT, therefore performing higher resolution spectroscopy is required.

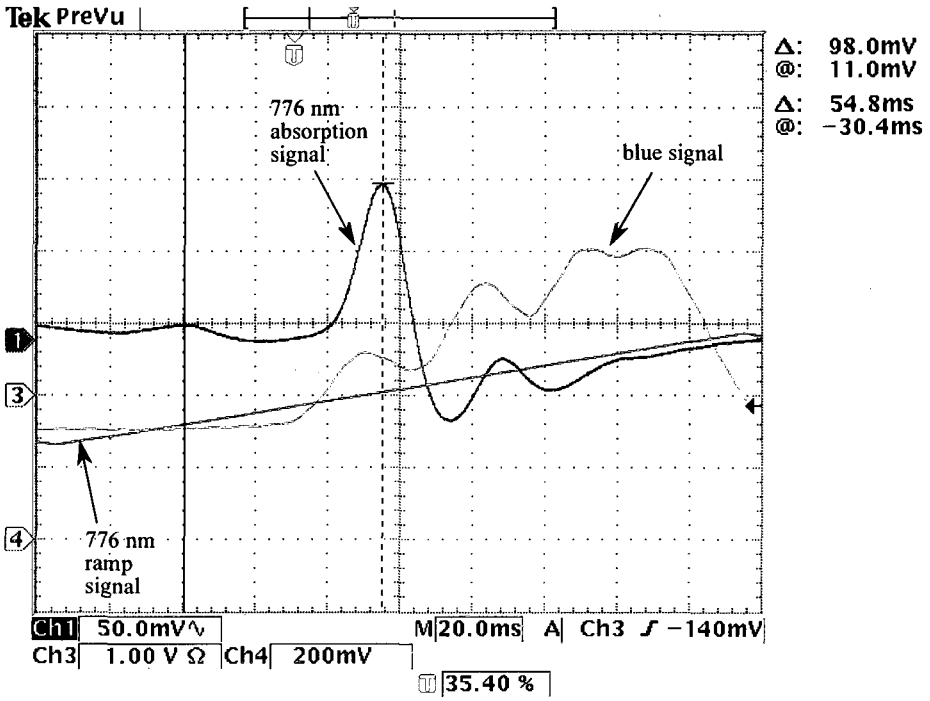

FIG. 48: Absorption of 776 nm laser beam in the ^{85}Rb MOT for -2Γ pump laser detuning.

IV.2 AUTLER-TOWNES EXPERIMENT

For a further study of the atoms in the MOT and the FORT, we performed an optical double resonance spectroscopy. The atoms are cooled on the $5S_{1/2} \rightarrow 5P_{3/2}$ transition and the absorption of a weak probe beam tuned to the $5P_{3/2} \rightarrow 5D_{5/2}$ transition is detected. The MOT laser beams are used as the pump laser to provide the first step transition ($5S_{1/2} \rightarrow 5P_{3/2}$) and the 776 nm laser beam is our probe beam which is scanned across the second transition ($5P_{3/2} \rightarrow 5D_{5/2}$). With the MOT laser tuned below resonance, the spectrum of the $5P_{3/2} \rightarrow 5D_{5/2}$ transitions (the probe) can be expected to display the characteristic double-peak structure of an Autler-Townes splitting. In this section, the data obtained for both isotopes in the MOT and the FORT will be presented.

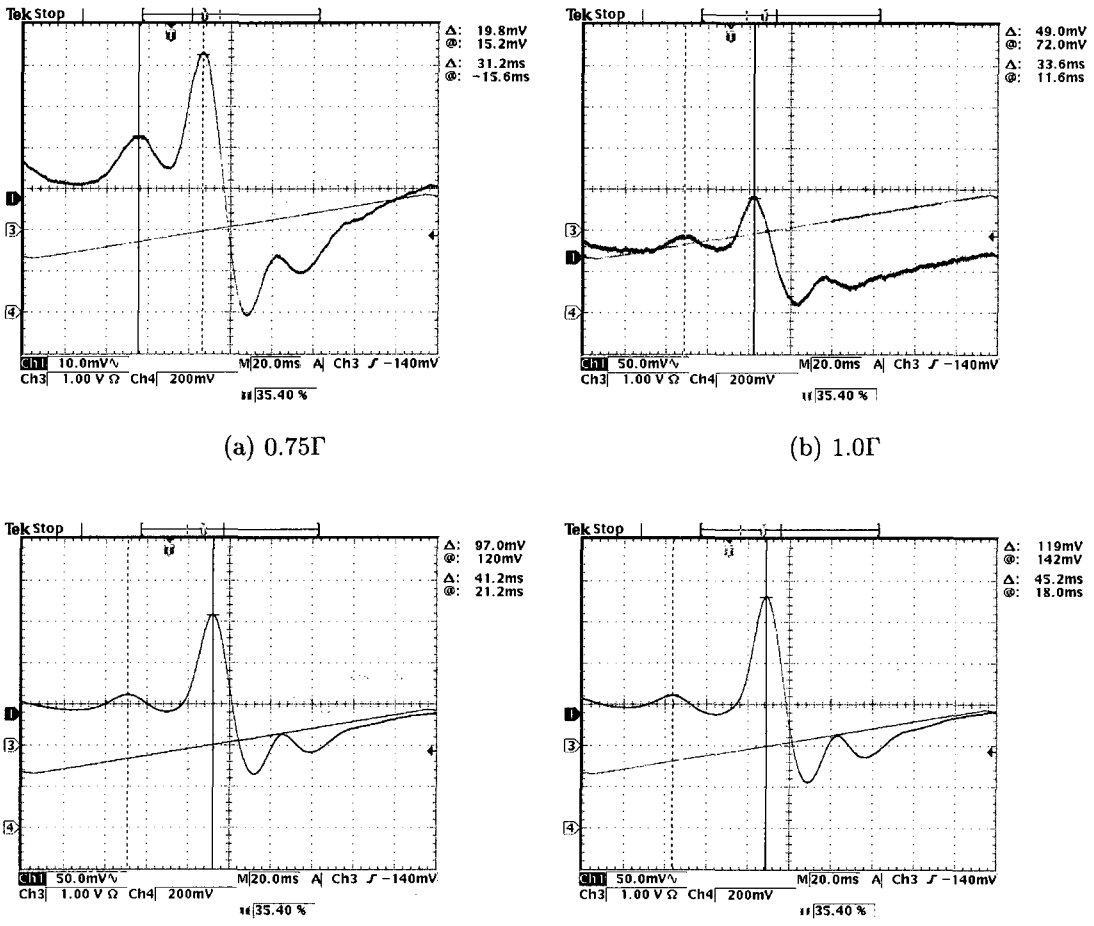

(a) 0.75Γ

(b) 1.0Γ

(c) 1.25Γ

(d) 1.5Γ

FIG. 49: Absorption of the 776 nm laser beam in the ^{85}Rb MOT for different pump laser detunings from 0.75Γ to 1.5Γ.

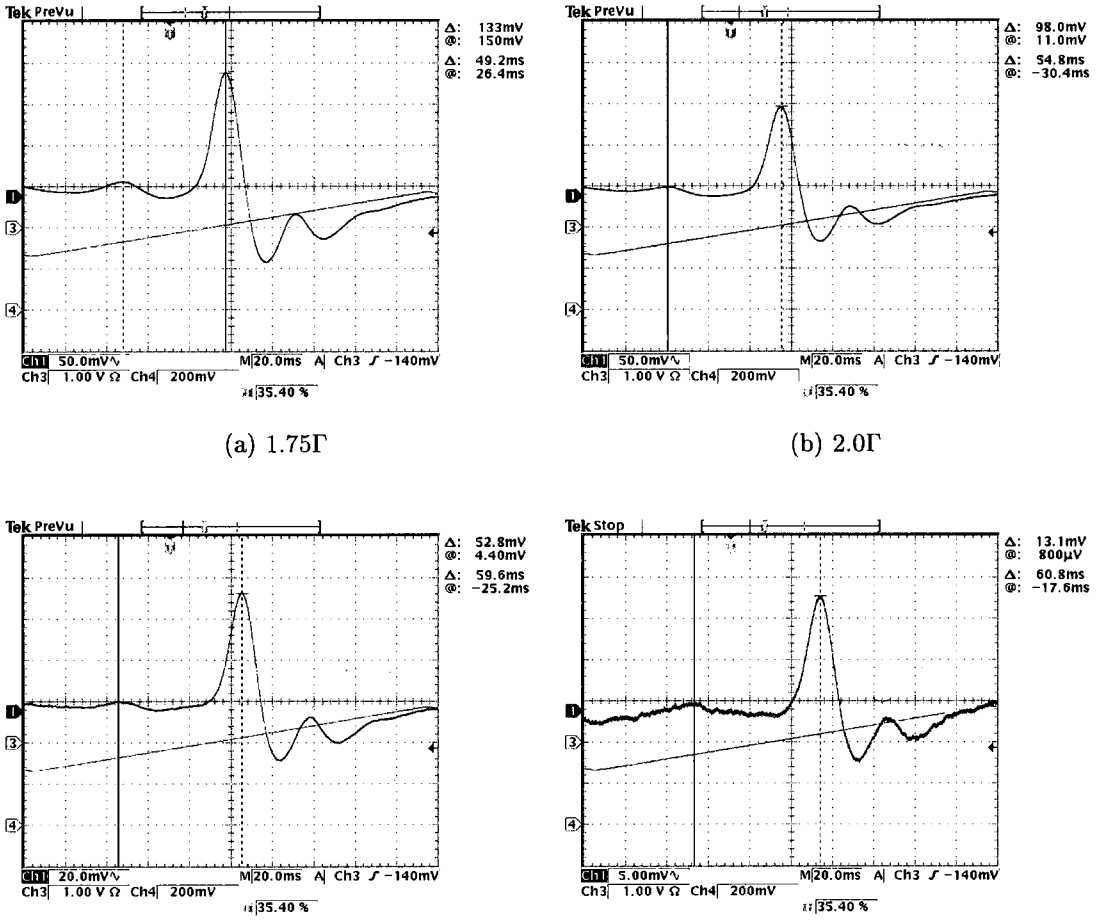

(a) 1.75Γ (b) 2.0Γ

(c) 2.25Γ (d) 2.5Γ

FIG. 50: Absorption of the 776 nm laser beam in the ^{85}Rb MOT for different pump laser detunings from 1.75Γ to 2.5Γ.

IV.2.1 MOT Data and Analysis

We have observed the Autler-Townes effect in both isotopes, ^{85}Rb and ^{87}Rb. The effect was studied as a function of the pump beam detuning from the first step transition. With the pump laser frequency fixed at a specific detuning, the two-photon resonance is observed by scanning the frequency of the 776 nm laser and measuring its absorption with a photodiode. The absorption signal was sent to a lock-in amplifier to improve the signal to noise ratio. The data shown here are the averages over tens of scans. The detuning of the pump beam is in units of Γ.

In ^{85}Rb, the cooling transition is from $5S_{1/2}(F = 3)$ ground state to $5P_{3/2}(F' = 4)$ excited state and the probe laser (776 nm laser) is scanned through the $5P_{3/2}(F' = 4) \rightarrow 5D_{5/2}(F'')$ resonance. The double resonance to the $5D_{5/2}(F'' = 5)$ state was observed clearly. The absorption spectra of the probe laser is shown in Fig. 48 for a pump laser detuning of -2Γ, and in Figs. 49 and 50 for different pump laser detunings, the 776 nm beam absorption spectra are summarized in Fig. 51. For ^{87}Rb, the cooling transition is from $5S_{1/2}(F = 2)$ ground state to $5P_{3/2}(F' = 3)$ excited state and the probe laser (776 nm laser) is scanned through the $5P_{3/2}(F' = 3) \rightarrow 5D_{5/2}$ resonance. Fig. 52 shows the splitting of the $5P_{3/2}(F' = 3) \rightarrow 5D_{5/2}(F'' = 3, 4)$ resonances for pump laser detuning of -2Γ, and Fig. 49 shows the spectra for different pump laser detuning. The measured Autler-Townes splittings for both isotopes are given in Table 1.

Autler-Townes splitting is given by $\sqrt{\Delta_C^2 + \Omega_R^2}$, where Δ_C is the detuning of the first step transition coupling laser (pump laser), and Ω_R is the Rabi frequency for that transition. Since we are unsure of the initial magnetic sublevel distribution and there is the additional possibility of optical pumping during the probe phase, we treated the Rabi frequency as a free parameter. Using the measured splitting values for different detuning we extracted the value of Rabi frequency. For ^{85}Rb, Ω_R is 7.1-9.4 MHz with an average value of 8.2 MHz. For ^{87}Rb, Ω_R is 6.2-9.6 MHz with an average value of 7.9 MHz. With our measured experimental laser parameters, and taking the MOT laser retro-reflection and various losses into account, we calculate a Rabi frequency of $\sim$15 MHz for the $5S_{1/2}, F = 3, m_F = 3 \rightarrow 5P_{3/2}, F' = 4, m'_F = 4$ transition. This value represents an upper limit on what we would expect to see given that this is the strongest transition between magnetic sublevels for circularly polarized light. Our effective measured Rabi frequencies indicate that there is indeed a distribution of magnetic sublevels in our sample of atoms and that a detailed line

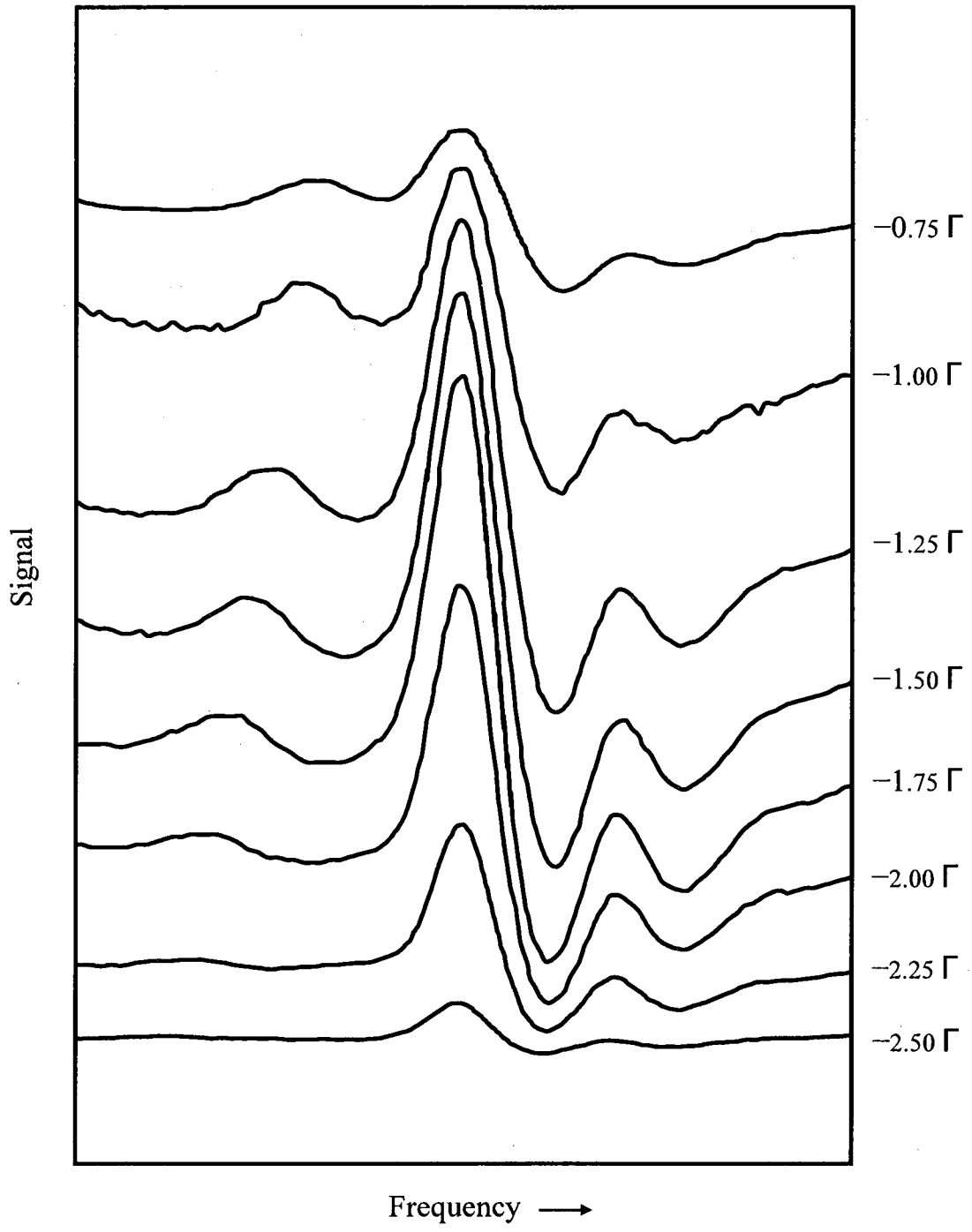

FIG. 51: Absorption of 776 nm laser beam in the ^{85}Rb MOT for different pump laser detuning.

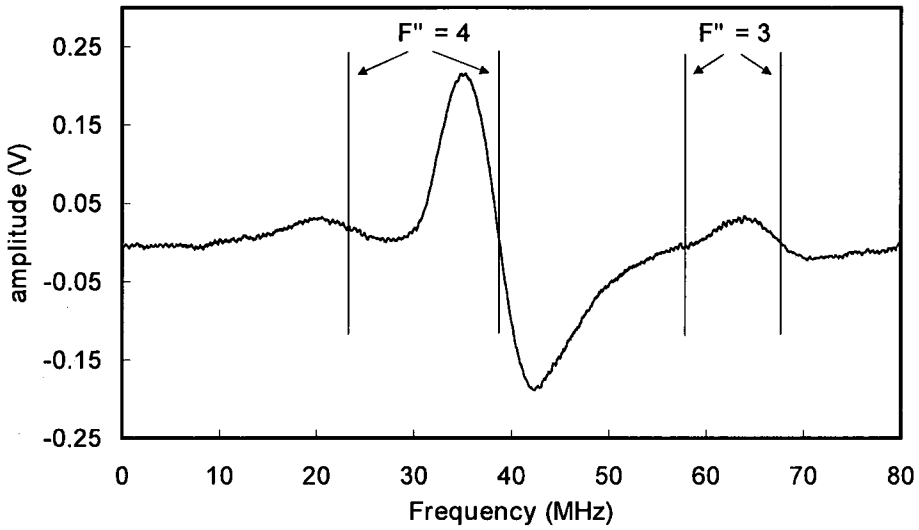

FIG. 52: Absorption of the 776 nm laser beam in the ^{87}Rb MOT for -2Γ pump laser detuning.

TABLE 1: Measured Autler-Townes splittings in ^{85}Rb and ^{87}Rb for different pump beam detuning.

Detuning (Γ)	^{85}Rb splitting (MHz)	^{87}Rb splitting (MHz)
-0.75	8.6	7.6
-1	9.3	9.4
-1.25	11.4	10.3
-1.5	12.5	11.6
-1.75	13.6	12.9
-2	15.1	15
-2.25	16.5	16.4
-2.5	16.8	17.8

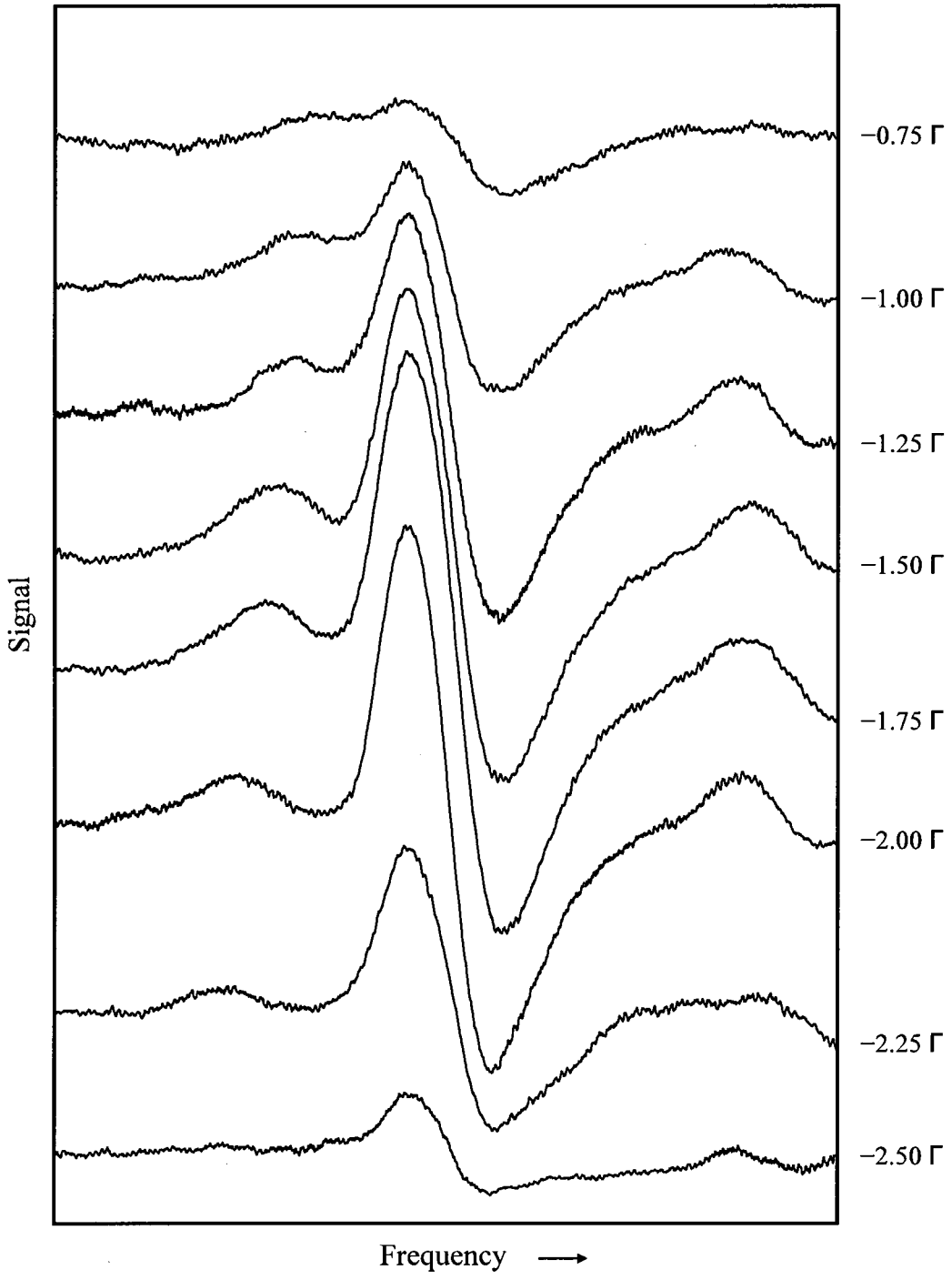

FIG. 53: Absorption of 776 nm laser beam in the ^{87}Rb MOT for different pump laser detuning.

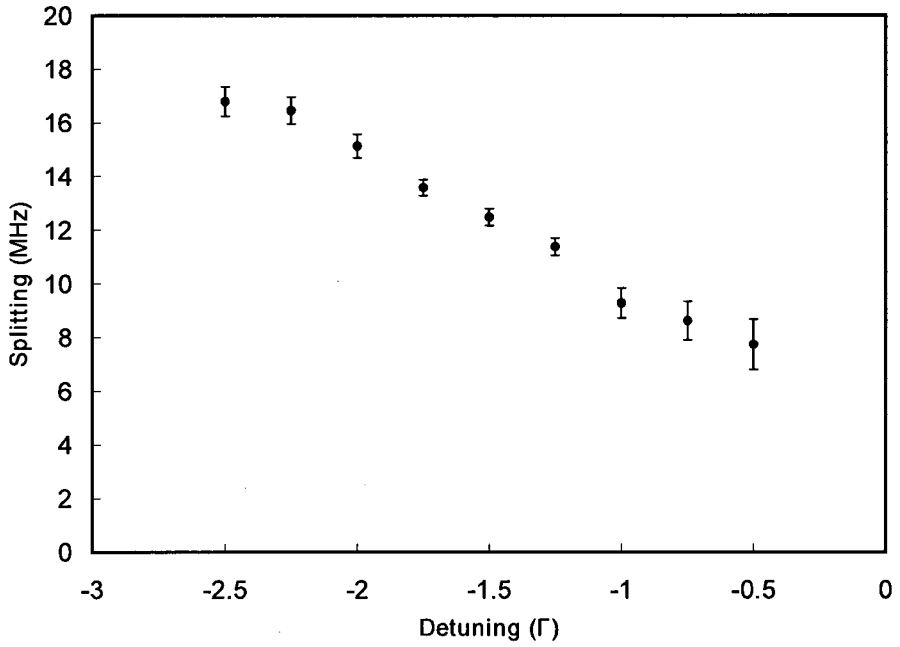

FIG. 54: Autler-Townes splitting in ^{85}Rb as a function of the pump beam detuning in units of Γ.

shape analysis is required to fully characterize the spectra. In addition, one could also look for interference effects in the excitation amplitudes, but our experiment did not have the required sensitivity to investigate this effect [76].

It should be noted that, since we were using a lock-in amplifier to detect the absorption spectra, the splitting should be measured as the difference between the zero crossings of the doublet. This was hard to achieve with high precision as the peaks got closer which can contribute to the variation in the extracted Rabi frequency.

Fig. 54 and Fig. 55 show the splitting in both isotopes versus the pump beam detuning. The error bars represent the uncertainty in measuring the splitting.

IV.2.2 FORT data and analysis

The number of atoms trapped in the FORT will start to decrease after few hundreds of milliseconds due to two-body and background gas collisions as well as scattering of probe laser photons, hence obtaining an absorption signal of the 776 nm beam is hard to achieve because of the need to average over tens of scans. The number of

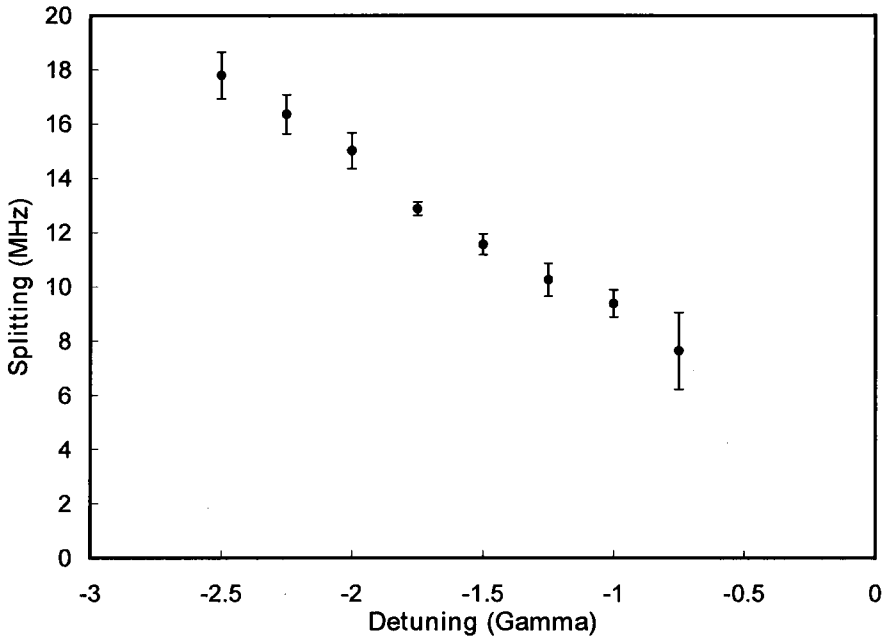

FIG. 55: Autler-Townes splitting in ^{87}Rb as a function of the pump beam detuning in units of Γ.

atoms in the FORT is about 12 % of that in the MOT, which will decrease the signal to noise ratio. Therefore, a different technique has to be used in order to conduct a two-photon spectroscopy experiment on the atoms in the FORT. The presence of the 776 nm laser and the Nd:YAG laser at the same time with the MOT light can cause photo-ionization of the atoms in the dipole trap, by detecting the number of atoms remaining in the FORT while scanning the 776 nm laser frequency we can observe the spectra. 3 ms before the holding stage ends, we turn on the 776 nm beam, the MOT beam, and the hyperfine repump beam, then we detect the number of atoms remaining in the FORT by measuring the florescence using the PMT. The experiment was performed on linearly polarized cw FORT. The timing sequence is shown in Fig. 56.

Fig. 57 shows the detected signal of the ^{85}Rb FORT by scanning the 766 nm laser beam (probe beam) for 5 Watts Nd:YAG laser power, 3 ms probe time, 1 μW probe beam power, and 1 mm probe beam diameter. The pump laser was detuned by -0.5 Γ from the $5S_{1/2}(F = 3) \rightarrow 5P_{3/2}(F' = 4)$ shifted resonance of the atoms in the FORT. From the kick beam experiment, the shift is 15 MHz (2.5 Γ) for Nd:YAG power of 5

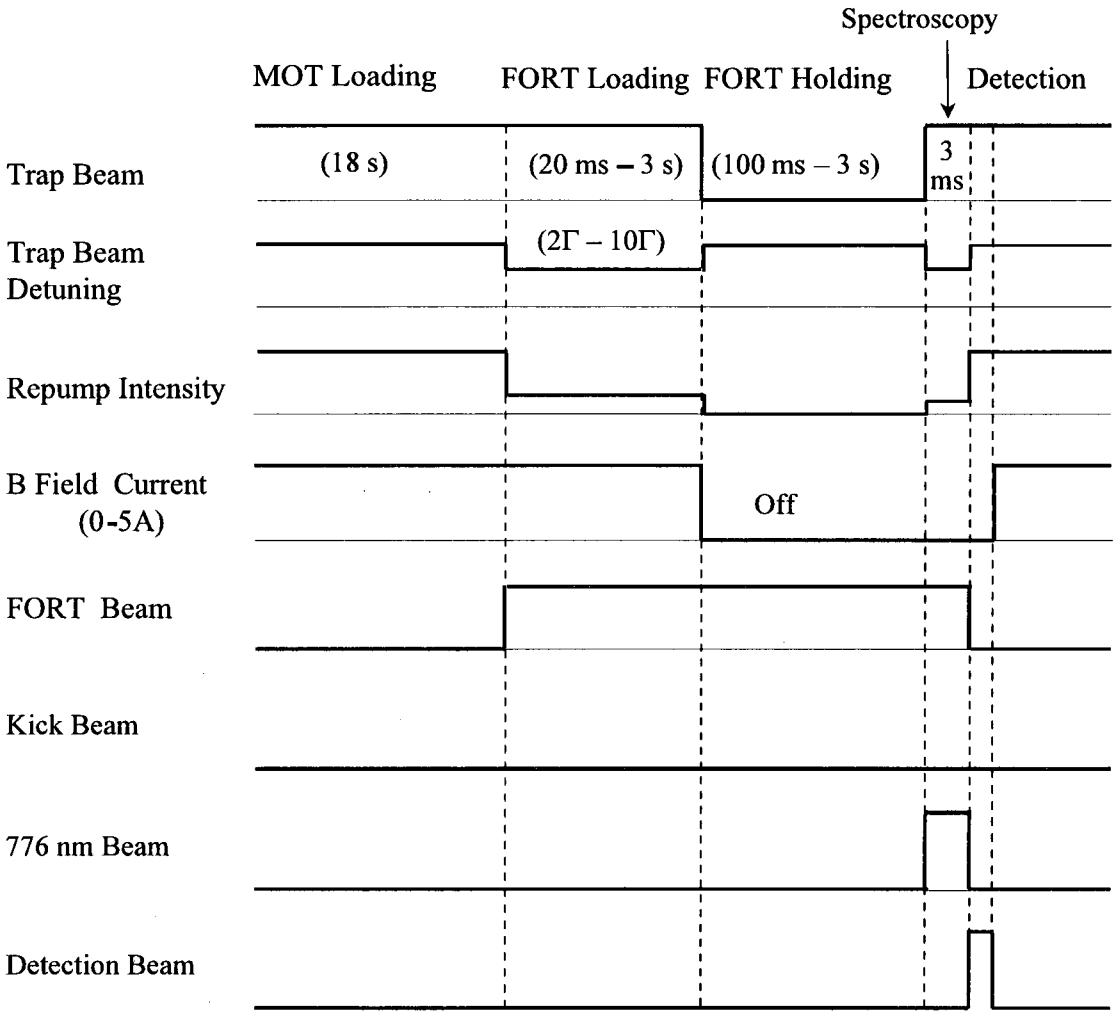

FIG. 56: Kick experiment timing sequence for the different parameters controlled by the DAQ system.

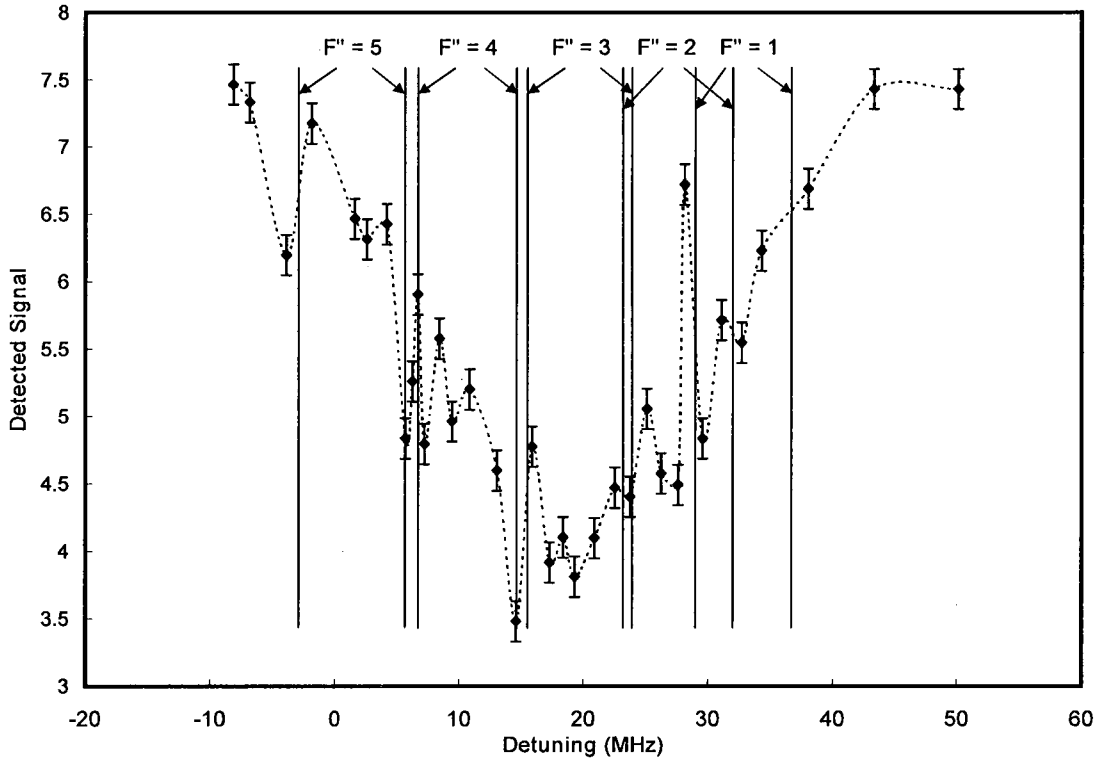

FIG. 57: Detected signal of the ^{85}Rb FORT for -0.5Γ pump laser detuning, 5 Watts FORT laser power, 3 ms probe time, 1 μW probe beam power and 1 mm probe beam diameter.

Watts. The zero frequency in Fig. 57 represents the $5P_{3/2}(F' = 4) \rightarrow 5D_{5/2}(F'' = 5)$ resonance accounting for the shift of the $5P_{3/2}$ state, which is about 7.5 MHz. The vertical lines indicate the expected locations of the Autler-Townes splittings of the $5P_{3/2}(F' = 4) \rightarrow 5D_{5/2}(F'')$ resonances. The splittings were calculated using the average value of Rabi frequency obtained from the MOT spectra. The data represent a global average of three scans taken on different days and seem to show evidence that we have in fact observed the Autler-Townes splitting in the FORT.

Due to the small separations between the hyperfine levels of the $5D_{5/2}$ state (in the order of few MHz), it was hard to resolve the spectra. We also performed the experiment on ^{87}Rb for different pump laser detuning. The observed spectra are shown in Fig. 58 for 5 Watts of Nd:YAG laser power, 3 ms probe time, 200 nW of probe beam power and 1 mm probe beam diameter. The zero frequency represents the shifted $5P_{3/2}(F' = 3) \rightarrow 5D_{5/2}(F'' = 4)$ resonance in the FORT. Fig. 59 shows the scan taken for pump detuning of -3.5Γ, the vertical lines indicate the calculated splitting locations of the $5P_{3/2}(F' = 3) \rightarrow 5D_{5/2}(F'' = 2, 3, 4)$ resonances.

IV.3 INHOMOGENEOUS BROADENING EXPERIMENT

The AC Stark shift of the $5S_{1/2}$ state and that of the $5P_{3/2}$ state in an optical dipole trap created with the Nd:YAG laser are opposite to each other, which results in a shift and inhomogeneous broadening in the $5S_{1/2} \rightarrow 5P_{3/2}$ transition. By the use of the multilevel structure of the atom, one can add another laser with specific power and detuning that has the same spatial intensity profile as the Nd:YAG laser to couple the $5P_{3/2}$ state with a higher excited state. This can result in the same shift for both $5S_{1/2}$ and $5P_{3/2}$ states, which can eliminate or decrease the shift and the broadening of the transition between them.

The 776 nm diode laser described in the previous chapter was used as the second laser to couple the $5P_{3/2}$ state with the $5D_{5/2}$ in ^{85}Rb. Its frequency was set at 270 MHz below the $5P_{3/2} \rightarrow 5D_{5/2}$ resonance frequency. The beam at the FORT was focused to a calculated waist of 16 μm which is the same as that of the Nd:YAG size to ensure that the atoms will experience the same shift spatial profile from the two lasers. The total shift of the $|5S_{1/2}, F, m_F\rangle$ state and that of the $|5P_{3/2}, F, m_F\rangle$ state are then given by:

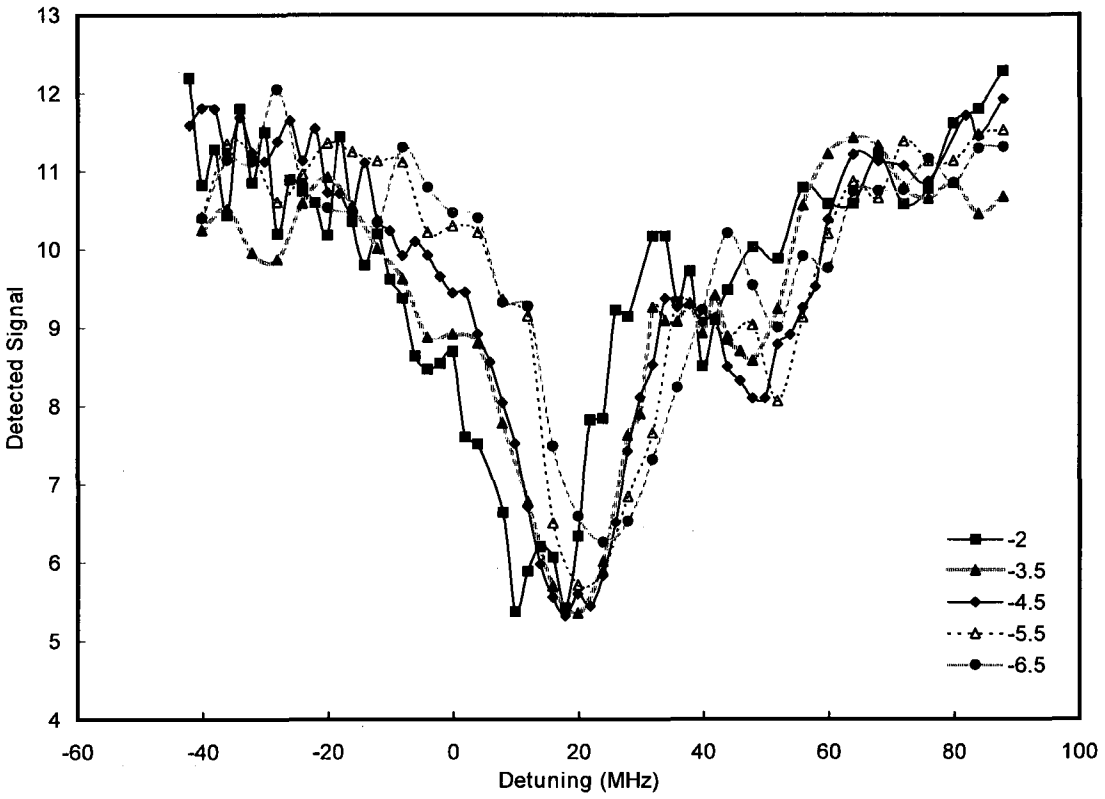

FIG. 58: Detected signal of ^{87}Rb FORT for different pump laser detuning, 5 Watts FORT laser power, 3 ms probe time, 200 nW probe beam power and 1 mm probe beam diameter.

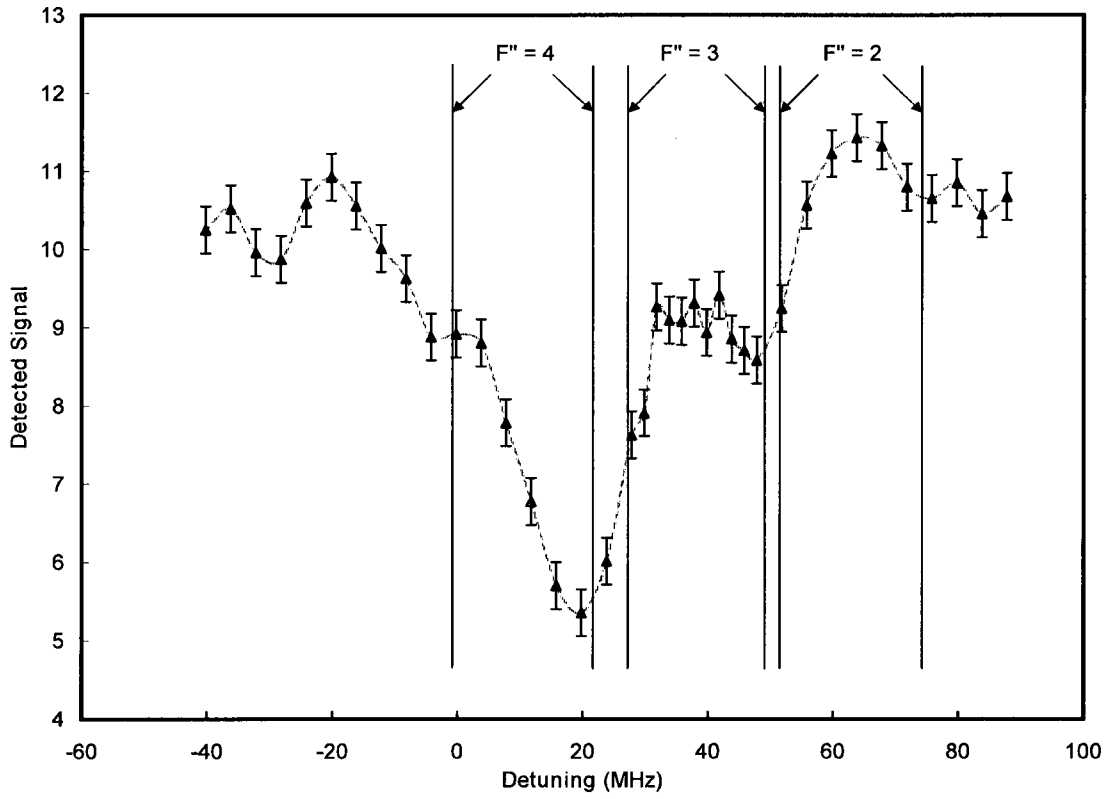

FIG. 59: Detected signal of the ^{87}Rb FORT for -3.5 Γ pump laser detuning, 5 Watts FORT laser power, 3 ms probe time, 200 nW probe beam power and 1 mm probe beam diameter.

$$U_{0(total)}\left(5S_{1/2},\, F,\, m_F\right) = -\alpha_S(1064\,nm)\left|\mathcal{E}_{0(YAG)}\right|^2 - \alpha_S(776\,nm)\left|\mathcal{E}_{0(diode)}\right|^2, \quad (94)$$

$$\begin{aligned} U_{0(Total)}\left(5P_{3/2},\, F,\, m_F\right) = & -\alpha_P(1064\,nm)\left|\mathcal{E}_{0(YAG)}\right|^2 \\ & -\gamma_P(1064\,nm)\frac{3m_F^2 - F(F+1)}{F(2F-1)}\left|\mathcal{E}_{0(YAG)}\right|^2 \\ & -\alpha_P(776\,nm)\left|\mathcal{E}_{0(diode)}\right|^2 \\ & -\gamma_P(776\,nm)\frac{3m_F^2 - F(F+1)}{F(2F-1)}\left|\mathcal{E}_{0(diode)}\right|^2. \end{aligned} \quad (95)$$

The scalar and tensor polarizabilities are given in Eq. (82) and Eq. (83), respectively. The values of the matrix element were evaluated in [77], using these two equations, the scalar and tensor polarizabilities can be calculated as a function of the applied field wavelength. In calculating α_S we considered the coupling of the $5S_{1/2}$ state with $5P_{1/2}$, $5P_{3/2}$, $6P_{1/2}$, $6P_{3/2}$, $7P_{1/2}$, and $7P_{3/2}$ states. For α_P and γ_P, the coupling of the $5P_{3/2}$ state with $5S_{1/2}$, $4D_{3/2}$, $4D_{5/2}$, $5D_{3/2}$, $5D_{5/2}$, and $6S_{1/2}$ states was considered. The values of the reduced matrix elements are given in Table 2.

Fig. 60 shows α_S, α_P, and γ_P as a function of the frequency detuning of the applied laser field from the $5S_{1/2} \rightarrow 5P_{3/2}$ transition frequency. The vertical lines on the higher frequency side are from the divergences at the $5P_{3/2} \rightarrow 5D_J$ resonances.

Fig. 61 shows the total AC Stark shift for the $5S_{1/2}$ and $5P_{3/2}$ states experienced by the atoms in the presence of the Nd:YAG and the 776 nm lasers as a function of the 776 nm laser beam power. The two levels have the same AC Stark shift at about 700 μW of 776 nm laser beam power. In Fig. 62, we show the energy shift for the $5S_{1/2}$ and $5P_{3/2}$ states as a function of laser detuning for fixed power of 700 μW.

Preliminary data were taken for a linearly polarized cw FORT for different 776 nm laser beam powers. The timing sequence used is shown in Fig. 63. For 6 ms before the FORT holding stage ends, we turn on the 776 nm laser with the Nd:YAG laser. 3 ms before the FORT holding stage ends, we also have the kick beam on with the 776 nm laser. Then we detect the number of atoms remaining in the FORT by measuring the fluorescence of the scattered photons using the PMT. By determining the number of atoms kicked out of the trap when the kick beam frequency is scanned, we can determine the spectra of the confined atoms. The kick laser frequency was

TABLE 2: Absolute values of electric-dipole matrix elements used in the calculation of the polarizabilities for ^{85}Rb in atomic units. Taken from Ref. [77].

Transition $(v - w)$	$\lvert\langle v \lVert D \rVert w\rangle\rvert$
$5P_{1/2} - 5S_{1/2}$	4.220
$5P_{3/2} - 5S_{1/2}$	5.956
$6P_{1/2} - 5S_{1/2}$	0.333
$6P_{3/2} - 5S_{1/2}$	0.541
$7P_{1/2} - 5S_{1/2}$	0.115
$7P_{3/2} - 5S_{1/2}$	0.202
$5P_{3/2} - 4D_{3/2}$	3.540
$5P_{3/2} - 4D_{5/2}$	10.634
$5P_{3/2} - 5D_{3/2}$	0.787
$5P_{3/2} - 5D_{5/2}$	2.334
$5P_{3/2} - 6S_{1/2}$	6.013

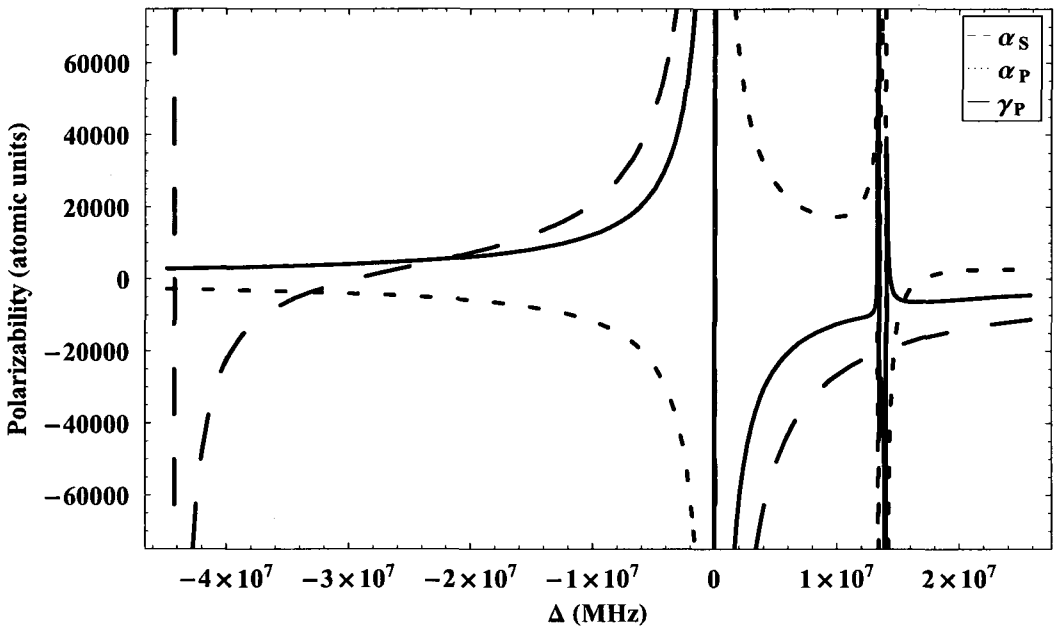

FIG. 60: Calculated polarizabilities of the $5S_{1/2}$ and $5P_{3/2}$ states of ^{85}Rb in atomic units as a function of the detuning from the $5S_{1/2} \rightarrow 5P_{3/2}$ transition frequency.

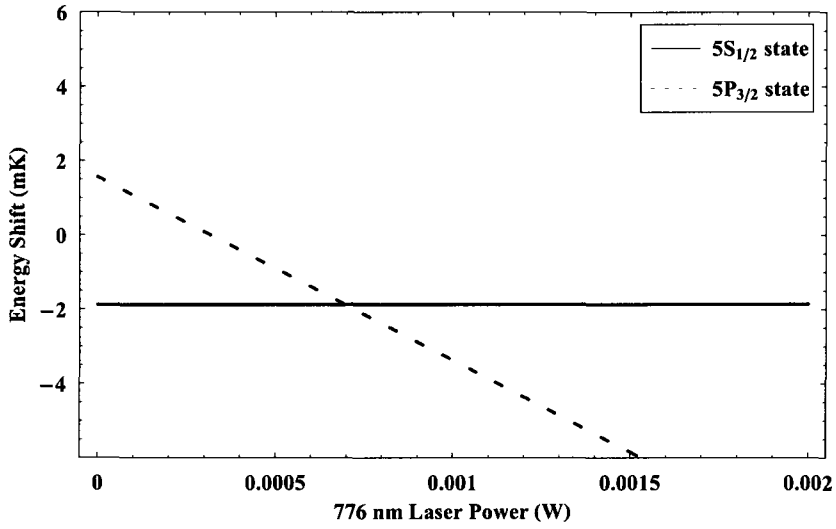

FIG. 61: Calculated AC Stark shift for the $5S_{1/2}$ and $5P_{3/2}$ states of ^{85}Rb as a function of the 776 nm laser power for 5 Watts Nd:YAG laser power, 16 μm beam waist, and 270 MHz 776 nm laser detuning.

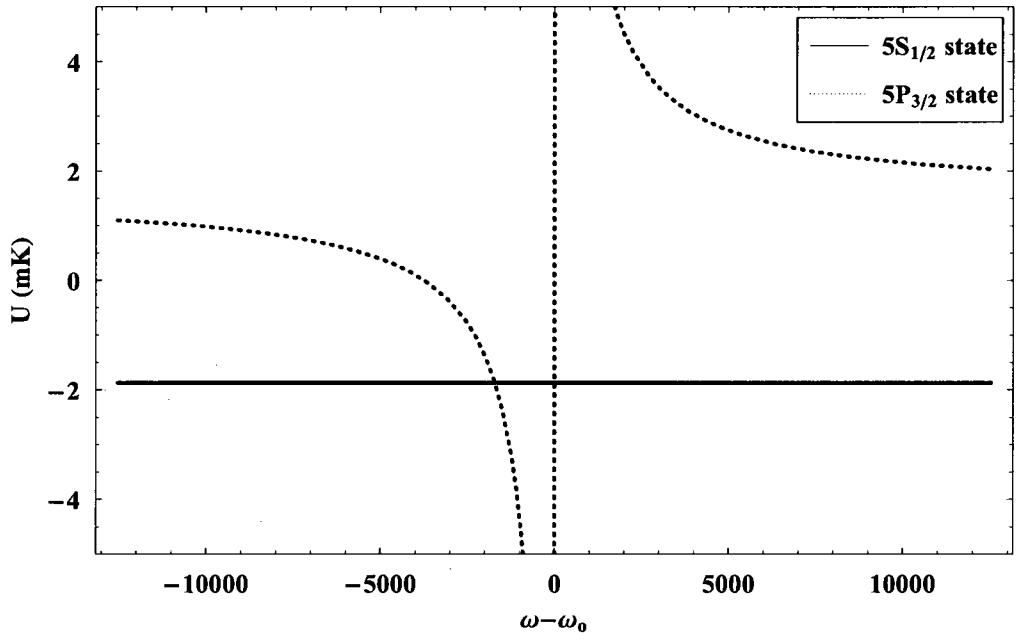

FIG. 62: Calculated AC Stark shift for the $5S_{1/2}$ and $5P_{3/2}$ states of ^{85}Rb as a function of the 776 nm laser detuning from the $5P_{3/2} \rightarrow 5D_{5/2}$ transition frequency for 5 Watts Nd:YAG laser power, 16 μm beam waist, and 776 nm laser power of 700 μW. $\omega - \omega_o = 2\pi\Delta$, where Δ is in units of MHz.

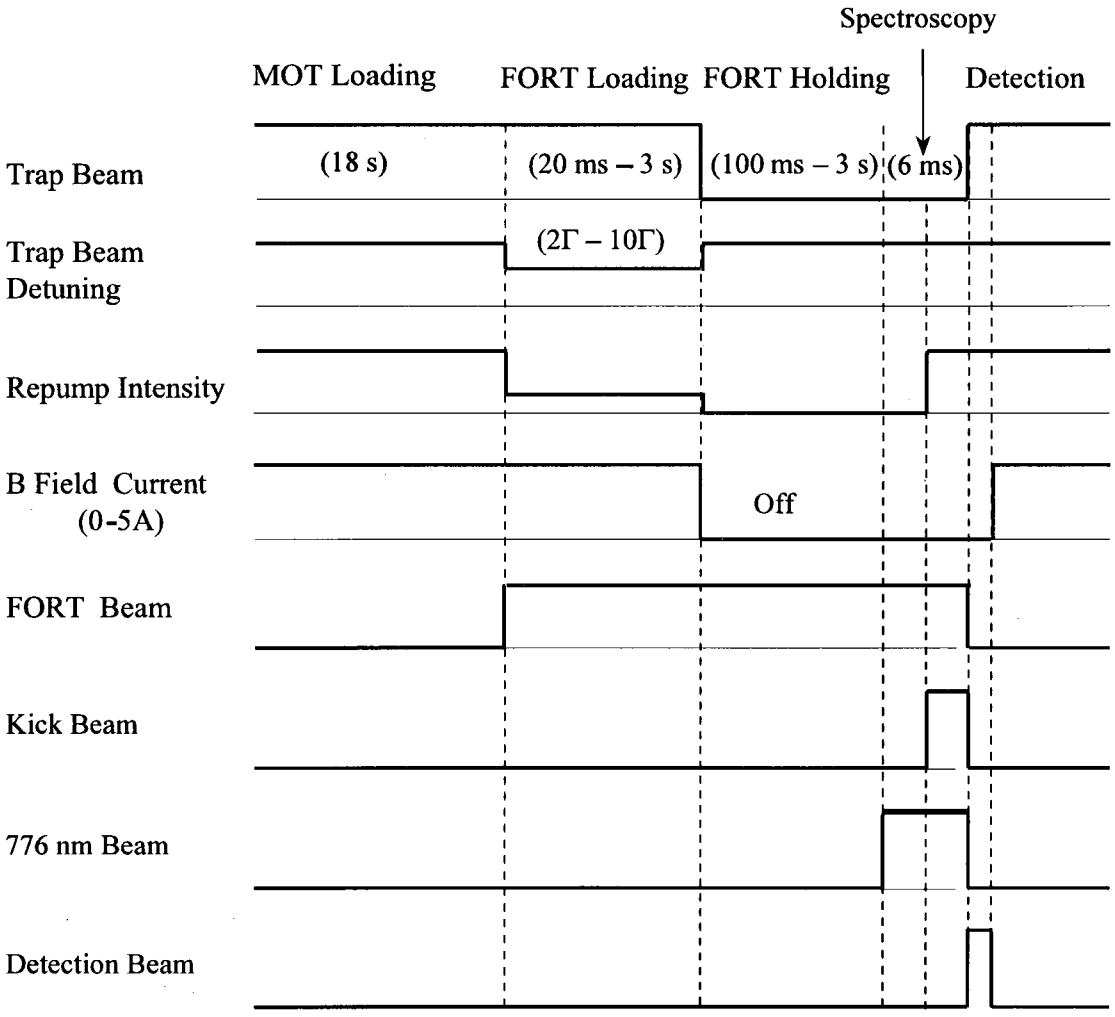

FIG. 63: Inhomogeneous broadening experiment timing sequence for the different parameters controlled by the DAQ system.

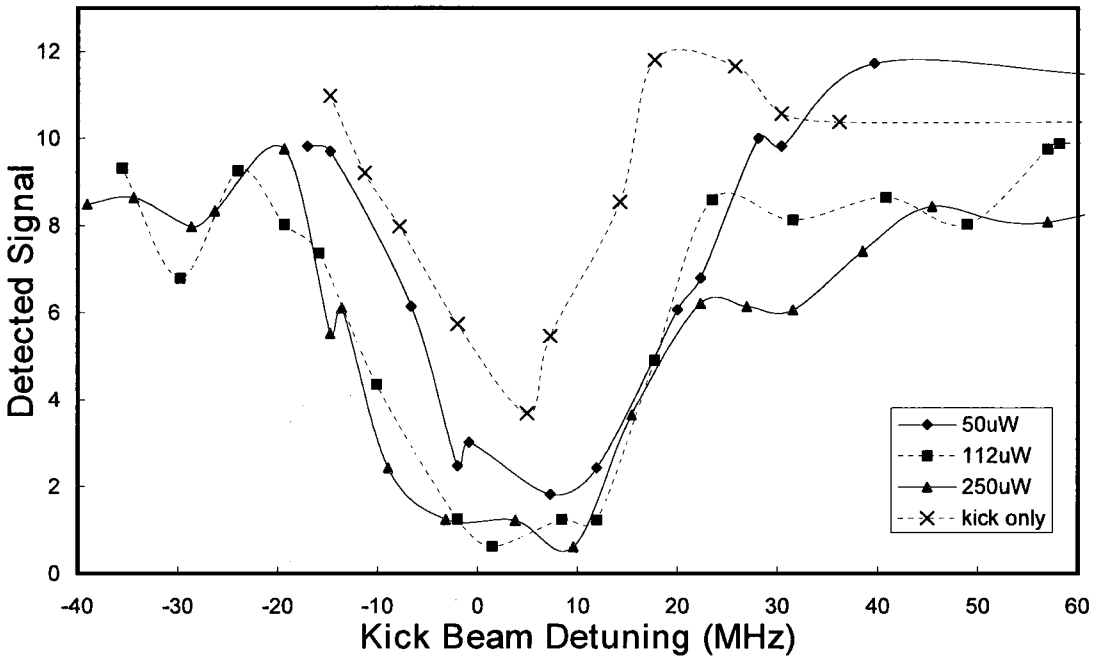

FIG. 64: Detected signal of the linearly polarized cw FORT as a function of the kick beam detuning for different values of the 776 nm laser power for 5 Watts FORT laser power, 10 μW kick beam power, and 1 mm kick beam radius.

scanned over the $F = 3$ to $F' = 4$ transition. Clearly, application of the laser had an effect, but we did not observe a reduction in the linewidth at this time. Based on our detailed calculations, we are confident the spectroscopic linewidth can be reduced, but better characterization of the experimental parameters and further effort will be required to demonstrate the reduction of inhomogeneous broadening in the FORT.

CHAPTER V

CONCLUSION AND OUTLOOK

Optical dipole force traps have been and continue to be used widely in atomic physics experiments. All atoms and molecules are polarizable to some degree, so a dipole force trap can find application if the laser power is sufficient and the wavelength appropriate. Free electron lasers like the one at Thomas Jefferson National Laboratory may find increasing use for creating deep traps for atoms and molecules. The dynamics of cold atom transfer from a magneto-optical trap to an optical dipole force trap, however, is a complicated process. Furthermore, both calculations and experiments have shown that the response of atoms in a pulsed trap (as one would have from a free electron laser) is not always the same as that found in continuous-wave traps.

In this dissertation, we have shown that laser spectroscopy of atoms confined in a trap can be used as a probe to characterize the conditions in the trap and to better understand the response of atoms confined in a trap and hence help elucidate trap dynamics. In one experiment, we used a laser scanning over the upper hyperfine level of the $5S_{1/2}$ ground state to the hyperfine manifold of the $5P_{3/2}$ state in order to investigate the response of Rb atoms confined in a dipole force trap. In a second experiment, we applied laser light at fixed (but adjustable) detuning on the $5S_{1/2} \rightarrow 5P_{3/2}$ transition while we scanned a second laser over the $5P_{3/2} \rightarrow 5D_{5/2}$ transition in both a MOT and a dipole force trap in order to observe the Autler-Townes splitting, which can be used to characterize conditions as seen by atoms in the trap. Finally, we presented calculations showing that it should be possible to greatly reduce the inhomogeneous broadening of the transition spectrum, which results from differing ground and excited state polarizabilities by application of a laser to couple the $5P_{3/2}$ state to the $5D_{5/2}$ state.

Future work in this direction will include: 1) experimental realization of the reduction of inhomogeneous broadening through application of an additional coupling laser; 2) higher resolution scans of all spectral features presented here to more quantitatively describe the trapped atom response; 3) increased exploration of the spectral features as a function of trap and probe parameters like power and especially polarization; and 4) high resolution spectroscopy to explore the differences and similarities of spectra taken in a cw optical dipole force trap as compared to a pulsed trap.

BIBLIOGRAPHY

[1] Ultracold Atom News, Research Groups, retrieved on July 17, 2010 from `http://ucan.physics.utoronto.ca/Groups`

[2] Ultracold Atoms and Quantum Gasses, Research groups working with atom traps, retrieved on July 17, 2010 from `http://www.uibk.ac.at/exphys/ultracold/atomtraps.html`

[3] The Official U.S. Time, retrieved on July 17, 2010 from `http://www.time.gov`

[4] G. A. Askar'yan, Sov. Phys. JETP **15**, 1088 (1962).

[5] V. S. Letokhov, JETP Lett. **7**, 272 (1968).

[6] A. Ashkin, Phys. Rev. Lett. **24**, 156 (1970).

[7] A. Ashkin, Phys. Rev. Lett. **40**, 729 (1978).

[8] T. W. Hänsch and A. L. Schawlow, Opt. Comm. **13**, 68 (1975).

[9] D. J. Wineland and H. Dehmelt, Bul. Am. Phys. Soc. **20**, 637 (1975).

[10] J. E. Bjorkholm, R. R. Freeman, A. Ashkin, and D. B. Pearson, Phys. Rev. Lett. **41**, 1361 (1978).

[11] W. Neuhauser, M. Hohenstatt, P. Toschek, and H. Dehmelt, Phys. Rev. Lett. **41**, 233 (1978).

[12] D. J. Wineland, R. E. Drullinger, and F. L. Walls, Phys. Rev. Lett. **40**, 1639 (1978).

[13] W. D. Phillips and H. Metcalf, Phys. Rev. Lett. **48**, 596 (1982).

[14] S. Chu, L. Hollberg, J. Bjorkholm, A. Cable, and Ashkin, Phys. Rev. Lett. **55**, 48 (1985).

[15] E. L. Raab, M. Prentiss, A. Cable, S. Chu, and D. E. Pritchard, Phys. Rev. Lett. **59**, 2631 (1987).

[16] H. R. Thorsheim, J. Weiner and P. S. Julienne, Phys. Rev. Lett. **58**, 2420 (1987).

[17] P. D. Lett *et al.*, Phys. Rev. Lett. **61**, 169 (1988).

[18] J. Dalibard and C. Cohen-Tannoudji, J. Opt. Soc. Am. B **6**, 2023 (1989).

[19] P. J. Ungar, D. S. Weiss, E. Riis, and Steven Chu, J. Opt. Soc. Am. B **6**, 2058 (1989).

[20] H. G. Dehmelt Phys. Scr. **1991**, 47 (1991).

[21] W. Paul, Rev. Mod. Phys. **62**, 531 (1990).

[22] P. D. Lett, K. Helmerson, W. D. Phillips, L. P. Ratliff, S. L. Rolston, and M. E. Wagshul, Phys. Rev. Lett. **71**, 2200 (1993).

[23] J. D. Miller, R. A. Cline, and D. J. Heinzen, Phys. Rev. Lett. **71**, 2204 (1993).

[24] N. Davidson, H.-J. Lee, M. Kasevich, and S. Chu, Phys. Rev. Lett. **72**, 3158 (1994).

[25] J. Lawall *et al.*, Phys. Rev. Lett. **73**, 1915 (1994).

[26] K. B. Davis *et al.*, Phys. Rev. Lett. **74**, 5202 (1995).

[27] M. H. Anderson, J. R. Ensher, M. R. Mattews, C. E. Wieman, and E. A. Cornell, Science **269**, 198 (1995).

[28] S. Chu, Rev. Mod. Phys. **70**, 685 (1998).

[29] C. N. Cohen-Tannoudji, Rev. Mod. Phys. **70**, 707 (1998).

[30] W. D. Phillips, Rev. Mod. Phys. **70**, 721 (1998).

[31] I. Bloch, T. W. Hänsch, and T. Esslinger, Phys. Rev. Lett. **82**, 3008 (1999).

[32] E. A. Cornell and C. E. Wieman, Rev. Mod. Phys. **74**, 875 (2002).

[33] W. Ketterle, Rev. Mod. Phys. **74**, 1131 (2002).

[34] S. Jochim *et al.*, Science **302**, 2101 (2003).

[35] M. Greiner, C. A. Regal and D. S. Jin, Nature **426**, 537 (2003).

[36] J. L. Hall, Rev. Mod. Phys. **78**, 1279 (2006).

[37] T. W. Hänsch, Rev. Mod. Phys. **78**, 1297 (2006).

[38] K. L. Corwin, Ph. D. Thesis, University of Colorado, Boulder, Colorado, 1999.

[39] S. J. M. Kuppens, K. L. Corwin, K. W. Miller, T. E. Chupp, and C. E. Wieman, Phys. Rev. A **62**, 013406 (2000).

[40] Minarni Minarni, Ph. D. Thesis, Old Dominion University, Virginia, 2006.

[41] M. Shiddiq, E. M. Ahmed, M. D. Havey, C. I. Sukenik, Phys. Rev. A **77**, 045401 (2008).

[42] H. J. Metcalf and P. van der Straten, *Laser Cooling and Trapping. Graduate Texts in Contemporary Physics* (Springer, New York, 1999).

[43] S. R. Granade, M. E. Gehm, K. M. O'Hara, and J. E. Thomas, Phys. Rev. Lett. **88**, 120405 (2002).

[44] D. G. Fried *et al.*, Phys. Rev. Lett **81**, 3811 (1998).

[45] G. Kirchhoff and R. Bunsen, Ann. Phys. Chem. **189** (7), 337 (1861).

[46] D. A. Steck, Rubidium 85 D Line Data, Version 2.1.2, retrieved on June 26, 2010 from `http://steck.us/alkalidata/rubidium85numbers.pdf`

[47] D. A. Steck, Rubidium 87 D Line Data, Version 2.1.2, retrieved on June 26, 2010 from `http://steck.us/alkalidata/rubidium87numbers.pdf`

[48] C. Savage, Aust. J. Phys. **49**, 745 (1996).

[49] D. Budker, D. F. Kimball and D. P. DeMille, *Atomic Physics, An exploration through problems and solutions* (Oxford University Press, New York, 2004).

[50] M. Schulz, Ph. D. Dissertation, Innsbruck University, Innsbruck, 2002.

[51] J. Dalibard and C. Cohen-Tannoudji, J. Opt. Soc. Am. B **2**, 1707 (1985).

[52] R. Grimm, M. Weidemüller and Y. B. Ovchinnikov, Adv. At. Mol. Opt. Phys. **42**, 95 (2000).

[53] C. Wieman, G. Flowers, and S. Gilbert, Am. J. Phys. **63**, 317 (1995).

[54] K. B. MacAdam, A. Steinbach, and C. Wieman, Am. J. Phys. **60**, 1098 (1995).

[55] C. Cohen-Tannoudji, J. Dupont-Roc, and G. Grynberg, *Atom-photon interactions: Basic processes and applications* (John Wiley & Sons, New York, 1992).

[56] A. E. Siegman, *Lasers* (University Science Books, Mill Valley, California, 1986).

[57] C. J. Foot, *Atomic Physics*, in Oxford Master Series in Atomic, Optical and Laser Physics (Oxford University Press, New York, 2005).

[58] J. D. Miller, R. A. Cline and D. J. Heinzen, Phys. Rev. A **47**, R4567 (1993).

[59] J. Y. Kim, J. S. Lee, J. H. Han and D. Cho, J. Korean Phys. Soc. **42**, 483 (2003).

[60] D. Cho, J. Korean Phys. Soc. **30**, 373 (1997).

[61] J. M. Choi and D. Cho, J. Phys.: Conf. Ser. **80**, 012037 (2007).

[62] A. Khadjavi, A. Lurio, and W. Happer, Phys. Rev. **167**, 128 (1968).

[63] S. H. Autler and C. H. Townes , Phys. Rev. **100**, 703 (1955).

[64] R. M. Whitley and C. R. Stroud, Jr., Phys. Rev. A **14**, 1498 (1976).

[65] C. Cohen-Tannoudji and S. Reynaud, J. Phys. B: At. Mol. Phys. **10**, 345 (1977).

[66] A. G. Sinclair, B. D. McDonald, E. Riis and G. Duxbury, Opt. Comm. **106**, 207 (1994).

[67] E. A. Donley, T. P. Heavner, F. Levi, M. O. Tataw, and S. R. Jefferts, Rev. Sci. Instrum. **76**, 063112 (2005).

[68] Spectra-Physics, CW Nd:YAG Laser System, Model 3800, *Instruction Manual* (February 1988).

[69] C. J. Hawthorn, K. P. Weber, and R. E. Scholten, Rev. Sci. Instrum. **72**, 12 (2001).

[70] T. T. Grove, V. Sanchez-Villicana, B. C. Duncan, S. Maleki, and P. L. Gould, Phys. Scr. **52**, 271 (1995).

[71] B. C. Duncan, V. Sanchez-Villicana, and P. L. Gould, Phys. Rev. A **63**, 043411 (2001).

[72] Y. Millerioux *et al.*, Opt. Comm. **108**, 91(1994).

[73] J. E. Bjorkholm and P. F. Liao, Phys. Rev. Lett. **33**, 128 (1974).

[74] J. E. Bjorkholm and P. F. Liao, Phys. Rev. A **14**, 751 (1976).

[75] O. S. Heavens, J. Opt. Soc. Am. **51**, 1058 (1961).

[76] S. B. Bayram, M. Havey, M. Rosu, A. Sieradzan, A. Derevianko, and W. R. Johnson, Phys. Rev. A **61**, 050502(R) (2000).

[77] M. S. Safronova, Carl J. Williams, and Charles W. Clark, Phys. Rev. A **69**, 022509 (2004).

VITA

Eman Mohammed Ahmed
Department of Physics
Old Dominion University
Norfolk, VA 23529

Alias: Eman Ahmed

EDUCATION:

Ph. D. in Physics, Old Dominion University, Norfolk, VA, August 2010
M. Sc. in Physics, Old Dominion University, Norfolk, VA, December 2005.
B. Sc. in Physics, Cairo University, Egypt, June 2000.

PROFESSIONAL EXPERIENCE:

Research Assistant, Spring 2005–present, Department of Physics, Old Dominion University, Norfolk, VA.
Teaching Assistant, Fall 2004, Department of Physics, Old Dominion University, Norfolk, VA.

PUBLICATIONS:

· "Investigation of loading of pulsed and continuous-wave optical dipole force traps," M. Shiddiq, E. M. Ahmed, M. D. Havey, C. I. Sukenik, Phys. Rev. A 77, 045401 (2008).
· "Trap Loss in a Dual Species Rb-Ar* Magneto-optical Trap," H. C. Busch, M. K. Shaffer, E. M. Ahmed, and C. I. Sukenik, Phys. Rev. A. 73, 023406 (2006).

Typeset using LaTeX.